

ISSN 1881-7815 Online ISSN 1881-7823

BST

BioScience Trends

Volume 8, Number 5
October, 2014



www.biosciencetrends.com

BioScience Trends is one of a series of peer-reviewed journals of the International Research and Cooperation Association for Bio & Socio-Sciences Advancement (IRCA-BSSA) Group and is published bimonthly by the International Advancement Center for Medicine & Health Research Co., Ltd. (IACMHR Co., Ltd.) and supported by the IRCA-BSSA and Shandong University China-Japan Cooperation Center for Drug Discovery & Screening (SDU-DDSC).

BioScience Trends devotes to publishing the latest and most exciting advances in scientific research. Articles cover fields of life science such as biochemistry, molecular biology, clinical research, public health, medical care system, and social science in order to encourage cooperation and exchange among scientists and clinical researchers.

BioScience Trends publishes Original Articles, Brief Reports, Reviews, Policy Forum articles, Case Reports, News, and Letters on all aspects of the field of life science. All contributions should seek to promote international collaboration.

Editorial Board

Editor-in-Chief:

Masatoshi MAKUCHI
Japanese Red Cross Medical Center, Tokyo, Japan

Misao MATSUSHITA

Tokai University, Hiratsuka, Japan

Takashi SEKINE

The University of Tokyo, Tokyo, Japan

Yasuhiko SUGAWARA

The University of Tokyo, Tokyo, Japan

</div

BioScience Trends

Editorial and Head Office

Pearl City Koishikawa 603, 2-4-5 Kasuga, Bunkyo-ku,
Tokyo 112-0003, Japan

Tel: +81-3-5840-8764, Fax: +81-3-5840-8765
E-mail: office@biosciencetrends.com
URL: www.biosciencetrends.com

Editorial Board Members

Girdhar G. AGARWAL (Lucknow, India)	Takahiro HIGASHI (Tokyo, Japan)	Mark MEUTH (Sheffield, UK)	Koji TANAKA (Tsu, Japan)	
Hirotugu AIGA (Geneva, Switzerland)	De-Xing HOU (Kagoshima, Japan)	Satoko NAGATA (Tokyo, Japan)	John TERMINI (Duarte, CA, USA)	
Hidechika AKASHI (Tokyo, Japan)	Sheng-Tao HOU (Ottawa, Canada)	Miho OBA (Odawara, Japan)	Usa C. THISYAKORN (Bangkok, Thailand)	
Moazzam ALI (Geneva, Switzerland)	Yong HUANG (Ji'ning, China)	Xianjun QU (Ji'nan, China)	Toshifumi TSUKAHARA (Nomi, Japan)	
Ping AO (Shanghai, China)	Hirofumi INAGAKI (Tokyo, Japan)	John J. ROSSI (Duarte, CA, USA)	Kohjiro UEKI (Tokyo, Japan)	
Hisao ASAMURA (Tokyo, Japan)	Masamine JIMBA (Tokyo, Japan)	Carlos SAINZ-FERNANDEZ (Santander, Spain)	Masahiro UMEZAKI (Tokyo, Japan)	
Michael E. BARISH (Duarte, CA, USA)	Kimitaka KAGA (Tokyo, Japan)	Yoshihiro SAKAMOTO (Tokyo, Japan)	Junming WANG (Jackson, MS, USA)	
Boon-Huat BAY (Singapore, Singapore)	Ichiro KAI (Tokyo, Japan)	Erin SATO (Shizuoka, Japan)	Ling WANG (Shanghai, China)	
Yasumasa BESSHIO (Nara, Japan)	Kazuhiro KAKIMOTO (Osaka, Japan)	Takehito SATO (Isehara, Japan)	Xiang-Dong Wang (Boston, MA, USA)	
Generoso BEVILACQUA (Pisa, Italy)	Kiyoko KAMIBEPPU (Tokyo, Japan)	Akihito SHIMAZU (Tokyo, Japan)	Hisashi WATANABE (Tokyo, Japan)	
Shiuan CHEN (Duarte, CA, USA)	Haidong KAN (Shanghai, China)	Zhifeng SHAO (Shanghai, China)	Lingzhong XU (Ji'nan, China)	
Yuan CHEN (Duarte, CA, USA)	Bok-Luel LEE (Busan, Korea)	Ri SHO (Yamagata, Japan)	Masatake YAMAUCHI (Chiba, Japan)	
Naoshi DOHMAE (Wako, Japan)	Mingjie LI (St. Louis, MO, USA)	Judith SINGER-SAM (Duarte, CA, USA)	Aitian YIN (Ji'nan, China)	
Zhen FAN (Houston, TX, USA)	Shixue LI (Ji'nan, China)	Raj K. SINGH (Dehradun, India)	George W-C. YIP (Singapore, Singapore)	
Ding-Zhi FANG (Chengdu, China)	Ren-Jang LIN (Duarte, CA, USA)	Junko SUGAMA (Kanazawa, Japan)	Xue-Jie YU (Galveston, TX, USA)	
Yoshiharu FUKUDA (Ube, Japan)	Daru LU (Shanghai, China)	Hiroshi TACHIBANA (Isehara, Japan)	Benny C-Y ZEE (Hong Kong, China)	
Rajiv GARG (Lucknow, India)	Hongzhou LU (Shanghai, China)	Tomoko TAKAMURA (Tokyo, Japan)	Yong ZENG (Chengdu, China)	
Ravindra K. GARG (Lucknow, India)	Duan MA (Shanghai, China)	Tadatoshi TAKAYAMA (Tokyo, Japan)	Xiaomei ZHU (Seattle, WA, USA)	
Makoto GOTO (Tokyo, Japan)	Francesco MAROTTA (Milano, Italy)	Shin'ichi TAKEDA (Tokyo, Japan)	(as of August 2014)	
Demin HAN (Beijing, China)	Yutaka MATSUYAMA (Tokyo, Japan)	Sumihito TAMURA (Tokyo, Japan)		
David M. HELFMAN (Daejeon, Korea)	Qingyue MENG (Beijing, China)	Puay Hoon TAN (Singapore, Singapore)		

Brief Report

- 242 - 247** Local immune compartments are related to the severity of dextran sodium sulphate induced colitis.
Luman Wang, Xuechao Jiang, Xiaoming Liu, Tingting Qian, Yiwei Chu

Original Articles

- 248 - 252** Involvement of the central monoaminergic system in the antidepressant-like effect of catalpol in mice.
Junming Wang, Ying Cui, Weisheng Feng, Yueyue Zhang, Guifang Wang, Xingxing Wang, Gai Zhou
- 253 - 259** Protection of *Angelica sinensis* (Oliv) Diels against hepatotoxicity induced by *Dioscorea bulbifera* L. and its mechanism.
Chengwei Niu, Junming Wang, Lili Ji, Zhengtao Wang
- 260 - 265** Fabrication and bioactivity evaluation of porous anodised TiO₂ films *in vitro*.
Fei Teng, Juanjuan Li, Yanyun Wu, Haohua Chen, Qi Zhang, Hu Wang, Guomin Ou
- 266 - 273** Clinical utility of simultaneous measurement of alpha-fetoprotein and des-γ-carboxy prothrombin for diagnosis of patients with hepatocellular carcinoma in China: A multi-center case-controlled study of 1,153 subjects.
Peipei Song, Xiaobin Feng, Yoshinori Inagaki, Tianqiang Song, Keming Zhang, Zhigang Wang, Shuguo Zheng, Kuansheng Ma, Qiang Li, Dalu Kong, Qiang Wu, Ti Zhang, Xin Zhao, Kiyoshi Hasegawa, Yasuhiko Sugawara, Norihiro Kokudo, Wei Tang and Japan-China Joint Team for Medical Research and Cooperation on HCC
- 274 - 279** Relationship between renal apparent diffusion coefficient values and glomerular filtration rate in infants with congenital hydronephrosis.
Feifei Lin, Zhiyong Li, Yungen Gan, Longwei Sun, Di Gang Fang, Kui Xiang, Lei Liu
- 280 - 285** Use of a mini-instrument in endoscopic thyroidectomy via a breast approach to improve cosmetic outcomes.
Wei Zhang, Chenpo Dang, Chengxiang Shan, Sheng Liu, Zhiguo Jiang, Bin Wang, Ming Qiu

Commentary

- 286 - 289** **Revisiting Einstein's brain in Brain Awareness Week.**
Hao Chen, Su Chen, Lidan Zeng, Lin Zhou, Shengtao Hou

Guide for Authors

Copyright

Local immune compartments are related to the severity of dextran sodium sulphate induced colitis

Luman Wang, Xuechao Jiang, Xiaoming Liu, Tingting Qian, Yiwei Chu*

Department of Immunology and Key Laboratory of Medical Molecular Virology of MOE/MOH, School of Basic Medical Sciences, Biotherapy Research Center of Fudan University, Shanghai, China.

Summary

Dextran sodium sulphate (DSS) induced colitis is commonly used to simulate human ulcerative colitis (UC). However, the mucosal immune responses related to the severity of disease have not been comprehensively documented. We used different concentration of DSS, induced various severities of colitis, and simultaneously examined the frequency of immune cells, antibodies and cytokine production. We found that T regulatory cells (Tregs), B cells, and IgA secretion increased on the recovery phase of mild colitis, accompanied by CD11b⁺ cells, interleukin (IL)-6 and tumor necrosis factor (TNF)- α accumulated mildly. While during severe and irreversible colitis, the CD11b⁺ cells, IL-6, and TNF- α infiltrated severely with Tregs, B cells, and IgA increased inconspicuously. These results demonstrate that Tregs, B cells, and IgA may play a significant role in maintaining the homeostasis of gut, by suppressing CD11b⁺ cells and the pro-inflammatory cytokines.

Keywords: DSS induced colitis, Tregs, B cells, IgA, CD11b⁺ cells

1. Introduction

Ulcerative colitis (UC) is an inflammatory bowel disease characterized by intestinal inflammation and mucosal damage (1). A widely used experimental model of colitis involves oral administration of dextran sulphate sodium (DSS) dissolved in drinking water. The exact mechanism through which DSS initiates colitis is unknown. One of the possible mechanisms is that DSS activates gut-associated lymphoid tissues (GALT) immune cells (2).

GALT are important for the maintenance of intestinal homeostasis, which consist of Peyer's patches, intraepithelial lymphocytes (IEL), lamina propria (LP) and mesenteric lymph nodes (MLN). The GALT that contain lymphocytes can be divided into two main immune-function-based compartments, the bacterial and antigen elimination required effector compartment and self-tolerance regulator compartment, which are associated with colitis symptoms (3). Granulocytes and

macrophages produce proinflammatory cytokines such as IL-6, TNF- α and are reported to be directly involved in the pathogenesis of UC (4,5). On the contrary, B cells are mainly located within the Peyer's patches and after cell differentiation, IgA plasmablasts migrate to the lamina propria and secrete IgA into the gut lumen (6-9). In addition, Treg cells also play an essential role in mucosal immune tolerance (10,11). The other essential protective cytokines related to B cells and Tregs are transforming growth factor (TGF)- β and IL-10 (12-16). Although the etiology and pathogenesis of colitis are still unclear, inappropriate activation of the GALT immune system has played an important role in the pathogenesis of mucosal inflammation (3). However, whether the expression of those GALT immune compartments are involved in the degree and the recovery of colitis have not yet been completely identified.

In this study, we used 1% DSS and 3.5% DSS to induce mild and severe colitis respectively. By comparing the immune compartments in the GALT during mild or severe colitis, we demonstrated that regulators such as Tregs, B cells, and IgA increased in the recovery phase of mild colitis. While during severe colitis, the amount of GALT regulators did not change or decreased which resulted in irreversible colitis.

*Address correspondence to:

Dr. Yiwei Chu, Department of Immunology, Shanghai Medical School, 138 YixueYuan Road, Shanghai 200032, China.

E-mail: yiwei_chu@126.com

2. Materials and Methods

2.1. Mice

Wild-type (WT) C57BL/6 mice were obtained from the Chinese Academy of Science (Shanghai, China). All mice used were 8-12 weeks of age and were housed in the animal facility of Fudan University, China. All animals received care in accordance with the Animal Care and Use Committee at Fudan University.

2.2. DSS-induced colitis

Mice were given 1% DSS (molecular weight 36-50 kDa) (MP Biomedicals, Inc., Santa Ana, CA, USA) or 3.5% DSS in their drinking water for 7 days followed by regular drinking water (17). The Disease activity index (DAI) was scored on a grade from 0 to 4 based on daily assessment of body weight, stool consistency, and detection of rectal bleeding, and then averaged for each parameter. Parameters were scored as follows: body weight loss scores (0, none; 1, 1-5%; 2, 6-10%; 3, 11-15%; 4, over 15%), stool scores (0, normal stools; 2, loose stools; 4, diarrhea) and fecal bleeding scores (0, negative hemoccult test; 1, positive hemoccult test; 2, blood visibly present in the stool; 3, blood visibly and blood clotting on the anus; 4, gross bleeding) as previously described (17).

2.3. Histology

At day 7 and day 10 after DSS administration, mice were sacrificed, the colon was removed and the segments were fixed in 10% buffered formalin. After paraffin embedding, five-micrometer thick sections were cut transversely and stained with hematoxylin and eosin (H&E). Assessment of histological colon injury was performed at 200 \times as previously described (18). A histology score was generated on a grade from 0 to 4 as follows: 0, normal tissue; 1, mild inflammation with scattered inflammatory cells; 2, moderate inflammation with multiple foci and/or mild epithelial ulcerations; 3, severe inflammation with massive infiltrating mononuclear cells and/or ulcerations in more than 30% of the tissue; and 4, inflammation with transmural inflammatory cell infiltration and/or more than 75% of the tissue section affected.

2.4. Gut cell isolation

MLN, Peyer's patches, intraepithelial lymphocytes (IEL) and lamina propria lymphocytes (LPL) were isolated by the method of Lefrancois and Lycke (19). Briefly, MLN were isolated and then the whole intestine was flushed with Ca²⁺Mg²⁺-free 100 mM HBSS (CMF) (Sigma-Aldrich, St. Louis, MO, USA). RPMI was injected into the intestine to highlight Peyer's patches, which were

then collected with a fine forceps and scissors. The intestines were opened longitudinally and cut into small sections, shook with CMF solution containing HEPES, NaHCO₃, DTT and EDTA (all from Sigma-Aldrich, St. Louis, MO, USA), and 2% fetal bovine serum (FBS) (Gibco®, Portland, OR, USA) at 37°C. IELs were then purified using discontinuous Percoll gradients (GE Healthcare, Buckinghamshire, UK). For the isolation of LPLs, intestinal pieces were digested with complete RPMI-1640 containing collagenase (Roche Applied Science, Upper Bavaria, Germany), dispase (Sigma-Aldrich, St. Louis, MO, USA) and DNase I (Sigma-Aldrich, St. Louis, MO, USA) at 37°C. LPLs were then purified using Percoll gradients.

2.5. Flow cytometry and antibodies

Single cell suspensions from the MLN, Peyer's patches, epithelium (IEL) and LP were incubated with the 2.4G2 antibody (eBioscience, San Diego, CA, USA) to block FcR II/III receptors before staining with specific Ab. The anti-mouse antibodies B220-PE-Texas Red, CD3-PerCP-Cy7, CD4-APC-Cy7, Foxp3-APC and CD11b-Pacific Blue were purchased from eBioscience (San Diego, CA, USA). Surface and intracellular Foxp3 staining was performed using the manufacturer's recommended protocol. Cells were applied to a CyAn™ ADP Analyzer (Beckman Coulter, Inc., Carlsbad, CA, USA) and data were analyzed using FlowJo software (Tree Star, Ashland, Or, USA).

2.6. ELISA

The intestines were isolated and flushed with 40 ml endotoxin free PBS. Mucus containing fluid was harvested and stored at -80°C until assayed. The concentration of IL-6, IL-10, TNF- α , TGF- β , IgM, and IgA was evaluated using the Mouse Ready-SET-Go! ELISA kits from eBioscience (San Diego, CA, USA) according to the manufacturer's instructions.

2.7. Statistical analysis

Multiple group comparisons were performed using one-way ANOVA, followed by Bonferroni Correction to compare two individual groups. The Spearman correlation was used to evaluate the relationship between immune factors and DAI. Statistical analysis was performed using STATA 8.0 or Prism 5.0. *p* values < 0.05 were considered statistically significant.

3. Results and Discussion

To induce UC assembled colitis, mice were treated with 1% or 3.5% DSS respectively, percentage change in body weight, DAI, colon length and histology of colonic sections of DSS treated and healthy animals

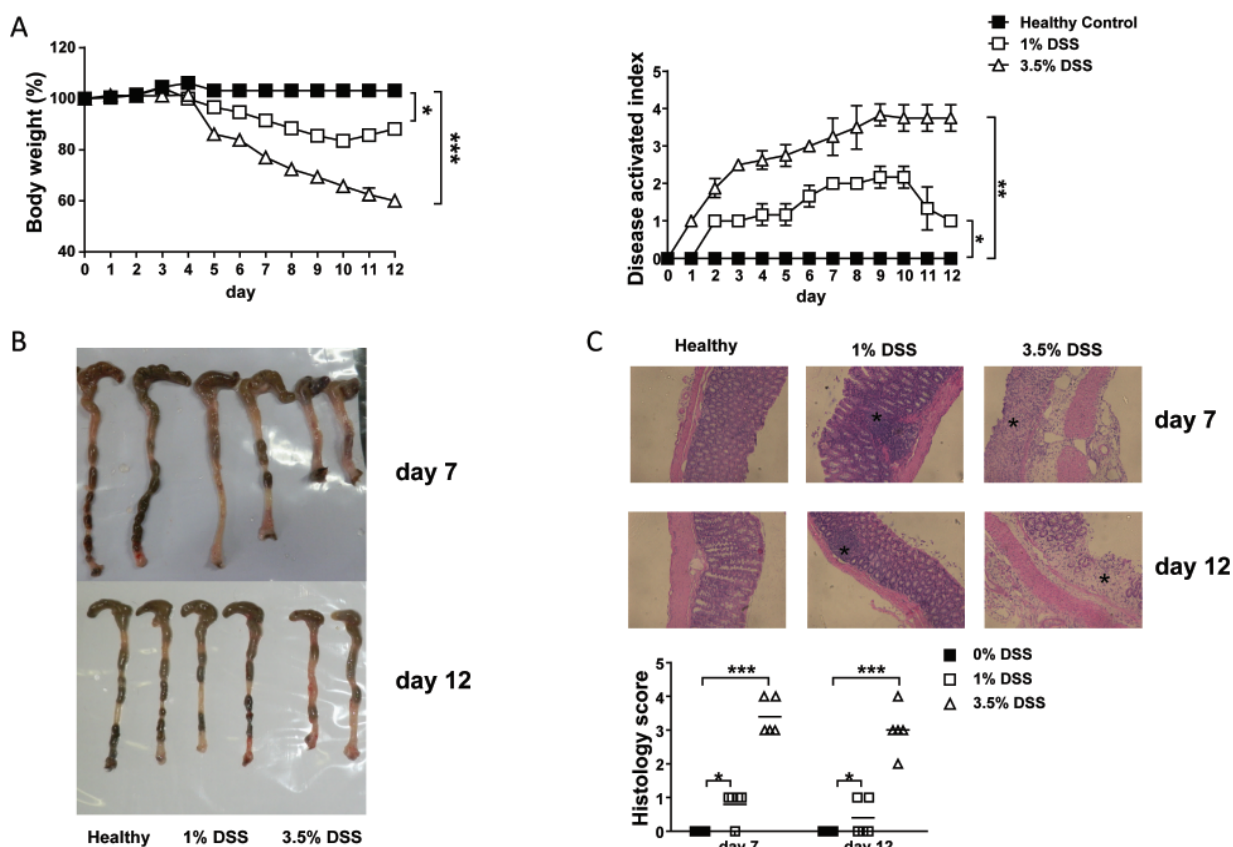


Figure 1. Figure 1. Clinical and macroscopic signs of inflammation. Mice were administered 1% or 3.5% DSS in drinking water for seven days followed by regular drinking water for an additional five days. Controls only received regular drinking water. Mice were evaluated daily for weight loss and DAI scores were calculated (A). Upon sacrifice of the mice, colons were harvested for length determination and gross comparison (B). Representative colon histological sections stained with H&E are shown for the WT and μMT groups (C). Images are shown at 200×. An asterisk indicates the position of the leukocyte infiltration in the histological images. Histological sections were blindly scored on a scale of 0 to 4 to generate a histological score (C). The data shown are the mean ± SEM of one experiment with five mice and was repeated three times with similar results. * $p < 0.05$; ** $p < 0.01$; *** $p < 0.001$.

were observed (Figure 1). Mice showed mild symptoms of colitis at a dose of 1% DSS, but showed significantly more weight loss and more severe disease as measured by the disease activity index of 3.5% DSS. 1% DSS treated mice developed diarrhea and lost more than 10% of their body weight starting on day 8, which was accelerated in 3.5% DSS treated mice to day 5. 1% DSS treated mice began to recover starting on day 10, whereas, 3.5% DSS mice continued to progress with no diminution of disease symptoms or severity (Figure 1A). The macroscopic findings continued to be significantly different within groups, 3.5% DSS treated mice had significantly shorter colons (Figure 1B). Finally, histological examination of the colonic sections from 3.5% DSS-induced colitis mice showed severe inflammatory changes in the colon, such as ulcerations, crypt dilation, goblet cell depletion as well as inflammatory cell infiltration preferentially in the acute (day 8) and recovery phase (day 12), when compared to healthy control animals. These tissue changes were milder in mice treated with 1% DSS (Figure 1C). Thus, we demonstrated that higher concentrations of DSS induced more severe and irreversible intestinal injury, which is consistent with a previous study (20). Thus, we asked whether the severity of disease related to

the mucosal immune responses.

In a previous study, phenotypic changes in immune compartments associated with DSS-induced colitis were determined within splenic cells and MLN. They showed that adaptive immune responses are induced during colitis (21). Thus, we asked whether the local GALT immune cells are recruited and activated during mild (1% DSS treated) or severe colitis (3.5% DSS treated). GALT cells were isolated and analyzed by flow cytometry. On day 12, the recovery phase, there was a significant increase in the percentage of Tregs in the MLN, Peyer's patch, iEL and LPL of 1% DSS treated mice while the frequencies didn't alter in the GALT of 3.5% DSS treated mice. During the 1% DSS treatment, the frequencies of B cells increased in the initial compartment MLN and effected the iEL compartment of GALT while the frequencies decreased in the MLN, Peyer's patch and LPL of 3.5% DSS treated mice (Figure 2). On the other hand, the effector compartment of GALT-CD11b⁺ cells were significantly increased in the MLN, Peyer's patch, and iEL during 3.5% DSS induced colitis while the percentage changed mildly in 1% DSS treated mice. At sites of intestinal inflammation, CD11b⁺ cells such as granulocytes and macrophages produced high levels of

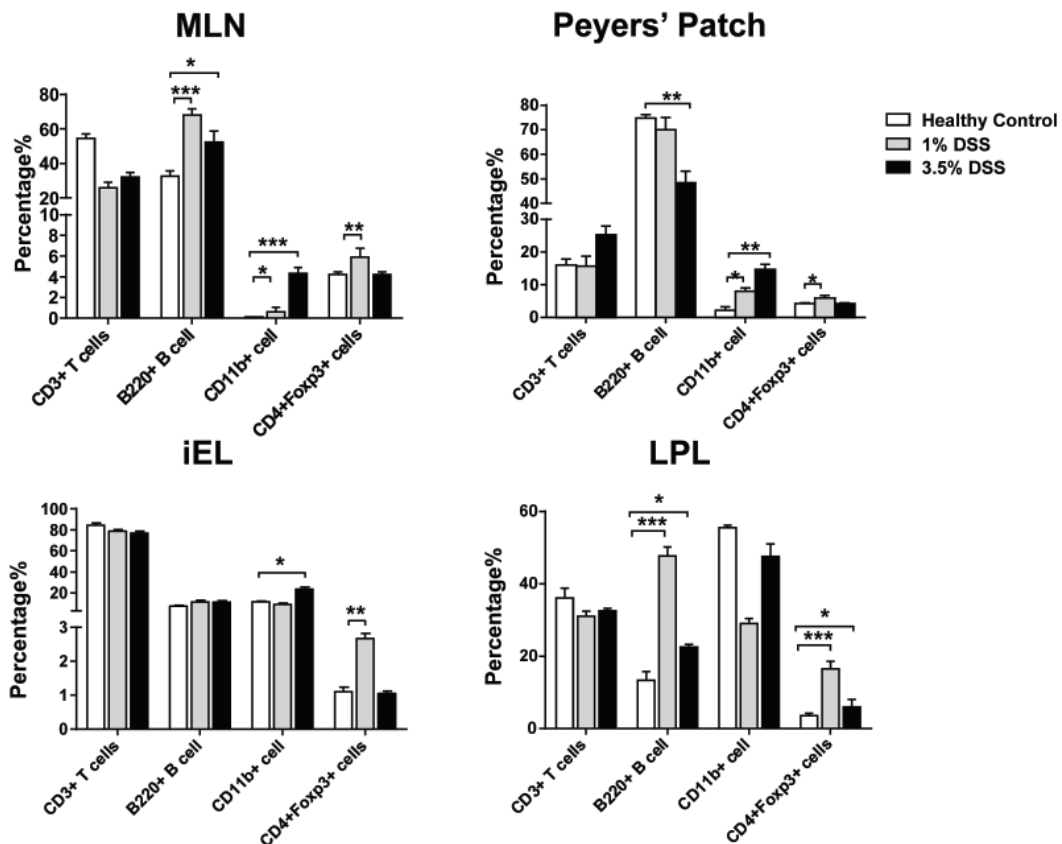


Figure 2. Percentage of immune cell populations in GALT on day 12. Colitis was induced as in Figure 1. Flow cytometry was used to determine the percentage of CD3⁺ T cells, B220⁺ B cells, CD11b⁺ cells and Tregs (CD4⁺Foxp3⁺) in Peyer's patch, iEL, MLN and LPL of colitis mice and healthy mice 12 days after colitis induction. The data shown are the mean ± SEM from one experiment with five mice and was repeated three times with similar results. **p* < 0.05; ***p* < 0.01; ****p* < 0.001.

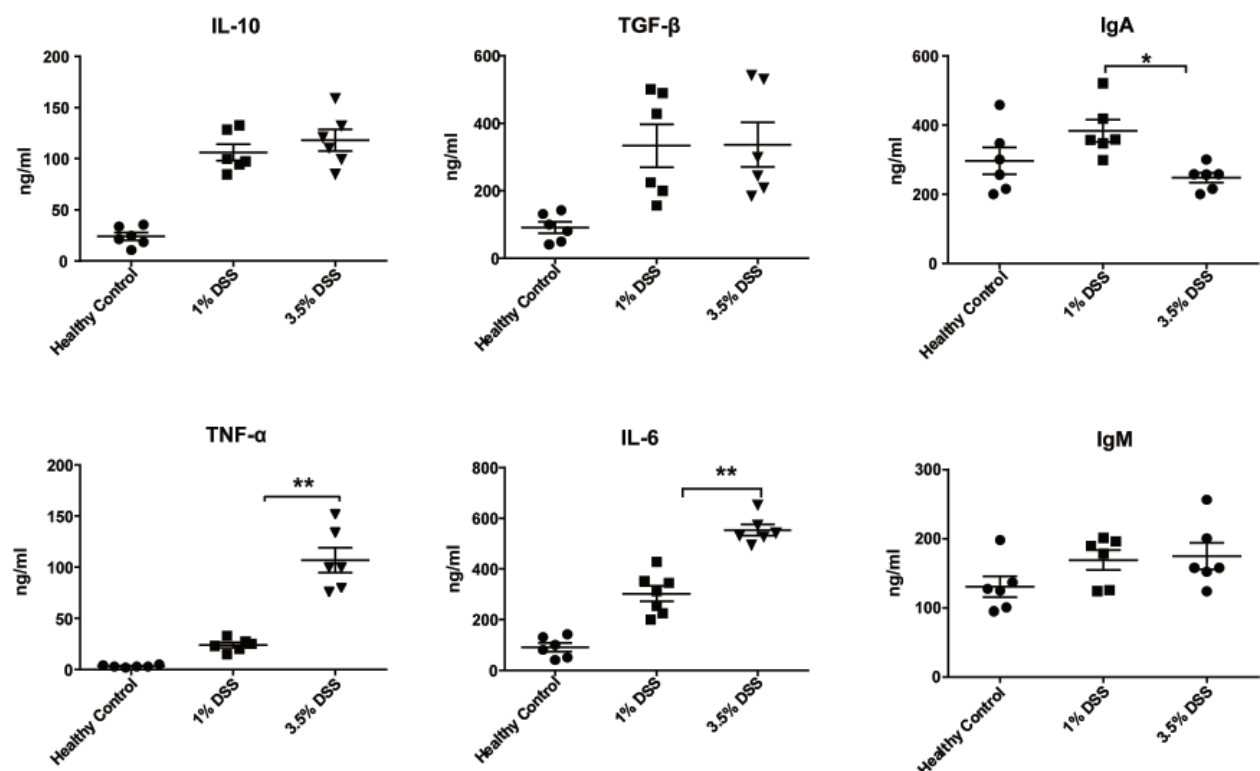


Figure 3. DSS-induced colitis induces significant changes in cytokines and antibodies within the gut. Colitis was induced as in Figure 1. On day 12, the intestines were flushed with 20 mL endotoxin and FCS free PBS. Mucus containing fluid was harvested and the level of IL-6, TNF- α , IL-10, TGF- β , IgM and IgA in the supernatant was determined by ELISA. Each data point represents a single mouse with the mean shown. Data shown are the mean ± SEM of six mice and was repeated three times with similar results. **p* < 0.05; ***p* < 0.01.

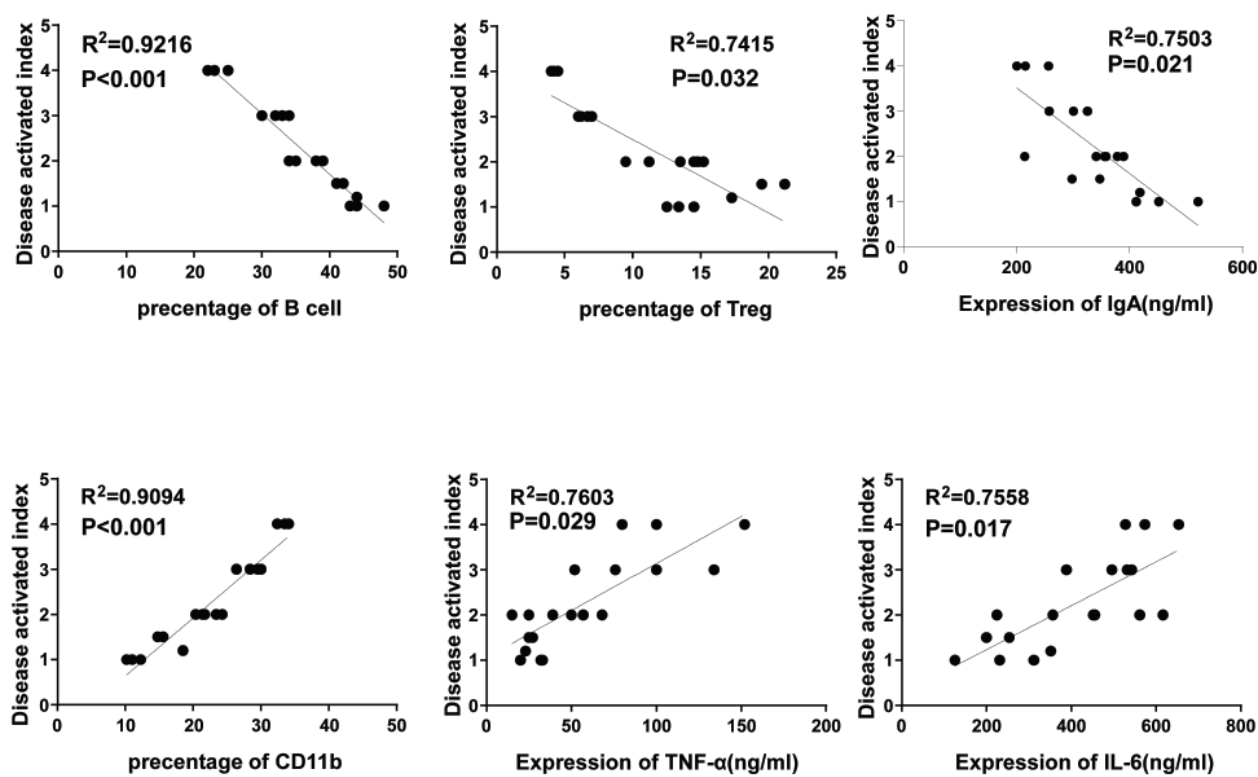


Figure 4. The expression of immune cells and cytokines is related to disease symptoms. Relative frequencies of B220⁺ B cells, CD11b⁺ cells, Tregs, IL-6, TNF- α , IgA and DAI in healthy and colitis mice. Each data point represents a single mouse with the mean shown. Data were repeated three times with similar results.

pro-inflammatory cytokines, including IL-6, and TNF- α , which are directly involved in the pathogenesis of UC (4,5). On the contrary, a protective role for B cells and serum Ig was described in the TCR- $\alpha^{-/-}$ spontaneous model of colitis (22) and DSS induced colitis (23). And also, Tregs are considered one of the most important immune cell regulators of intestinal homeostasis (15,24-27). Thus, the deficiency of GALT B cells and Tregs during 3.5% DSS may cause the infiltration of CD11b⁺ cells and lead to an irreversible colitis.

We next determined cytokine and antibody production by those immune cells during mild and severe colitis. We found that IL-10, TGF- β and IgM production in the gut mucus were increased during colitis, but there was no significant difference between mild and severe colitis, however, pro-inflammatory cytokines TNF- α and IL-6 were found to be significantly higher in the severe colitis (Figure 3). Noteworthy, IgA secreted in the gut mucus decreased in the severe colitis mice compared to the mild colitis mice (Figure 3). In order to identify the effector compartment and the regulator compartment during colitis, we performed statistical analysis between immune factors and DAI. Tregs, B cells and IgA had a negative relationship with DAI, while CD11b⁺ cells, IL-6 and TNF- α had a positive relationship with DAI (Figure 4).

Our results indicated that Tregs, B cells, and IgA produced had a regulatory function during colitis, which

can rescue colitis by confrontation of pro-inflammation cells and cytokines (Figure 3). However, during severe colitis, Tregs, B cells and IgA were exhausted in the acute phase (data not shown). They were not increased on recovery phase, thus CD11b⁺ cells and its secreted IL-6 and TNF- α were accumulated on lamina propria and epithelia, resulting in severe and irreversible colitis. These results give us a new prospect that patients have different degrees of colitis (28), both immune cells such as CD11b⁺ cells, B cells, Tregs and the immune factors produced by them are directly related to the symptoms of different degrees of colitis. Thus, the frequencies of immune cells and the level of immune factors may provide a new diagnosis of colitis. More importantly, the fact that sufficient Tregs, B cells and IgA are able to rescue colitis from pro-inflammatory factors activation while the deficiency of regulators leads to an irreversible colitis may provide innovative immune cell-based therapies for the treatment of colitis.

Acknowledgements

This work was supported by National Science Foundation of China (81273215, 91229110), the National Basic Research Program of China (973 Programs, 2011CB910404), the China Postdoctoral Science Foundation (2014M5502141), Specialized Research Fund for the Doctoral Program of Higher Education (20120071110046).

References

1. Garcia de Tena J, Espinosa LM, Alvarez-Mon M. Inflammatory bowel disease. *N Engl J Med.* 2002; 347:1982-1984; author reply 1982-1984.
2. Ni J, Chen SF, Hollander D. Effects of dextran sulphate sodium on intestinal epithelial cells and intestinal lymphocytes. *Gut.* 1996; 39:234-241.
3. Cheroutre H, Madakamutil L. Acquired and natural memory T cells join forces at the mucosal front line. *Nat Rev Immunol.* 2004; 4:290-300.
4. Sands BE. Inflammatory bowel disease: Past, present, and future. *Journal of gastroenterology.* 2007; 42:16-25.
5. Hibi T, Ogata H. Novel pathophysiological concepts of inflammatory bowel disease. *Journal of gastroenterology.* 2006; 41:10-16.
6. Sattler S, Ling GS, Xu D, Hussaarts L, Romaine A, Zhao H, Fossati-Jimack L, Malik T, Cook HT, Botto M, Lau YL, Smits HH, Liew FY, Huang FP. IL-10-producing regulatory B cells induced by IL-33 (Breg(IL-33)) effectively attenuate mucosal inflammatory responses in the gut. *J Autoimmun.* 2014; 50:107-122.
7. Suzuki K, Kawamoto S, Maruya M, Fagarasan S. GALT: Organization and dynamics leading to IgA synthesis. *Adv Immunol.* 2010; 107:153-185.
8. Chorny A, Puga I, Cerutti A. Innate signaling networks in mucosal IgA class switching. *Adv Immunol.* 2010; 107:31-69.
9. Kirkland D, Benson A, Mirpuri J, Pifer R, Hou B, DeFranco AL, Yarovinsky F. B cell-intrinsic MyD88 signaling prevents the lethal dissemination of commensal bacteria during colonic damage. *Immunity.* 2012; 36:228-238.
10. Rudensky AY. Regulatory T cells and Foxp3. *Immunol Rev.* 2011; 241:260-268.
11. Kawamoto S, Maruya M, Kato LM, Suda W, Atarashi K, Doi Y, Tsutsui Y, Qin H, Honda K, Okada T, Hattori M, Fagarasan S. Foxp3⁺ T cells regulate immunoglobulin a selection and facilitate diversification of bacterial species responsible for immune homeostasis. *Immunity.* 2014; 41:152-165.
12. Sonoda E, Matsumoto R, Hitoshi Y, Ishii T, Sugimoto M, Araki S, Tominaga A, Yamaguchi N, Takatsu K. Transforming growth factor beta induces IgA production and acts additively with interleukin 5 for IgA production. *J Exp Med.* 1989; 170:1415-1420.
13. Cazac BB, Roes J. TGF-beta receptor controls B cell responsiveness and induction of IgA *in vivo*. *Immunity.* 2000; 13:443-451.
14. Kuhn R, Lohler J, Rennick D, Rajewsky K, Muller W. Interleukin-10-deficient mice develop chronic enterocolitis. *Cell.* 1993; 75:263-274.
15. Rubtsov YP, Rasmussen JP, Chi EY, Fontenot J, Castelli L, Ye X, Treuting P, Siewe L, Roers A, Henderson WR, Jr., Muller W, Rudensky AY. Regulatory T cell-derived interleukin-10 limits inflammation at environmental interfaces. *Immunity.* 2008; 28:546-558.
16. Zigmond E, Bernshtein B, Friedlander G, Walker CR, Yona S, Kim KW, Brenner O, Krauthgamer R, Varol C, Muller W, Jung S. Macrophage-Restricted Interleukin-10 Receptor Deficiency, but Not IL-10 Deficiency, Causes Severe Spontaneous Colitis. *Immunity.* 2014.
17. Murthy SN, Cooper HS, Shim H, Shah RS, Ibrahim SA, Sedergran DJ. Treatment of dextran sulfate sodium-induced murine colitis by intracolonic cyclosporin. *Digestive diseases and sciences.* 1993; 38:1722-1734.
18. Wirtz S, Neufert C, Weigmann B, Neurath MF. Chemically induced mouse models of intestinal inflammation. *Nat Protoc.* 2007; 2:541-546.
19. Lefrancois L, Lycke N. Isolation of mouse small intestinal intraepithelial lymphocytes, Peyer's patch, and lamina propria cells. *Current protocols in immunology* (Coligan JE, ed.). 2001; Chapter 3: Unit 3.19.
20. Rose WA, 2nd, Sakamoto K, Leifer CA. Multifunctional role of dextran sulfate sodium for *in vivo* modeling of intestinal diseases. *BMC immunology.* 2012; 13:41.
21. Hall LJ, Faivre E, Quinlan A, Shanahan F, Nally K, Melgar S. Induction and activation of adaptive immune populations during acute and chronic phases of a murine model of experimental colitis. *Digestive diseases and sciences.* 2011; 56:79-89.
22. Mizoguchi A, Mizoguchi E, Smith RN, Preffer FI, Bhan AK. Suppressive role of B cells in chronic colitis of T cell receptor alpha mutant mice. *J Exp Med.* 1997; 186:1749-1756.
23. Yanaba K, Yoshizaki A, Asano Y, Kadono T, Tedder TF, Sato S. IL-10-producing regulatory B10 cells inhibit intestinal injury in a mouse model. *Am J Pathol.* 2011; 178:735-743.
24. Schmitt EG, Haribhai D, Williams JB, et al. IL-10 produced by induced regulatory T cells (iTregs) controls colitis and pathogenic ex-iTregs during immunotherapy. *J Immunol.* 2012; 189:5638-5648.
25. Eastaff-Leung N, Mabarrack N, Barbour A, Cummins A, Barry S. Foxp3⁺ regulatory T cells, Th17 effector cells, and cytokine environment in inflammatory bowel disease. *J Clin Immunol.* 2010; 30:80-89.
26. Griseri T, Asquith M, Thompson C, Powrie F. OX40 is required for regulatory T cell-mediated control of colitis. *J Exp Med.* 2010; 207:699-709.
27. Uhlig HH, Coombes J, Mottet C, Izcue A, Thompson C, Fanger A, Tannapfel A, Fontenot JD, Ramsdell F, Powrie F. Characterization of Foxp3⁺CD4⁺CD25⁺ and IL-10-secreting CD4⁺CD25⁺ T cells during cure of colitis. *J Immunol.* 2006; 177:5852-5860.
28. Hanauer SB. Inflammatory bowel disease. *N Engl J Med.* 1996; 334:841-848.

(Received August 12, 2014; Revised October 5, 2014; Re-revised October 9, 2014; Accepted October 10, 2014)

Involvement of the central monoaminergic system in the antidepressant-like effect of catalpol in mice

Junming Wang^{1,2,*}, Ying Cui¹, Weisheng Feng^{1,*}, Yueyue Zhang¹, Guifang Wang¹, Xingxing Wang¹, Gai Zhou¹

¹ Collaborative Innovation Center for Respiratory Disease Diagnosis and Treatment & Chinese Medicine Development of Henan Province, Henan University of Traditional Chinese Medicine, Zhengzhou, Henan, China;

² College of Chemistry and Molecular Engineering, Zhengzhou University, Zhengzhou, Henan, China.

Summary

Catalpol is a natural iridoid glycoside with diverse bioactivities that is found in abundance in *Rehmannia glutinosa* Libosch. (Scrophulariaceae). The present study assessed whether catalpol treatment (5, 10, or 20 mg/kg for 14 days by intragastric administration (*i.g.*)) has an antidepressant-like effect on mice performing the forced swim test (FST), tail suspension test (TST), open field test (OFT), and tests for reversal of reserpine-induced ptosis, akinesia, and hypothermia. This study also examined the potential role that catalpol plays in the cerebral monoaminergic system. Results indicated that catalpol administration produced an antidepressant-like effect in mice, as indicated by the reduced duration of immobility in the FST and TST, but it had no effect on locomotor activity in the OFT. Catalpol treatment significantly counteracted the decrease in rectal temperature, akinesia, and eyelid ptosis induced by reserpine. Moreover, catalpol increased levels of serotonin (5-HT) and its metabolite 5-hydroxyindoleacetic acid (5-HIAA) in the brains of mice, but it did not affect levels of norepinephrine (NE) or dopamine (DA). These antidepressant-like effects of catalpol are essentially similar to the effects of the clinical antidepressant fluoxetine hydrochloride (FH). This is the first study to indicate that catalpol has an antidepressant-like effect and that its action may be mediated by the central serotonergic system, and not by noradrenergic or dopaminergic systems.

Keywords: Catalpol, antidepressant-like effect, monoaminergic system, serotonergic system, reserpine

1. Introduction

Depression is a common but serious illness that can impact people's lives. Various antidepressants, including tricyclic antidepressants, monoamine oxidase inhibitors, and norepinephrine (NE) reuptake inhibitors, are widely available on the pharmaceutical market. Although these drugs have excellent efficacy, most frequently produce undesirable adverse reactions (1-3). Thus, an urgent task is to search for more promising antidepressants

from natural medicinal plants in order to meet the needs of clinically depressed patients.

The dried root of *Rehmannia glutinosa* Libosch. (Scrophulariaceae) has been widely used as a traditional Chinese medicine to treat behavioral diseases, including depression. Catalpol (Figure 1A) is a major bioactive compound that is found in abundance in the dried root of *R. glutinosa*. This compound has been found to have neuroprotective action, ameliorate cognition deficits, and have potential as a treatment for inflammation-related neurodegenerative diseases (4-6). A previous study reported that the powdered dried root of *R. glutinosa* had an antidepressant-like effect in mice (7). However, no studies have specifically examined the antidepressant-like effect of catalpol from the dried root of *R. glutinosa*. Moreover, whether the mechanism of catalpol's action is related to the central monoaminergic system has not been known.

*Address correspondence to:

Dr. Junming Wang and Dr. Weisheng Feng, College of Pharmacy, Henan University of Traditional Chinese Medicine, East Jinshui Road & Boxue Road, Zhengzhou 450046, China. E-mail: mjw98_2010@163.com (Wang JM); fwsh@hactm.edu.cn (Feng WS)

The present study sought to assess the antidepressant-like effect of catalpol and to behaviorally and pharmacologically determine the role that it plays in the central monoaminergic system.

2. Materials and Methods

2.1. Experimental animals

Male Kunming (KM) male mice (18–22 g) were purchased from the Experimental Animal Center of Henan Province (Zhengzhou, Henan Province, China). Animals were given rodent laboratory chow and water *ad libitum* and maintained under controlled conditions with a temperature of 22 ± 1°C, relative humidity of 60 ± 10%, and a 12/12 h light/dark cycle (lights on at 7:00 a.m.). All procedures were in strict accordance with Chinese legislation on the use and care of laboratory animals and with guidelines established by the Institute for Experimental Animals of Henan University of Traditional Chinese Medicine. This study was approved by the committee for animal experiments of Henan University of Traditional Chinese Medicine.

2.2. Reagents

Catalpol with a purity of 99.5% according to high-performance liquid chromatography (HPLC) was provided by Shanghai Jinsui Biotechnology Co., Ltd. (Shanghai, China). Reserpine with a purity of more than 98% according to HPLC was purchased from Xi'an Senzhuo Biotech Co., Ltd. (Xi'an, Shanxi Province, China). Fluoxetine hydrochloride (FH) was purchased from Changzhou Siyao Pharmaceuticals Co., Ltd. (Changzhou, Jiangsu Province, China).

Mouse norepinephrine (NE), dopamine (DA), serotonin (5-HT), and 5-hydroxy-indoleacetic acid (5-HIAA) enzyme-linked immunoassay (ELISA) kits were purchased from R&D Systems China Co., Ltd. (Shanghai, China).

2.3. Animal treatment protocol

Male mice were randomly divided into several groups of 10 mice each. Mice in the treated groups were orally administered catalpol (5, 10, or 20 mg/kg) or the positive drug FH (10 mg/kg) daily for 14 consecutive days by intragastric administration (*i.g.*). Mice in the vehicle group (*i.e.* not treated with catalpol) were orally administered (*p.o.*) 0.5% CMC-Na daily. A tail suspension test (TST), forced swim test (FST), open field test (OFT), and tests for reversal of reserpine-induced ptosis, akinesia and hypothermia were used to observe the antidepressant-like effects of catalpol in mice 1 h after final administration. After the OFT, TST, and FST, animals were immediately sacrificed by cervical dislocation. Brain tissue was quickly

removed and kept on ice to analyze levels of the central monoamine neurotransmitters NE, DA, and 5-HT and the 5-HT metabolite 5-HIAA.

2.4. Tail suspension test (TST)

The total duration of immobility induced by tail suspension was measured in accordance with the methods of Steru *et al.* (8). Acoustically and visually isolated mice were suspended 50 cm above the floor with adhesive tape placed approximately 1 cm from the tip of the tail. The duration of immobility was recorded during the last 4 min of the 6 min testing period. Mice were considered immobile only when they hung passively and they were completely motionless.

2.5. Forced swim test (FST)

The forced swim test was similar to tests described previously (9,10). The mice were individually placed in glass cylinders (height, 25 cm; diameter, 10 cm) containing 10 cm of water (22 ± 1°C). The duration of immobility was defined as the time the mouse spent without struggling, floating motionless or making only small movements necessary to keep its head above water during the last 4 min of the 6 min testing period. The water was replaced following each trial.

2.6. Open field test (OFT)

Locomotor activity was observed *via* a slightly modified form of the open field test (OFT) (11,12). Briefly, the locomotor activity of the mice was measured using a box (40 × 60 × 50 cm) with the floor divided into 12 identical squares illuminated with light from the ceiling. Mice were placed in the central square and the total number of squares entered was recorded for 3 min. The open field arena was cleaned following each trial.

2.7. Tests for reversal of reserpine-induced ptosis, akinesia, and hypothermia

Tests for reversal of reserpine-induced ptosis, akinesia, and hypothermia were in accordance with the methods of Qiu *et al.* (13). Mice were treated with reserpine (2.5 mg/kg, *i.p.*) 1 h after the administration of catalpol. Three parameters of akinesia, the degree of palpebral ptosis, and the rectal temperature were recorded 4 h after the administration of reserpine. The degree of palpebral ptosis was evaluated according to the following rating scale: 0, eyes open; 1, eyes one-quarter closed; 2, eyes half-closed; 3, eyes three-quarters closed; and 4, eyes completely closed. To measure akinesia, mice were placed in the center of a circle (diameter, 7.5 cm). The total time the mice remained within the circle during a 1 min period was measured.

2.8. Measurement of monoamine neurotransmitter levels

Brain levels of NE, DA, 5-HT, and the 5-HT metabolite 5-HIAA were measured with ELISA kits according to the manufacturer's protocols (14-16). The levels of NE, DA, 5-HT, and 5-HIAA were expressed as ng/g in wet weight tissue. Sample preparation was as follows: 100 mg of tissue was rinsed with 1× phosphate buffered solution (PBS), homogenized in 1 mL of 1× PBS, and stored overnight at -20°C. After two freeze-thaw cycles were used to rupture the cell membranes, the homogenates were centrifuged for 5 min at 5000×g, 4°C. The supernate was assayed and immediately removed. The sample was thawed and centrifuged again before measurement. Repeated freeze-thaw cycles were avoided.

2.9. Statistical analysis

All experimental data are expressed as the mean ± standard error of mean (SEM). Significant differences among experimental groups were compared using one-way analysis of variance (ANOVA) followed by least significant difference (LSD) test ($p < 0.05$) using the Statistics Package for Social Science (SPSS) program Version 13.0.

3. Results

3.1. Catalpol shortens the duration of immobility in the TST and FST

The duration of immobility in the TST and FST was 93.8 ± 4.9 s and 102.4 ± 6.8 s, respectively, for the vehicle group. Compared to the vehicle group, catalpol (5, 10, and 20 mg/kg, i.g.) significantly shortened the duration of immobility both in TST (Figure 1B) and in FST (Figure 1C). Fluoxetine hydrochloride (FH, 10 mg/kg, i.g.) that was used as a positive control also caused a significant shortening of the duration of immobility in both the TST and FST (Figures 1B and 1C). There was no significant difference in the duration of immobility caused by a similar dose of catalpol or FH. Results indicated that catalpol causes antidepressant-like action and that catalpol is comparable to the positive drug FH.

3.2. Catalpol has no effect on locomotor activity

The effect of catalpol on the locomotor activity of mice is shown in Figure 2. The locomotion measured in the OFT was 80.3 ± 6.7 for the vehicle group. Neither catalpol nor FH affected locomotor activity at doses that significantly shortened the duration of immobility in the TST and FST.

3.3. Catalpol attenuates reserpine-induced ptosis, akinesia, and hypothermia

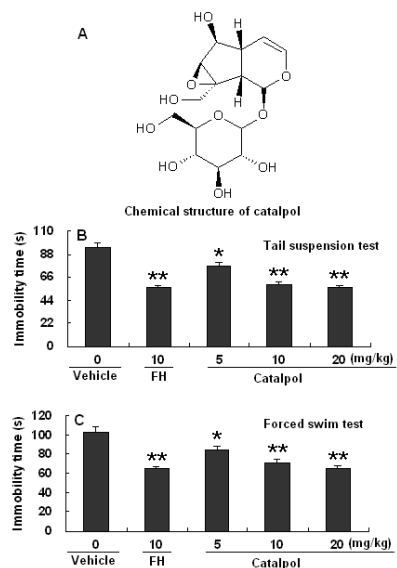


Figure 1. Chemical structure of catalpol (A), and its effect on the duration of immobility of mice in the tail suspension (B) and forced swim (C) tests. Data are expressed as the mean ± SEM ($n = 10$). Significant differences compared to the vehicle group were indicated by * $p < 0.05$ and ** $p < 0.01$.

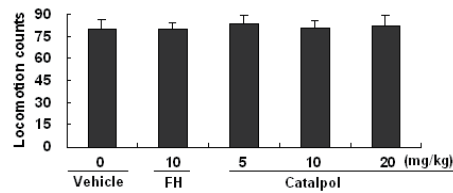


Figure 2. Effect of catalpol on the locomotor activity of mice in the open field test. Data are expressed as the mean ± SEM ($n = 10$).

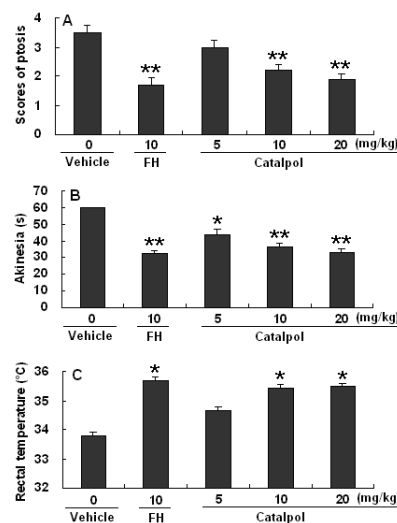


Figure 3. Effects of catalpol on reserpine induced ptosis, akinesia, and hypothermia in mice. Data are expressed as the mean ± SEM ($n = 10$). Significant differences compared to the vehicle group were indicated by * $p < 0.05$ and ** $p < 0.01$.

The effects of catalpol on reserpine induced ptosis, akinesia, and hypothermia are shown in Figure 3. Reserpine induced ptosis was 3.5 ± 0.3 , akinesia was

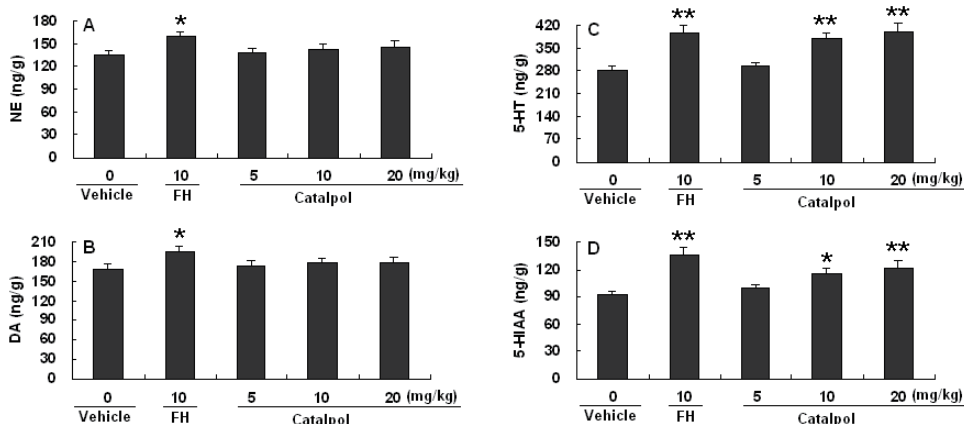


Figure 4. Effect of catalpol on central monoamine neurotransmitters and a major metabolite. Data are expressed as the mean \pm SEM ($n = 10$). Significant differences compared to the vehicle group were indicated by * $p < 0.05$ and ** $p < 0.01$.

60 s, and hypothermia was $33.8 \pm 0.1^\circ\text{C}$ in the vehicle group. Compared to the vehicle group, catalpol (10, 20 mg/kg) significantly decreased reserpine-induced ptosis and significantly counteracted reserpine-induced hypothermia. Catalpol (5, 10, and 20 mg/kg) significantly reduced the duration of reserpine-induced akinesia in comparison to that in the vehicle group. FH (10 mg/kg) also significantly counteracted the hypothermia, ptosis, and akinesia induced by reserpine.

3.4. Catalpol increases levels of monoamine neurotransmitters and a major metabolite in mice

The effect of catalpol on central monoamine neurotransmitters and a major metabolite of 5-HT in mice is shown in Figure 4. The levels of 5-HT, 5-HIAA, NE, and DA in the brains of mice in the vehicle group were 280.3 ± 11.7 , 92.2 ± 3.9 , 134.7 ± 5.8 , 168.8 ± 7.6 ng/g, respectively. Compared to the vehicle group, catalpol (10, 20 mg/kg) treatment significantly increased the levels of 5-HT and 5-HIAA, but not NE or DA, in the brains of mice, while FH treatment significantly affected levels of NE, DA, 5-HT, and 5-HIAA.

4. Discussion

Both the TST and FST are widely used to screen drugs for antidepressant activity (8-10). In animals, immobility as a result of the forced swim and tail suspension is similar to human depression and is amenable to reversal by antidepressant drugs (8-10). These models are based on the despair or helpless behavior of animals in an inescapable situation or a confined space. Results from these models revealed that catalpol has significant antidepressant-like effects in a dose-dependent manner.

In these behavioral tests, false-positive results are occasionally obtained with agents that stimulate locomotor activity (17). Therefore, the present study determined whether catalpol had excitatory or inhibitory action on the central nervous system. Catalpol had no

effect on the spontaneous locomotor activity of mice, indicating that catalpol had no excitatory or inhibitory action on the central nervous system at the doses used. This rules out the possibility of false positive results on the TST and FST. Catalpol shortened the duration of immobility in the TST and FST; this is likely due to antidepressant-like action and not psychomotor-stimulant action.

Reserpine is an antihypertensive drug that depletes neuronal storage granules of biogenic amines in the brains of rodents and that produces a clinically significant depression-like state (13). Mice become hypothermic, akinetic, and diarrhetic, with eyelid drooping, in response to reserpine. Reserpine irreversibly inhibits the vesicular uptake of monoamine neurotransmitters such as NA, DA, and 5-HT (13-17). The symptoms are reversed by major classes of antidepressant drugs. The present results revealed that catalpol counteracts, in a dose-dependent manner, the ptosis, akinesia, and hypothermia induced by reserpine in mice. This indicates that catalpol has an antidepressant-like effect and may have an effect on monoamine neurotransmitters. Therefore, this study further explored the antidepressant action of catalpol by using ELISA to determine the levels of monamine neurotransmitters in the brains of mice. Results indicated that catalpol increased the levels of central 5-HT and its metabolite 5-HIAA but did not affect levels of NE and DA in mice, suggesting that the antidepressant-like effects of catalpol may be mediated by the central serotonergic system and not by the noradrenergic or dopaminergic systems.

In conclusion, this is the first study to reveal that catalpol has an antidepressant-like effect in mice and that its action may involve upregulation of the central serotonergic system.

Acknowledgements

This work was financially supported by the National

Science & Technology Pillar Program of China under the 12th Five-year Plan (2011BAI06B02), the National Natural Science Foundation of China (81473368), the Innovation Program for Science & Technology Leading Talents of Zhengzhou City in China's Henan Province (121PLJRC534), the National Science Foundation for Post-doctoral Scientists of China (2012M521412), and the Program for Innovative Research Teams (in Science and Technology) of Henan University of Traditional Chinese Medicine (2011XCXTD01).

References

1. Whiskey E, Taylor D. A review of the adverse effects and safety of noradrenergic antidepressants. *J Psychopharmacol.* 2013; 27:732-739.
2. Molyneux PD. Tricyclic antidepressants reduce frequency of tension-type and migraine headaches compared with placebo, and intensity of headaches compared with SSRIs, but cause greater adverse effects. *Evid Based Med.* 2011; 16:75-76.
3. Simon G. Review: Second-generation antidepressants have similar effectiveness, but specific adverse effects differed. *Evid Based Med.* 2009; 14:82.
4. Chen W, Li X, Jia LQ, Wang J, Zhang L, Hou D, Wang J, Ren L. Neuroprotective activities of catalpol against CaMKII-dependent apoptosis induced by LPS in PC12 cells. *Br J Pharmacol.* 2013; 169:1140-1152.
5. Zhang XL, Jiang B, Li ZB, Hao S, An LJ. Catalpol ameliorates cognition deficits and attenuates oxidative damage in the brain of senescent mice induced by D-galactose. *Pharmacol Biochem Behav.* 2007; 88:64-72.
6. Zhang X, Jin C, Li Y, Guan S, Han F, Zhang S. Catalpol improves cholinergic function and reduces inflammatory cytokines in the senescent mice induced by D-galactose. *Food Chem Toxicol.* 2013; 58:50-55.
7. Miao JX, Zhang XL, Ji XN, Miao MS. Anti-depressant effect of fresh *Rehmannia glutinosa* Libosch. powder on mice. *Zhong Yi Xue Bao.* 2011; 26:813-814. (in Chinese)
8. Steru L, Chermat R, Thierry B, Simon P. The tail suspension test: A new method for screening antidepressants in mice. *Psychopharmacology (Berl).* 1985; 85:367-370.
9. Piotrowska A, Siwek A, Wolak M, Pochwat B, Szewczyk B, Opoka W, Poleszak E, Nowak G. Involvement of the monoaminergic system in the antidepressant-like activity of chromium chloride in the forced swim test. *J Physiol Pharmacol.* 2013; 64:493-498.
10. Wang Z, Gu J, Wang X, Xie K, Luan Q, Wan N, Zhang Q, Jiang H, Liu D. Antidepressant-like activity of resveratrol treatment in the forced swim test and tail suspension test in mice: The HPA axis, BDNF expression and phosphorylation of ERK. *Pharmacol Biochem Behav.* 2013; 112:104-110.
11. Porsolt RD, Bertin A, Jalfre M. Behavioral despair in mice: A primary screening test for antidepressants. *Arch Int Pharmacodyn Ther.* 1977; 229:327.
12. Zeni AL, Zomkowski AD, Maraschin M, Tasca CI, Rodrigues AL. Evidence of the involvement of the monoaminergic systems in the antidepressant-like effect of *Aloysia gratissima*. *J Ethnopharmacol.* 2013; 148:914-920.
13. Qiu F, Zhong X, Mao Q, Huang Z. The antidepressant-like effects of paeoniflorin in mouse models. *Exp Ther Med.* 2013; 5:1113-1116.
14. Zhou XJ, Liu M, Yan JJ, Cao Y, Liu P. Antidepressant-like effect of the extracted of Kai Xin San, a traditional Chinese herbal prescription, is explained by modulation of the central monoaminergic neurotransmitter system in mouse. *J Ethnopharmacol.* 2012; 139:422-428.
15. Xu H, Zhao B, Cui Y, Lim MY, Liu P, Han L, Guo H, Lao L. Effects of moxa smoke on monoamine neurotransmitters in SAMP8 mice. *Evid Based Complement Alternat Med.* 2013; 2013:178067.
16. Wang S, Qi F, Li J, Zhao L, Li A. Effects of Chinese herbal medicine Ningdong granule on regulating dopamine (DA)/serotonin (5-HT) and gamma-amino butyric acid (GABA) in patients with Tourette syndrome. *Biosci Trends.* 2012; 6:212-218.
17. Bourin M1, Fiocco AJ, Clenet F. How valuable are animal models in defining antidepressant activity? *Hum Psychopharmacol.* 2001; 16:9-21.

(Received February 23, 2014; Revised May 30, 2014;
Accepted October 11, 2014)

Protection of *Angelica sinensis* (Oliv) Diels against hepatotoxicity induced by *Dioscorea bulbifera* L. and its mechanism

Chengwei Niu¹, Junming Wang³, Lili Ji^{1,2,*}, Zhengtao Wang^{1,2}

¹ The MOE Key Laboratory for Standardization of Chinese Medicines, The Shanghai Key Laboratory for Complex Prescription, and The SATCM Key Laboratory for New Resources and Quality Evaluation of Chinese Medicines, Institute of Chinese Materia Medica, Shanghai University of Traditional Chinese Medicine, Shanghai, China;

² Shanghai R&D Centre for Standardization of Chinese Medicines, Shanghai, China;

³ School of Pharmacy, Henan University of Traditional Chinese Medicine, Zhengzhou, Henan, China.

Summary

Dioscorea bulbifera L., a traditionally used medicinal plant in China, is reported to induce hepatotoxicity. The present study is designed to investigate the protection of an ethanol extract of *Angelica sinensis* (Oliv) Diels (AE) against an ethyl acetate fraction of *D. bulbifera* (EF)-induced liver injury and its engaged mechanism. High performance liquid chromatography (HPLC) analysis showed that the amount of diosbulbin B in EF was 16.03% and ferulic acid in AE was 0.18%. EF (350 mg/kg) increased serum alanine/aspartate aminotransferase (ALT/AST), alkaline phosphatase (ALP) activities and total bilirubin (TB) amount, while AE inhibited such an increase. Liver histological evaluation showed that AE prevented development of severe hepatic lesions induced by EF. Further results showed that EF decreased the expression of Bcl-2 and induced the cleaved activation of caspase-9 and -3, and all those effects were reversed by AE. AE also reversed EF-induced decreased expression of the inhibitor of kappa B (IkB), superoxide dismutase (SOD), and glutathione peroxidase (GPx). Taken together, our results demonstrate that AE can prevent EF-induced hepatotoxicity via preventing apoptosis, meanwhile IkB, SOD, and GPx may be involved in such protection.

Keywords: *Dioscorea bulbifera* L., *Angelica sinensis* (Oliv) Diels, hepatotoxicity, apoptosis, oxidative stress injury

1. Introduction

Dioscorea bulbifera L. is a medicinal plant distributed in the tropics and the subtropical zone of Asia. It is used in folk medicine to treat thyroid disease (especially goiter) and cancer, as well as some other syndromes involving "toxic heat," such as sore throat, struma (1,2). In spite of its unique clinical benefit, its potential toxicity has been an increasing concern to clinical doctors. *D. bulbifera* has been documented to cause intoxication and is lethal in animals and humans (3-5). It has been elucidated that the main toxic target organ of *D. bulbifera* is liver, and its exposure could lead to severe liver damage, including

liver swelling, fatty degeneration, even animal death (3-5). Intake of *D. bulbifera* has also been associated with high occurrence of jaundice or toxic hepatitis in humans (3). It is reported that diterpene lactones are the main hepatotoxins existing in the rhizome of *D. bulbifera* (6,7). So far, some structural analogues of diterpene lactones have been identified in *D. bulbifera* and of which the amount of diosbulbin B is the highest (8-10).

Danggui, the dried root of *Angelica sinensis* (Oliv) Diels, is a commonly used medicinal herb. It can enrich blood, promote blood circulation and clinically is used to treat blood deficiency patterns and menstrual disorders such as dysmenorrhea and irregular menstrual cycles (11,12). In recent years, pharmacological research has focused on elucidating the antioxidative, anti-cancer and neuroprotective properties of *A. sinensis* (13-15). In addition, *A. sinensis* also showed a hepatoprotective effect, especially its active component ferulic acid (16-18). In the present study, we investigated the protection

*Address correspondence to:

Dr. Lili Ji, Institute of Chinese Materia Medica, Shanghai University of Traditional Chinese Medicine, 1200 Cailun Road, Shanghai, 201203, China.
E-mail: lichenyue1307@126.com

of the ethanol extract of *A. sinensis* (AE) against *D. bulbifera* (EF)-induced liver injury and its engaged mechanism.

2. Materials and Methods

2.1. Drugs and reagents

The rhizomes of *D. bulbifera* were collected in Qingyang, Anhui Province and authenticated by Prof. Shou-Jin Liu (Anhui College of Traditional Chinese Medicine, Anhui, China). The radixes of *A. sinensis* were purchased from Yanghetang drugstore (Shanghai) and authenticated by Associate Prof. Li-Hong Wu (Shanghai University of Traditional Chinese Medicine, Shanghai, China). The identified specimens were deposited in the herbarium of Institute of Chinese Materia Medica, Shanghai University of Traditional Chinese Medicine. Diosbulbin B and ferulic acid were purchased from Shanghai Tauto Biotech Co., Ltd. Methanol and acetonitrile (HPLC Grade) were purchased from Fisher Chemical. Antibodies against Bcl-2, caspase-9, caspase-3, I_KB and β-actin were all purchased from Cell Signaling Technology (Danvers, MA, USA). Rabbit polyclonal antibody against superoxide dismutase (SOD) was purchased from Abcam (Cambridge, MA, USA). Mouse monoclonal antibody against glutathione peroxidase (GPx) was purchased from Santa Cruz (Santa Cruz, CA, USA). Peroxidase-conjugated goat anti-Rabbit IgG (H + L) and anti-mouse IgG (H + L) were purchased from Jackson ImmunoResearch (West Grove, PA, USA). Pre-stained protein marker was purchased from Fermentas (Burlington, Ontario, Canada). Nitrocellulose membranes were purchased from Bio-Rad (Hercules, CA, USA) and an enhanced chemiluminescence detection system was obtained from Millipore Corporation (Billerica, MA, USA).

2.2. Experimental animals

Specific pathogen free male ICR mice (18-22 g body weight) were purchased from the Chinese Academy of Sciences. The mice were fed with a standard laboratory diet and given free access to tap water, kept in a controlled room temperature ($22 \pm 1^\circ\text{C}$), humidity ($65 \pm 5\%$), and a 12:12-h light/dark cycle. All mice receive humane care in compliance with the institutional animal care guidelines approved by the Experimental Animal Ethical Committee of Shanghai University of Traditional Chinese Medicine.

2.3. Samples and preparation of extracts

Preparation of ethyl acetate fraction from *D. bulbifera* (EF): The powder was soaked in 80% ethanol (w/v = 1:10) for 2 h at room temperature. The macerated plant material was extracted at 70-80°C and refluxed for 2 h,

and then filtered through a cheese cloth. The residue was extracted as described previously (19). The combined filtrates were then evaporated to be free of alcohol using a rotary evaporator under reduced pressure at 50°C. The extracts were then partitioned with ethyl acetate to yield an ethyl acetate solution. After evaporation of solvents, an ethyl acetate fraction was achieved and stored in 70% ethanol.

Preparation of ethanol extract of *A. sinensis* (AE): The powder was soaked in 70% ethanol for 2 h at room temperature, and then percolated slowly until percolating liquid was colorless. Extracted liquid was evaporated using a rotary evaporator under reduced pressure at 50°C and adjusted to 1 mg/mL of raw material with 70% ethanol.

2.4. HPLC analysis

Analysis was carried out on a HPLC instrument (Agilent) consisting of an autosampler, quaternary pump, column heater compartment and diode array detection (DAD) with an on-line degasser. Chromatographic separation was achieved on an ultimate TMXB-C 18 column for diosbulbin B and CAPCELL PAK C18 column for ferulic acid (4.6 × 250 mm, 5 μm). The mobile phase consisted of acetonitrile and water (v/v = 25:75) for diosbulbin B or acetonitrile and 0.085% phosphoric acid (v/v = 17:83) for ferulic acid with a flow rate of 1.0 mL/min. Column temperature was set at 25°C and detection was carried out by UV absorbance at 210 nm for diosbulbin B and 323 nm for ferulic acid.

To obtain a calibration curve for diosbulbin B or ferulic acid, standard solutions were prepared in a range of 7.8-250 μg/mL for diosbulbin B and 2.7-173.6 μg/mL for ferulic acid on a column, and a 10 μL aliquot was injected. The samples were prepared and an aliquot (10 μL) each was injected into the above system respectively. The contents of diosbulbin B and ferulic acid in the respective extract were obtained using the calibration curves.

2.5. Treatment protocol

Mice were orally pre-administered AE suspended in 0.5% sodium carboxyl methyl cellulose (CMC-Na) (180, 360, or 720 mg/kg per day) for 6 consecutive days. Four hours after the treatment with AE on the last day, a single dose of EF (350 mg/kg, suspended in 0.5% CMC-Na) was administered orally. 0.5% CMC-Na was used as vehicle control. Twenty-four hours later, blood samples were collected by extirpating the eyeball. Mice were then sacrificed; and their livers were removed for further research.

2.6. Serum biomarkers for liver injury

Blood samples obtained from mice of all groups were

allowed to coagulate for 2 h on ice. Serum was then isolated following centrifugation at $840 \times g$ for 15 min. Serum alanine/aspartate aminotransferase (ALT/AST), alkaline phosphatase (ALP) activities and total bilirubin (TB) amounts were measured with kits purchased from Nanjing Jiancheng Bioengineering Institute (Nanjing, China) according to the manufacturer's instructions.

2.7. Histological examination

Portions of the liver were fixed in 10% formalin and embedded in paraffin. Samples were subsequently sectioned five micrometers thick and stained with hematoxylin-eosin (HE) for further histological analysis.

2.8. Western blot analysis

Liver tissue (approximately 25 mg) was homogenized in 0.5 mL, ice-cold lysis buffer containing 50 mM Tris, pH 7.5, 150 mM NaCl, 1 mM EDTA, 20 mM NaF, 0.5% NP-40, 10% glycerol, 1 mM phenylmethylsulfonyl fluoride 10 μ g/mL aprotinin, 10 μ g/mL leupeptin, 10 μ g/mL pepstatin A and incubated on ice for 10 min. The liver homogenate was centrifuged at 10,000 $\times g$ for 20 min at 4°C and protein concentration of the resulting supernatant was determined by the Bradford method. Two samples of each group were subjected to SDS-PAGE and then electrophoretically transferred onto a nitrocellulose membrane. Nonspecific binding was blocked for 1 h with 5% non-fat milk in Tris-buffered saline Tween-20 (TBST) (10 mM Tris, pH 7.5, 100 mM NaCl, 0.1% Tween-20), and then blots were incubated with primary antibody and secondary antibody. Immunoblots were visualized using a chemiluminescent reagent. The densities of the bands were normalized using a corresponding β -actin density as an internal control.

2.9. Statistical analysis

All experimental data were expressed as mean \pm standard error (S.E.). Significant differences were determined by One-Way ANOVA. $p < 0.05$ was considered as a statistically significant difference.

3. Results

3.1. HPLC analysis of plant extract

Our previous study showed that diosbulbin B is the main hepatotoxic chemical compound in *D. bulbifera* (19). Ferulic acid is the main active component in *A. sinensis*. Measurement of diosbulbin B and ferulic acid were used to control the quality of EF and AE extracts in the present study, respectively. The chemical structures of diosbulbin B and ferulic acid are shown in Figure 1A and Figure 2A. As shown in Figures 1B-

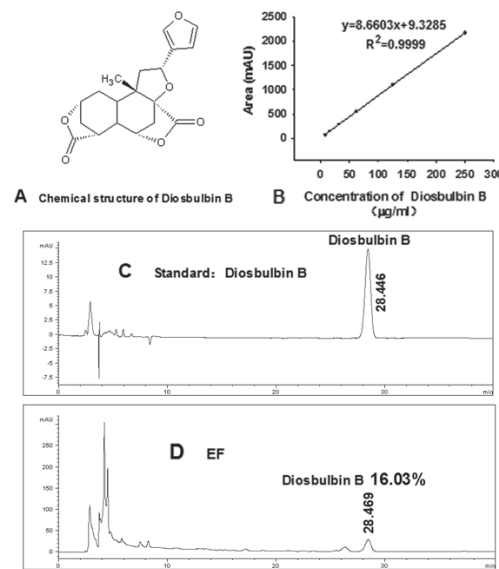


Figure 1. Chemical structure of diosbulbin B and the amount of diosbulbin B in EF. (A) Chemical structure of diosbulbin B. (B) Calibration curve of diosbulbin B. (C) HPLC chromatogram of diosbulbin B. (D) HPLC chromatogram of EF.

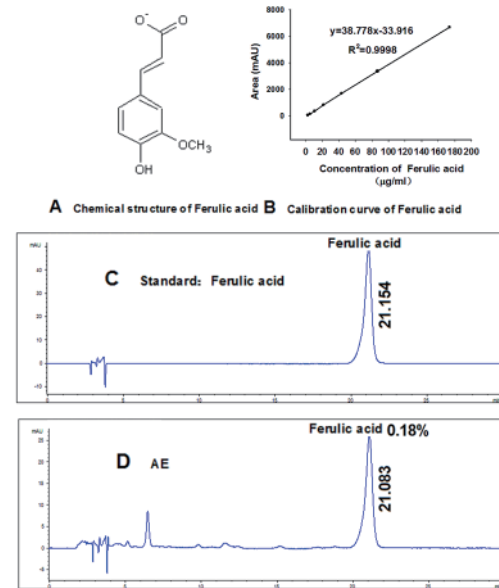


Figure 2. Chemical structure of ferulic acid and the amount of ferulic acid in AE. (A) Chemical structure of ferulic acid. (B) Calibration curve of ferulic acid. (C) HPLC chromatogram of ferulic acid. (D) HPLC chromatogram of AE.

1D and Figures 2B-2D, the amount of diosbulbin B in EF was 16.03% and ferulic acid in AE was 0.18% as determined by HPLC-DAD.

3.2. AE reversed EF-induced increase of ALT, AST, and ALP activities and TB amount

As shown in Figure 3, EF (350 mg/kg) increased serum ALT, AST, and ALP activities and TB amount as compared with control, while pretreatment with 360 mg/kg, 720 mg/kg of AE could obviously inhibit

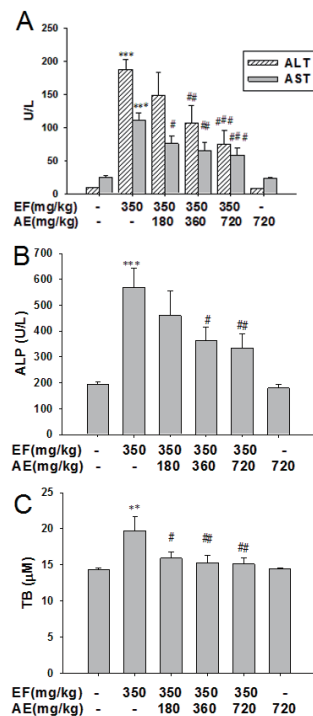


Figure 3. Serum ALT, AST, and ALP activities and TB amount in EF-treated mice with or without preadministration of AE. (A) Serum ALT and AST activities. (B) Serum ALP activity. (C) Serum TB amount. Data are shown as mean \pm S.E. ($n = 7-12$). ** $p < 0.01$, *** $p < 0.001$ versus control group, # $p < 0.05$, ## $p < 0.01$, ### $p < 0.001$, versus EF-treated group.

such an EF-induced increase. In contrast, there were no significant differences in the activities of ALT, AST, and ALP and level of TB in mice treated with AE (720 mg/kg) alone when compared with control.

3.3. Histological analysis of liver tissue

The livers from control mice appear normal (Figure 4a). In contrast to control mice, the mice treated with EF exhibited severe liver damage, indicated by intrahepatic hemorrhage, extensive infiltration of lymphocytes into liver tissue and serious destruction of liver structure (Figure 4b). Interestingly, AE strongly prevented the development of severe hepatic lesions induced by EF, indicated by decreased intrahepatic hemorrhage and infiltration of lymphocytes, and little destruction of liver structure (Figure 4c). In addition, there was not much difference between control and AE-treated groups (Figure 4d).

3.4. AE prevented EF-induced liver apoptosis

Bcl-2, a membrane protein, can prevent the release of pro-apoptotic factors from the mitochondrial outer membrane and thus suppress apoptosis (20). As shown in Figures 5A and 5B, EF treatment (350 mg/kg) resulted in a marked decrease in the level of Bcl-2, whereas AE pretreatment reversed such a decrease.

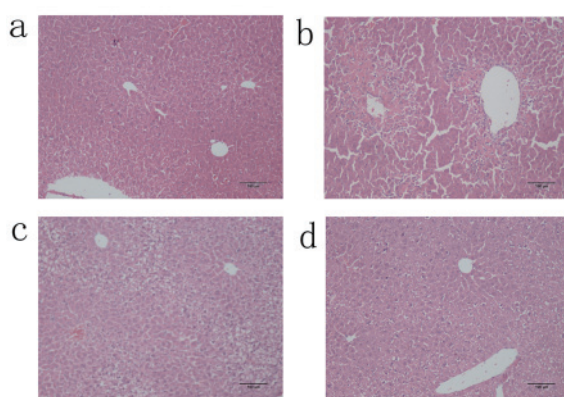


Figure 4. Liver histological evaluation of EF-treated mice with or without preadministration of AE. Liver sections were stained with hematoxylin-eosin. (a) Control group, (b) EF only group, (c) EF + AE (720 mg/kg) group, (d) AE (720 mg/kg) group. Magnification, $\times 100$.

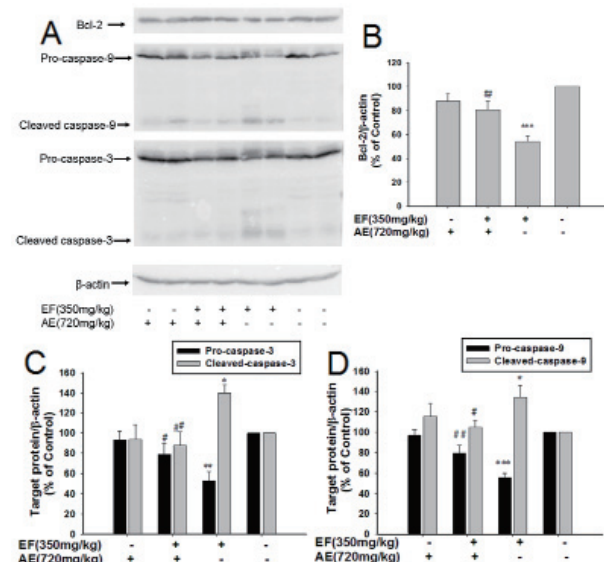


Figure 5. The expression of Bcl-2, and the activation of caspase-9 and caspase-3 in livers of EF-treated mice with or without preadministration of AE. (A) Protein extracts from liver tissue were analyzed by SDS-PAGE and immunoblotted using Bcl-2, caspase-9, caspase-3 and β -actin antibodies, respectively. The result represents one of three separate experiments, and the level of β -actin was used as loading control. The bands of Bcl-2 (B), Pro- and Cleaved caspase-3 (C) and Pro- and Cleaved caspase-9 (D) were normalized to basal β -actin expression and the vehicle control is set as 100%. Data are shown as means \pm S.E., and the results represent three separate experiments. * $p < 0.05$, ** $p < 0.01$, *** $p < 0.001$ versus control, # $p < 0.05$, ## $p < 0.01$ versus EF-treated group.

Our results in Figures 5A, 5C, and 5D indicated that the expression of pro-caspase-9 and -3 were decreased due to EF administration, while the cleaved fragments of caspase-9 and -3 were increased significantly. In contrast, the decreased levels of pro-caspase-9 and -3 were increased and the elevated fragments of caspase-9 and -3 were markedly decreased in the livers of mice pretreated with AE.

3.5. AE reversed EF-changed expression of SOD, GPx, I κ B

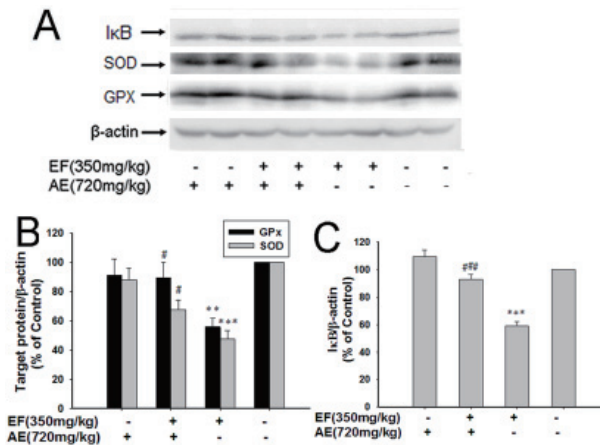


Figure 6. The expression of IκB, SOD, and GPx in livers of EF-treated mice with or without preadministration of AE. (A) Protein extracts from liver tissue were analyzed by SDS-PAGE and immunoblotted using IκB, SOD, GPx, and β-actin antibodies, respectively. The result represents one of three separate experiments, and the level of β-actin was used as loading control. The bands of SOD and GPx (B), IκB (C) were normalized to basal β-actin expression and the vehicle control is set as 100%. Data are shown as means ± S.E., and the results represent three separate experiments. ***p* < 0.01, ****p* < 0.001 versus control, #*p* < 0.05, ###*p* < 0.001 versus EF-treated group.

As shown in Figures 6A and 6C, EF decreased IκB expression as compared to control, while such a decrease was reversed in mice pretreated with AE. In addition, we also detected the expression of two antioxidant-related enzymes SOD and GPx. The results in Figures 6A and 6B showed that the decreased expression of SOD and GPx induced by EF was reversed by the pretreatment with AE.

4. Discussion

The elevation of ALT, AST, ALP, and TB is the diagnostic indicator for acute liver injury (21). As shown in Figure 3, AE can prevent EF-induced liver injury, as indicated by the decreased ALT, AST, and ALP activities and the TB amounts which are increased after EF treatment. Histological analysis further confirmed the protection of AE against EF-induced liver injury (Figure 4). There are some reports about the protection of *A. sinensis* and its main compound ferulic acid against liver injury (16-18). In addition, our previous study demonstrated that ferulic acid can prevent diosbulbin B-induced liver injury in tumor-bearing mice (22). The present results demonstrate that *A. sinensis* prevented liver injury induced by *D. bulbifera*, and ferulic acid may be the active compound in *A. sinensis*.

Apoptosis is the process of programmed cell death which occurs during animal development and tissue homeostasis, and plays an important role in a variety of physiological and pathological processes (23). There are two major pathways during the initiation of apoptosis: the extrinsic pathway and the intrinsic pathway. The

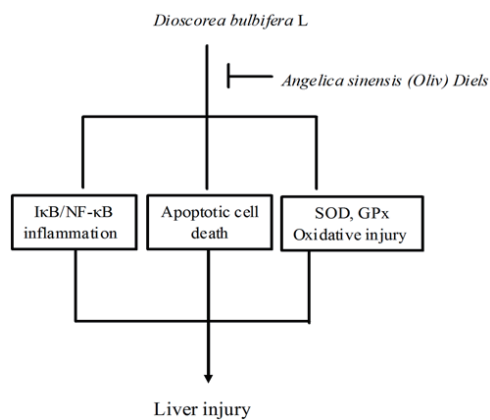


Figure 7. Schematic diagram of mechanism involved in EF-induced liver injury and AE's target(s) of protective action.

extrinsic pathway is related to death receptors, while the intrinsic pathway involves mitochondria: the release of pro-apoptotic factors from the mitochondrial outer membrane and subsequent activation of downstream caspase-9, finally resulting in activation of downstream executioner caspase-3 (24,25). Our results showed that EF down-regulated the expression of Bcl-2, pro-caspase-9, pro-caspase-3, while increased the expression of cleaved caspase-9 and caspase-3. In contrast, such phenomena were all reversed in the livers of mice pretreated with AE (Figure 5). All these results suggest that AE prevents EF-induced apoptotic liver injury.

Many studies have demonstrated that reactive oxygen species (ROS) play an important role in various hepatotoxin-induced liver injuries (26-28). The body has an effective defense mechanism to prevent and neutralize the free radical-induced damage. Hepatic cellular oxidative stress often takes place during the lack of antioxidants. SOD and GPx, two endogenous antioxidant enzymes, play important roles in the defense against ROS (29). SOD can efficiently and specifically catalyze dismutation of O²⁻ to O₂ and H₂O₂, while GPx catalyzes the further decomposition of H₂O₂ using reduced glutathione as a substrate (30,31). The results show that EF down-regulated the expression of SOD and GPx, while AE prevented such a decrease. The results suggest that *A. sinensis* can elevate antioxidant capacity to counteract with *D. bulbifera*-induced liver injury.

IκB is an inhibitory protein, and it inhibits the transcription of nuclear factor κB (NF-κB), which plays a pivotal role in inflammatory and immune responses (32-34). There are already reports that immune dysfunction is involved in alcohol and various drug-induced liver injuries, of which IκB/NF-κB plays an important role (35,36). As shown in Figure 6C, AE can reverse EF-induced decrease of IκB expression. The decrease of IκB protein will lead to the activation of NF-κB, and our result indicates that the IκB/NF-κB signal pathway may also be involved in the protection

of *A. sinensis* against the hepatotoxicity induced by *D. bulbifera*.

In the present study we found that *A. sinensis* prevented the hepatotoxicity induced by *D. bulbifera* via inhibiting apoptosis, meanwhile two important antioxidant enzymes SOD and GPx, and IκB may be involved in such protection (Figure 7).

Acknowledgements

This work was financially supported by State major science and technology special projects during the 12th five year plan (2015ZX09501004-002-002) and the Program for New Century Excellent Talents in University (NCET-11-1054).

References

- Gao H, Kuroyanagi M, Wu L, Kawahara N, Yasuno T, Nakamura Y. Antitumor-promoting constituents from *Dioscorea bulbifera* L. in JB6 mouse epidermal cells. *Biol Pharm Bull.* 2002; 25:1241-1243.
- Murray RDH, Jorge Z, Khan NH, Shahjahan M, Quaisuddin M. Diosbulbin D and 8-epidiosbulbin E acetate, norclerodane diterpenoids from *Dioscorea bulbifera* tubers. *Phytochemistry.* 1984; 23:623-625.
- Liu JR. Two cases of toxic hepatitis caused by *Dioscorea bulbifera* L. *Adverse Drug Reactions J.* 2002; 2:129-130. (In Chinese)
- Wang JM, Ji LL, Liu H, Wang ZT. Study of the hepatotoxicity induced by *Dioscorea bulbifera* L. rhizome in mice. *Biosci Trends.* 2010; 4:79-85.
- Sheng YC, Ma YB, Deng ZP, Wang ZT. Cytokines as potential biomarkers of liver toxicity induced by *Dioscorea bulbifera* L. *Biosci Trends.* 2014; 8:32-37.
- Ma YB, Niu CW, Wang JM, Ji LL, Wang ZT. Diosbulbin B-induced liver injury in mice and its mechanism. *Hum Exp Toxicol.* 2013; 33:729-736.
- Ma M, Jiang Z, Ruan J, Tan X, Liu J, Wang C, Zha XM, Zhang L. The furano norclerodane diterpenoid disobulbin-D induces apoptosis in normal human liver L-02 cells. *Exp Toxicol Pathol.* 2012; 64:611-618.
- Liu H, Chou GX, Guo YL, Ji LL, Wang JM, Wang ZT. Norclerodane diterpenoids from the rhizomes of *Dioscorea bulbifera*. *Phytochemistry.* 2010; 71:1174-1180.
- Kawasaki T, Komori T, Setoguchi S. Furanoid norditerpenes from Dioscoreaceae plants. I. Diosbulbins A, B and C from *Dioscorea bulbifera* L. forma spontanea. *Chem Pharm Bull.* 1968; 16:2430-2435.
- Wang G, Liu JS, Lin BB, Wang GK, Liu JK. Two new furanoid norditerpenes from *Dioscorea bulbifera*. *Chem Pharm Bull.* 2009; 57:625-627.
- Shimizu M, Matsuzawa T, Suzuki S, Yoshizaki M, Morita N. Evaluation of angelicae radix (Touki) by the inhibitory effect on platelet aggregation. *Chem Pharm Bull.* 1991; 39:2046-2048.
- Liu J, Burdette JE, Xu H, Gu C, van Breemen RB, Bhat KP, Booth N, Constantinou AI, Pezzuto JM, Fong HH, Farnsworth NR, Bolton JL. Evaluation of estrogenic activity of plant extracts for the potential treatment of menopausal symptoms. *J Agric Food Chem.* 2001; 49:2472-2479.
- Tsai NM, Lin SZ, Lee CC, Chen SP, Su HC, Chang WL, Harn HJ. The antitumor effects of *Angelica sinensis* on malignant brain tumors *in vitro* and *in vivo*. *Clin Cancer Res.* 2005; 11:3475-3484.
- Xin YF, Zhou GL, Shen M, Chen YX, Liu SP, Chen GC, Chen H, You ZQ, Xuan YX. Angelica sinensis: A novel adjunct to prevent doxorubicin-induced chronic cardiotoxicity. *Basic Clin Pharmacol.* 2007; 101:421-426.
- Zhang Z, Zhao R, Qi J, Wen S, Tang Y, Wang D. Inhibition of glycogen synthase kinase-3β by *Angelica sinensis* extract decreases β-amyloid-induced neurotoxicity and tau phosphorylation in cultured cortical neurons. *J Neurosci Res.* 2011; 89:437-447.
- Ye YN, Liu ES, Li Y, So HL, Cho CC, Sheng HP, Lee SS, Cho CH. Protective effect of polysaccharides-enriched fraction from *Angelica sinensis* on hepatic injury. *Life Sci.* 2001; 69:637-646.
- Srinivasan M, Rukkumani R, Ram Sudheer A, Menon VP. Ferulic acid, a natural protector against carbon tetrachloride-induced toxicity. *Fund Clin Pharmacol.* 2005; 19:491-496.
- Thyagaraju BM, Muralidhara. Ferulic acid supplements abrogate oxidative impairments in liver and testis in the streptozotocin-diabetic rat. *Zool Sci.* 2008; 25:854-860.
- Wang JM, Liang QN, Ji LL, Liu H, Wang CH, Wang ZT. Gender-related difference in liver injury induced by *Dioscorea bulbifera* L. rhizome in mice. *Hum Exp Toxicol.* 2011; 30:1333-1341.
- Cory S, Huang DC, Adams JM. The Bcl-2 family: Roles in cell survival and oncogenesis. *Oncogene.* 2003; 22:8590-8607.
- Rajesh MG, Latha MS. Preliminary evaluation of the antihepatotoxic activity of Kamilari, a polyherbal formulation. *J Ethnopharmacol.* 2004; 91:99-104.
- Wang JM, Sheng YC, Ji LL, Wang ZT. Ferulic acid prevents liver injury and increases the anti-tumor effect of diosbulbin B *in vivo*. *J Zhejiang Univ Sci B.* 2014; 15:540-547.
- Jacobson MD, Weil M, Raff MC. Programmed cell death in animal development. *Cell.* 1997; 88:347-354.
- Jin Z, El-Deiry WS. Overview of cell death signaling pathways. *Cancer Biol Ther.* 2005; 4:139-163.
- Bao Q, Shi Y. Apoptosome: a platform for the activation of initiator caspases. *Cell Death Differ.* 2007; 14:56-65.
- Chen YH, Lin FY, Liu PL, Huang YT, Chiu JH, Chang YC, Man KM, Hong CY, Ho YY, Lai MT. Antioxidative and hepatoprotective effects of magnolol on acetaminophen-induced liver damage in rats. *Arch Pharm Res.* 2009; 32:221-228.
- dos Santos NA, Martins NM, Curti C, Pires Bianchi Mde L, dos Santos AC. Dimethylthiourea protects against mitochondrial oxidative damage induced by cisplatin in liver of rats. *Chem-Biol Interact.* 2007; 170:177-186.
- Liang QN, Liu TY, Ji LL, Min Y, Xia YY. Pyrrolizidine alkaloid clivorine-induced oxidative stress injury in human normal liver L-02 cells. *Drug Discov Ther.* 2009; 3:247-251.
- Liu CM, Zheng YL, Lu J, Zhang ZF, Fan SH, Wu DM, Ma JQ. Quercetin protects rat liver against lead-induced oxidative stress and apoptosis. *Environ Toxicol Pharmacol.* 2010; 29:158-166.
- Halliwell B, Cutteridge JMC. Oxygen radicals and the nervous system. *Trends Neurosci.* 1985; 8:22-26.
- Cotgreave IA, Moldeus P, Brattsand R, Hallberg A,

- Andersson CM, Engman L. Alpha-(phenylselenenyl)-aceto-phenone derivates with glutathione peroxidase-like activity. *Biochem Pharmacol.* 1992; 43:793-802.
32. Baeuerle PA, Henkel T. Function and activation of NF-kappa B in the immune system. *Annu Rev Immunol.* 1994; 12:141-179.
33. Baeuerle PA, Baltimore D. NF-kappa B: ten years after. *Cell.* 1996; 87:13-20.
34. Thompson JE, Phillips RJ, Erdjument-Bromage H, Tempst P, Ghosh S. I kappa B-beta regulates the persistent response in a biphasic activation of NF-kappa B. *Cell.* 1995; 80:573-582.
35. Antoniades CG, Berry PA, Wendon JA, Vergani D. The importance of immune dysfunction in determining outcome in acute liver failure. *J Hepatol.* 2008; 49:845-861.
36. Mandrekar P, Szabo G. Signaling pathways in alcohol-induced liver inflammation. *J Hepatol.* 2009; 50:1258-1266.

(Received July 8, 2014 ; Revised September 25, 2014;
Re-revised October 9, 2014 ; Accepted October 10, 2014)

Fabrication and bioactivity evaluation of porous anodised TiO₂ films *in vitro*

Fei Teng^{1,*}, Juanjuan Li^{1,2,*}, Yanyun Wu¹, Haohua Chen¹, Qi Zhang¹, Hu Wang¹, Guomin Ou^{1,**}

¹ West China School of Stomatology, Sichuan University, Chengdu, Sichuan, China;

² Center of Dental Implantation, the Third Affiliated Hospital of Xinxiang Medical University, Henan, China.

Summary

This study aims to find an optimal method for modifying the neck of dental implants for gingival attachment through *in vitro* investigations of the biological features of various anodised TiO₂ films. The titanium sheets were divided into four groups: a control group and three test groups classified according to the anodisation voltage (Group 150 V, Group 180 V or Group 200 V). The surface microstructure and crystal structure were observed using scanning electron microscopy and X-ray diffraction. The protein adsorption ability, antibacterial activity and cell adhesion ability were tested to examine the biological properties of the materials *in vitro*. Microscopic grooves were observed in the control group, whereas the test groups contained numerous pores. Group 180 V and Group 200 V showed higher protein adsorption ability ($p < 0.05$), whereas Group 150 V and Group 180 V exhibited better antibacterial activity ($p < 0.05$). Higher cell concentrations of L929 were observed in Group 180V and Group 200 V than in the other two groups ($p < 0.05$), which indicated that the TiO₂ films formed at 180 V promote protein adsorption and enhance fibroblast growth while inhibiting bacterial adhesion. These results indicate that anodisation positively affects the formation of a biological seal in the neck region of dental implants.

Keywords: Anodic oxidation, TiO₂ film, biomaterials, surfaces, *in vitro* bioactivity

1. Introduction

Titanium and its alloys are used for dental implants because of their low toxicity, low corrosion rate, favourable mechanical properties and excellent biocompatibility (1). However, bone loss often occurs in the alveolar crest surrounding the dental implants, and a stable biochemical connection between the neck part of the implant and gingival tissue is difficult to achieve. These findings can be attributed to the lack of natural biological width and functionally oriented fibre (2-4).

The formation of a firm soft tissue barrier around

the dental implant neck is considered important to prevent bacterial invasion (5). To control plaque formation around the neck, most current designs for this region are mechanically machined to achieve a smooth surface, which facilitates the proliferation of epithelial cells. However, unlike the orientation perpendicular to the natural teeth surface, the orientation of the collagen fibres in the connective tissue was found to be parallel to the implant surface (6,7), which may cause epithelial down growth after the implants have been inserted (8).

To resolve these issues, an on-going goal in bioengineering is to modify titanium implant surfaces and establish the bionic attachment of peri-implant soft tissues in the neck region. A coating for the neck that can help reduce plaque accumulation and form a good seal would be desirable (9,10). Several studies have revealed that the micro-roughening of surfaces not only inhibits the formation of plaque but also facilitates the growth of epithelial cells and fibroblasts (11). The anchor-shaped structure formed by cellular processes and that extends into the pores on the material

*These authors contributed equally to this work.

**Address correspondence to:

Dr. Guomin Ou, Department of Implantology, West China School of Stomatology, Sichuan University. NO.14, 3rd Section of Ren Min Nan Rd. Chengdu, Sichuan 610041, China.

E-mail: guominou66@yahoo.com

effectively inhibits the migration of the junctional epithelium to the root square (12,13).

To obtain this type of micro-roughened surface, several techniques, such as anodic oxidation, plasma spraying, ion planting, sol-gel, sputtering and chemical vapour deposition (14,15), have been used to produce oxide films on titanium and its alloys. Among these methods, anodic oxidation treatment, which can be readily applied to implants with irregular and complex surface geometries (16), has become more attractive in recent years. Moreover, a porous TiO_2 layer can be obtained at low temperatures, and the morphology and crystallinity of the oxides can be well controlled by changing the voltage, current density and electrolyte (17-19).

In this study, anodic oxidation was adopted to form a porous film with different pore sizes on titanium surfaces. The aim of this study was to create a desirable interface that not only enhances the connection between the host and implant but also inhibits microbial adhesion.

2. Materials and Methods

2.1. Sample preparation

Commercially pure titanium of ASTM grade 2 (99.9% Ti, Northwest Institute for Nonferrous Metal Research, Shanghai, China) was cut into 10-mm diameter sheets with a thickness of 1 mm. The sheets were carefully ground with Nos. 400, 600, 800, 1000, and 1200 SiC paper and were subsequently cleaned ultrasonically with pure acetone, ethanol and distilled water for 5 min.

The titanium sheets were divided into four groups: a control group, which consisted of the sheets processed using only the previously described steps, and three test groups classified according to the anodising voltage (Group 150 V, Group 180 V or Group 200 V). Anodic oxidation was performed at room temperature with a direct-current supply system (QUERLI DC power supply WYJ-500 V 1 A, China). A titanium sheet was used as the anode, and a titanium plate (20 mm × 20 mm × 1 mm) served as the cathode. A sodium acetate solution (1 mol/L) was used as the electrolyte, and three final voltages (150 V, 180 V and 200 V) were adopted to form a porous film on the titanium surface. The current density was 50 mA/cm², and the time at the final voltage was 2 min.

2.2. Surface characterisation

The surface microstructure, elemental composition and crystal structure of the titanium oxide films were observed using scanning electron microscopy (SEM, Hitachi, S-4800, Tokyo, Japan), energy dispersive X-ray spectroscopy (EDS, Hitachi, S-4800, Tokyo, Japan) and X-ray diffraction (XRD, X'Pert, PANalytical B.V., Almelo, Netherlands).

2.3. Protein adsorption ability

A bicinchoninic acid (BCA) protein assay (20) was adopted to measure the concentration of the proteins. Samples were placed in a 16-well cell culture plate. Approximately 1 mL of standard bovine serum albumin (BSA, 2 mg/mL) was added into each well, and the plate was placed on a thermostatic horizontal shaker for 2 h (50 rpm, 20°C). According to the Lambert-Beer law, the absorbance of a solution can be evaluated by its concentration at a given wavelength of light (21). Therefore, the optical density (OD) of the supernatant was measured at 562 nm using a spectrophotometer (TECAN SpectrofluorPlus); the concentration of the corresponding BSA solution was subsequently calculated, and the protein adsorption quantity of different surfaces was obtained.

2.4. Antibacterial activity

A modified antibacterial drop-test (22) was used to study the antibacterial activity of the samples. As the predominant bacterial flora in healthy peri-implant sulci, *Streptococcus mutans* (23) (*S. mutans*, ATCC 25175, provided by the State Key Laboratory of Oral Diseases, West China Hospital of Stomatology, Sichuan University) were chose and cultivated in brain-heart infusion (BHI) broth and anaerobically cultured (37°C, 80% N₂, 10% CO₂, 10% H₂) for 24 h. The bacteria-containing broth was centrifuged at 2,700 rpm for 10 min. The supernatant was discarded, and the bacteria were washed three times with phosphate-buffered saline (PBS). The bacteria were then resuspended in PBS at a concentration of 1×10^6 cfu/mL. All glassware and disk samples were sterilised with ultraviolet irradiation for 1 h beforehand. The bacterial suspension (1 mL) was added dropwise using a dispenser onto the surface of each sample in a 16-well plate, followed by incubation at 37°C for 24 h without stirring. After this period, the samples were washed three times with PBS and then resuspended in 4 mL PBS using ultrasonic vibration for 5 min at room temperature. The bacterial suspension was diluted 10,000-fold, and a 30-μL bacterial suspension of each sample was dropped onto the BHI solid medium to obtain a colony count after 48 h of incubation.

2.5. L929 fibroblast adhesion

L929 mouse fibroblasts (provided by the State Key Laboratory of Oral Diseases, West China Hospital of Stomatology, Sichuan University) were cultivated in Dulbecco's Modified Eagle Medium (DMEM) containing 10% foetal bovine serum (FBS) and 1% penicillin/streptomycin. An L929 fibroblast monolayer was formed, which was passaged upon confluence using trypsin (0.5% w/v in PBS). The cells were subsequently harvested from the culture by immersion in

trypsin solution for 5 min. The cells were centrifuged, and the supernatant was discarded. DMEM (3 mL) supplemented with serum was added to neutralise any residual trypsin, and then the cells were resuspended in serum-supplemented DMEM at a concentration of 1×10^4 /mL. Afterward, the cells were cultivated in 5% CO₂ at 37°C.

The L929 cells were seeded onto different disk surfaces, and after a 24 h incubation, the sample surfaces were washed with PBS solution to remove loosely adsorbed cells. Cell fixation was performed with 4% glutaraldehyde in PBS for 4 h at 4°C, followed by dehydration with 25%, 50%, 70% and 95% (v/v) ethanol solutions for 15 min and final dehydration in absolute ethanol twice. The surfaces with immobilised cells were dried in supercritical carbon dioxide and were subsequently observed by SEM.

2.6. Statistical analysis

Statistical calculations were performed using the SPSS 17.0 software package. The differences were considered significant if the probability value was less than 5% ($p < 0.05$). SKEW and KURT tests were initially used to test the data for normality. A Levene test was conducted to examine the homogeneity of variance for multiple samples. Normally distributed data were expressed as the mean and standard deviation. For three-group comparisons, one-way ANOVA and Dunnett's *t*-test were used.

3. Results and Discussion

3.1. Surface characterisation

Figure 1 illustrates the surface SEM micrographs of the control samples and the samples anodised in 1M CH₃COONa for 2 min at different voltages. The surface of the control group showed scratches and grooves formed during mechanical grounding (Figure 1A).

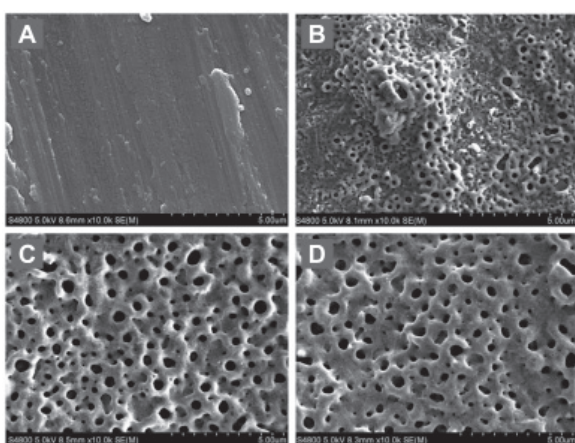


Figure 1. SEM images. (A) The control group, (B) Group 150 V, (C) Group 180 V and (D) Group 200 V.

The surface processed by anodic oxidation at 150 V (Figure 1B) no longer showed visible scratches, and the surface consisted of randomly scattered pits and holes; diameters were approximately 100 nm to 3 μm. The surface subjected to an applied voltage of 180 V (Figure 1C) became uniform and was overlaid with densely distributed pores with sizes that ranged from 2 μm to 7 μm. The size of the pores did not change when the applied voltage was increased to 200 V (Figure 1D). Several larger-sized pores appeared, most likely because of the interconnection of some pores with each other (24). EDS analysis showed no contamination on any of the groups of disks (Figure 2).

Figure 3 shows the XRD patterns of the control group and the test groups. For the control group, only the peaks of titanium were observed. The XRD pattern of the surface treated with an applied voltage of 150 V indicated the presence of anatase phase, and the intensity of the anatase phase continued to increase until 180 V. The peaks of the rutile phase appeared in the pattern of the sample treated at 180 V, and the intensity of the corresponding peaks continued to increase as the anodisation voltage was increased from 180 V to 200 V, whereas the intensity of the peaks from the anatase phase and the titanium substrate decreased.

Starting with the growth of the amorphous TiO₂ (25), the formation of the anodic titanium oxides is

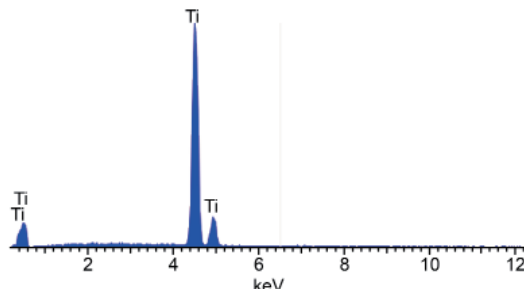


Figure 2. EDS graph of the anodic oxidation group.

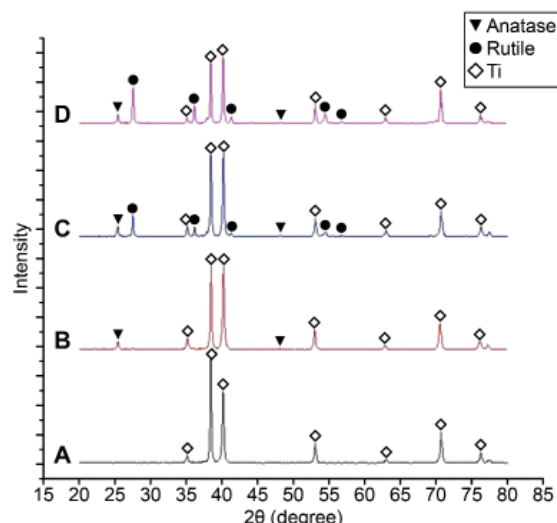


Figure 3. XRD graph. (A) The control group, (B) Group 150 V, (C) Group 180 V and (D) Group 200 V.

a process of competition between the deposition of the titanium oxides layer and the dissolution of that layer by the electrolyte (26). As the applied voltage is increased, the anodic oxidised film breaks down locally and porous regions become obvious because of the dielectric breakdown (27). According to our previous study (25), when the substrates were anodised in CH₃COONa electrolyte, spark discharges were observed on their surfaces beginning at ~135V; these discharges became more intense at higher anodising voltages. This behaviour accounts for the porous surface at 150 V observed by SEM. Meanwhile, spark discharges led to instantaneous, local high temperatures and pressures (28), so the initially produced amorphous titania was converted into the crystalline phases (29). The anatase structure was formed at the beginning and then transformed into the rutile phase with increasing voltage, which was consistent with the XRD results.

Among the three phases of titanium dioxide, rutile is known to be the most dense and stable phase and to exhibit the highest resistance to dissolution (26). As shown by the SEM results, the pore size and the porosity increased when the applied voltage was varied from 150 V to 180 V due to the growing field-assisted and chemical dissolution (16). However, as additional rutile formed during the crystallographic transformation, the dissolution resistance continued to increase, which led to similar pore sizes and porosities of the samples treated at 180 V and 200 V.

3.2. Protein adsorption ability

Figure 4 shows that the control sample exhibited presented the poorest adsorbing ability for proteins and that the protein adsorption ability increased as the applied voltage was increased from 150 V to 180 V. As the applied voltages increase, the thickness, surface roughness and porosity of the anodised TiO₂ layer increase (27), which, in turn, increase the biocompatibility and improve the protein adsorption ability (26). In addition, compared with rutile and amorphous titanium, anatase exhibits better bioactivity (30,31). Therefore, due to the decrease in the amount of anatase on the surface anodised at 200 V, the protein

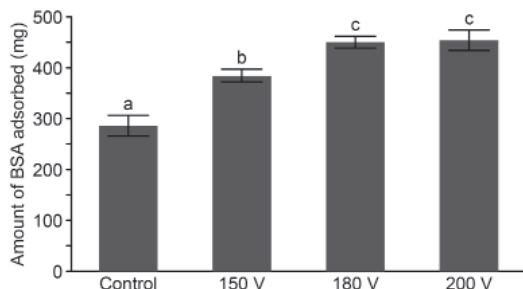


Figure 4. Amount of bovine serum albumin (BSA) adsorbed onto different surfaces. (a, b, c) Different letters indicate a significant difference at $p < 0.05$.

adsorption ability did not obviously change between Group 180 V and Group 200 V.

3.3. Antibacterial activity

The *S. mutans* colonies found on the culture were counted, and no significant difference in bacterial adherence was observed between the control group and Group 200 V or between Group 150 V and Group 180 V. The quantities of bacterial colonies observed in the control group and Group 200 V were much greater than those observed in Group 150 V and Group 180 V (Figure 5).

In the case of an applied voltage of 150 V, the increased antibacterial activity was attributed to the increase in the high photocatalytic crystalline phase of anatase (22,32). Although the amount of anatase structure continued to increase in samples treated up to 180 V, the appearance of the rutile phase, which decreases the photocatalytic activity of the TiO₂ film (22), made the antibacterial activity of the sample treated at 180 V almost the same as that treated at 150 V. In the case of the sample treated at an applied voltage of 200 V, in which the amounts of rutile and anatase increased and decreased, respectively, the antibacterial activity decreased sharply.

3.4. L929 growth

L929 fibroblasts were seeded onto the sample surface. After 24 h (26), some of the L929 fibroblasts started to develop pseudopods, and some fibroblasts spread out on the TiO₂ films, appearing in fusiform, polygonal and triangular shapes (Figure 6). As shown in the inset of Figure 6C, a single cell could be clearly observed to spread out its body and interlock to the porous surface with filopodia, whereas the cellular form and linkage were obscure in the control group. Furthermore, the cell concentration on the uncoated titanium surface was obviously lower than on the other surfaces, and the cell concentrations on the titanium surfaces anodised at 180 V and 200 V stood out, which can be attributed to the enhanced biological performance of the anodised TiO₂ surfaces (33).

It's widely accepted that application of the porous

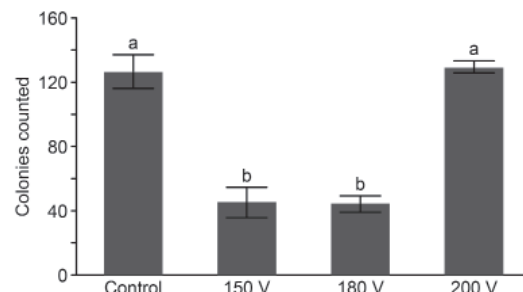


Figure 5. Number of *Streptococcus mutans* colonies that adhered to the different surfaces. (a, b) Different letters indicate a significant difference at $p < 0.05$.

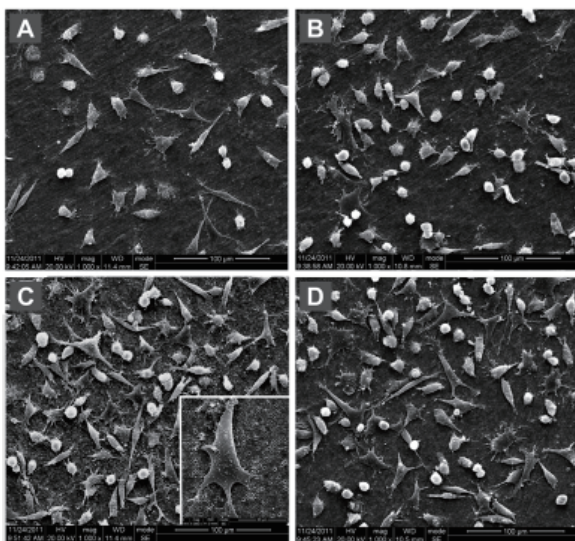


Figure 6. SEM images of L929 cells cultured for 24 h on different surfaces. (A) The control group, **(B)** Group 150 V, **(C)** Group 180 V and **(D)** Group 200 V. The cell concentrations on the titanium surfaces anodised at 180V (C) and 200V (D) stood out, which indicates better cell adhesion and proliferation. The inset shows a higher-magnification image in which a single cell could be clearly observed to spread out its body and interlock to the porous surface with filopodia.

surface can greatly improve the outcome of cell seeding (34), just in accordance with the significant higher cell concentration on the titanium surfaces of the test groups. Squier *et al.* (8), on the basis of an *in vitro* study, suggested that 3 µm is the minimum pore size that permits penetration of the connective tissue, thus, the collagen fibres are oriented perpendicularly to the implant surface and epithelial downgrowth is markedly restricted when the pore sizes are larger than 3 µm. Therefore, we determined that a greater cell concentration results in a fully spread-out morphology and that the obvious anchorage on the titanium surfaces anodised at 180 V or 200 V may be the result of the adequate pore sizes formed at these voltages. In addition, as the protein adsorption ability of the materials acts as the base to support cell adhesion and proliferation (26), the bacterial adhesion performances were consistent with the protein adsorption results.

4. Conclusion

The porous TiO₂ films formed through anodisation at 180 V promote the adsorption of proteins, inhibit bacterial adhesion and enhance fibroblast growth, which indicates that anodisation positively affects biological seal formation in the neck region.

Acknowledgements

This work was supported by the National Natural Science Foundation of China (Project No. 81070868/H1409). We acknowledge the staff and faculty at

the State Key Laboratory of Oral Diseases, Sichuan University for their assistance.

References

- Buser D, Belser UC, Lang NP. The original one-stage dental implant system and its clinical application. *Periodontol*. 2000; 1998; 17:106-118.
- Sul YT, Jeong Y, Johansson C, Albrektsson T. Oxidized, bioactive implants are rapidly and strongly integrated in bone. Part 1--experimental implants. *Clin Oral Implants Res*. 2006; 17:521-526.
- Holt RL, Rosenberg MM, Zinser PJ, Ganeles J. A concept for a biologically derived, parabolic implant design. *Int J Periodontics Restorative Dent*. 2002; 22:473-481.
- Schupbach P and Glauser R. The defense architecture of the human periimplant mucosa: A histological study. *J Prosthet Dent*. 2007; 97:S15-25.
- Glauser R, Schupbach P, Gottlow J, Hammerle CH. Periimplant soft tissue barrier at experimental one-piece mini-implants with different surface topography in humans: A light-microscopic overview and histometric analysis. *Clin Implant Dent Relat Res*. 2005; 7(Suppl 1):S44-51.
- Comut AA, Weber HP, Shortkroff S, Cui FZ, Spector M. Connective tissue orientation around dental implants in a canine model. *Clin Oral Implants Res*. 2001; 12:433-440.
- Tete S, Mastrangelo F, Bianchi A, Zizzari V, Scarano A. Collagen fiber orientation around machined titanium and zirconia dental implant necks: An animal study. *Int J Oral Maxillofac Implants*. 2009; 24:52-58.
- Squier CA and Collins P. The relationship between soft tissue attachment, epithelial downgrowth and surface porosity. *J Periodontal Res*. 1981; 16:434-440.
- Oh TJ, Yoon J, Misch CE, Wang HL. The causes of early implant bone loss: Myth or science? *J Periodontol*. 2002; 73:322-333.
- Rutar A, Lang NP, Buser D, Burgin W, Mombelli A. Retrospective assessment of clinical and microbiological factors affecting periimplant tissue conditions. *Clin Oral Implants Res*. 2001; 12:189-195.
- Bratu EA, Tandlich M and Shapira L. A rough surface implant neck with microthreads reduces the amount of marginal bone loss: A prospective clinical study. *Clin Oral Implants Res*. 2009; 20:827-832.
- Simion M, Baldoni M and Rossi P. A study on the attachment of human gingival cell structures to oral implant materials. *Int J Prosthodont*. 1991; 4:543-547.
- Mustafa K, Oden A, Wennerberg A, Hultenby K, Arvidson K. The influence of surface topography of ceramic abutments on the attachment and proliferation of human oral fibroblasts. *Biomaterials*. 2005; 26:373-381.
- Ishizawa H and Ogino M. Characterization of thin hydroxyapatite layers formed on anodic titanium oxide films containing Ca and P by hydrothermal treatment. *J Biomed Mater Res*. 1995; 29:1071-1079.
- Kim HM, Miyaji F, Kokubo T, Nishiguchi S, Nakamura T. Graded surface structure of bioactive titanium prepared by chemical treatment. *J Biomed Mater Res*. 1999; 45:100-107.
- Park IS, Lee MH, Bae TS, Seol KW. Effects of anodic oxidation parameters on a modified titanium surface. *J*

- Biomed Mater Res B Appl Biomater. 2008; 84:422-429.
- 17. Zhu X, Kim KH, Jeong Y. Anodic oxide films containing Ca and P of titanium biomaterial. *Biomaterials*. 2001; 22:2199-2206.
 - 18. Ishizawa H, Ogino M. Formation and characterization of anodic titanium oxide films containing Ca and P. *J Biomed Mater Res*. 1995; 29:65-72.
 - 19. Sul YT, Johansson CB, Jeong Y, Albrektsson T. The electrochemical oxide growth behaviour on titanium in acid and alkaline electrolytes. *Med Eng Phys*. 2001; 23:329-346.
 - 20. Smith PK, Krohn RI, Hermanson GT, Mallia AK, Gartner FH, Provenzano MD, Fujimoto EK, Goeke NM, Olson BJ, Klenk DC. Measurement of protein using bicinchoninic acid. *Anal Biochem*. 1985; 150:76-85.
 - 21. Gao L, Feng B, Wang J, Lu X, Liu D, Qu S, Weng J. Micro/nanostructural porous surface on titanium and bioactivity. *J Biomed Mater Res B Appl Biomater*. 2009; 89:335-341.
 - 22. Trapalis CC, Keivanidis P, Kordas G, Zaharescu M, Crisan M, Szatvanyi A, Gartner M. TiO₂(Fe³⁺) nanostructured thin films with antibacterial properties. *Thin Solid Films*. 2003; 433:186-190.
 - 23. Kocar M, Seme K, Hren NI. Characterization of the normal bacterial flora in peri-implant sulci of partially and completely edentulous patients. *Int J Oral Maxillofac Implants* 2010; 25:690-8.
 - 24. Sul YT, Johansson CB, Petronis S, Krozer A, Jeong Y, Wennerberg A, Albrektsson T. Characteristics of the surface oxides on turned and electrochemically oxidized pure titanium implants up to dielectric breakdown: The oxide thickness, micropore configurations, surface roughness, crystal structure and chemical composition. *Biomaterials*. 2002; 23:491-501.
 - 25. Xie L, Liao XM, Xu H, Yin GF, Huang ZB, Yao YD, Chen XC, Gu JW. A facile one-step anodization treatment to prepare multi-level porous titania layer on titanium. *Mater Lett*. 2012; 72:141-144.
 - 26. Xie L, Yin G, Yan D, Liao X, Huang Z, Yao Y, Kang Y, Liu Y. Structure, morphology and fibroblasts adhesion of surface-porous titanium via anodic oxidation. *J Mater Sci Mater Med*. 2010; 21:259-266.
 - 27. Kuromoto NK, Simao RA, Soares GA. Titanium oxide films produced on commercially pure titanium by anodic oxidation with different voltages. *Mater Charact*. 2007; 58:114-121.
 - 28. Wu HH, Lu XY, Long BH, Wang XQ, Wang JB, Jin ZS. The effects of cathodic and anodic voltages on the characteristics of porous nanocrystalline titania coatings fabricated by microarc oxidation. *Mater Lett*. 2005; 59:370-375.
 - 29. Li LH, Kong YM, Kim HW, Kim YW, Kim HE, Heo SJ, Koak JY. Improved biological performance of Ti implants due to surface modification by micro-arc oxidation. *Biomaterials*. 2004; 25:2867-2875.
 - 30. Yang TS, Shiu CB, Wong MS. Structure and hydrophilicity of titanium oxide films prepared by electron beam evaporation. *Surf Sci*. 2004; 548:75-82.
 - 31. Sun LC, Hou P. Spectroscopic ellipsometry study on e-beam deposited titanium dioxide films. *Thin Solid Films*. 2004; 455:525-529.
 - 32. Zhang HJ, Wen DZ. Antibacterial properties of Sb-TiO₂ thin films by RF magnetron co-sputtering. *Surf Coat Technol*. 2007; 201:5720-5723.
 - 33. Sul YT, Johansson CB, Jeong Y, Roser K, Wennerberg A, Albrektsson T. Oxidized implants and their influence on the bone response. *J Mater SciMater Med*. 2001; 12:1025-1031.
 - 34. Dai W, Dong J, Chen G, Uemura T. Application of low-pressure cell seeding system in tissue engineering. *Biosci Trends*. 2009; 3:216-219.

(Received March 2, 2014; Revised August 10, 2014; Revised October 9, 2014; Accepted October 10, 2014)

Clinical utility of simultaneous measurement of alpha-fetoprotein and des- γ -carboxy prothrombin for diagnosis of patients with hepatocellular carcinoma in China: A multi-center case-controlled study of 1,153 subjects

Peipei Song¹, Xiaobin Feng², Yoshinori Inagaki¹, Tianqiang Song³, Keming Zhang⁴, Zhigang Wang¹, Shuguo Zheng², Kuansheng Ma², Qiang Li³, Dalu Kong³, Qiang Wu³, Ti Zhang³, Xin Zhao⁴, Kiyoshi Hasegawa¹, Yasuhiko Sugawara¹, Norihiro Kokudo¹, Wei Tang^{1,*} and Japan-China Joint Team for Medical Research and Cooperation on HCC

¹ Hepato-Biliary-Pancreatic Surgery Division, Department of Surgery, Graduate School of Medicine, the University of Tokyo, Tokyo, Japan;

² Institute of Hepatobiliary Surgery, Southwest Hospital, Third Military Medical University, Chongqing, China;

³ Department of Hepatobiliary Tumor, Tianjin Medical University Cancer Hospital, Tianjin, China;

⁴ Hepatobiliary Surgery Department, 302 Military Hospital of China, Beijing, China.

Summary

This study aimed to investigate the clinical utility of simultaneous measurement of alpha-fetoprotein (AFP) and des- γ -carboxy prothrombin (DCP) for hepatocellular carcinoma (HCC) diagnosis in Chinese patients predominantly caused by hepatitis B virus infection by a multi-center case-controlled study. Subjects were 1,153 individuals from three major hospitals in China, including 550 cases in HCC group, 164 in Malignant disease group, 182 in Benign disease group, 85 in Chronic liver disease group, and 173 in Normal group. Serum levels of AFP and DCP were measured and clinicopathological features were determined for all subjects. Results showed that the levels of DCP and AFP were significantly higher in HCC group (550 patients, 74.18% with HBV infection) than that in other four groups ($P < 0.001$). Receiver operating curves (ROC) indicated the optimal cut-off value was 86 mAU/mL for DCP with a sensitivity of 71.50% and specificity of 86.30%, and 21 ng/mL for AFP with a sensitivity of 68.00% and specificity of 93.20%. The area under ROC curve was 0.846 for DCP, 0.832 for AFP, and 0.890 for the combination of DCP and AFP. The combination of DCP and AFP resulted in a higher Youden index and a sensitivity of approximately 90%, even for small tumors. The simultaneous measurement of AFP and DCP could achieve a better sensitivity in diagnosing Chinese HCC patients, even for small tumors.

Keywords: Serum biomarker, des- γ -carboxy prothrombin (DCP), alpha-fetoprotein (AFP), sensitivity, specificity

1. Introduction

Hepatocellular carcinoma (HCC) is the second leading cause of cancer deaths worldwide, with an estimated

global incidence of 782,000 new cases and nearly 746,000 deaths in 2012 (1). HCC is prevalent in Eastern and South-Eastern Asia, with an incidence of 31.9/100,000 and 22.2/100,000, where the major risk factor is hepatitis B virus (HBV) (2). Of particular note is the fact that China alone accounts for 50% of HCC cases worldwide, with a total prevalence of 26-32/10,000 and a prevalence as high as 70-80/10,000 in some areas (3,4).

While imaging diagnostic tools are widely used in Western countries, the serum biomarkers are still

*Address correspondence to:

Dr. Wei Tang, Hepato-Biliary-Pancreatic Surgery Division, Department of Surgery, Graduate School of Medicine, the University of Tokyo, Hongo 7-3-1, Bunkyo-ku, Tokyo, 113-8655, Japan.

E-mail: TANG-SUR@h.u-tokyo.ac.jp

regarded as useful tools for HCC early diagnosis in Asian countries. In China, alpha-fetoprotein (AFP) is the serum biomarker most widely used in HCC early diagnosis (5), and its clinical usefulness was confirmed by a randomized controlled trial of 18,816 Chinese patients in 2004 (6). However, AFP levels are normal in up to 40% of patients with HCC, particularly during the early stage of the disease (low sensitivity) (7,8), and elevated AFP levels are seen in patients with cirrhosis or exacerbation of chronic hepatitis (low specificity) (9,10). Furthermore, some studies have indicated that AFP has substantially limited diagnostic accuracy in detecting small HCC (11). Thus, other reliable serum biomarkers need to be identified to complement AFP in order to improve clinical outcomes for patients.

Worldwide, a number of studies have looked at des- γ -carboxy prothrombin (DCP), also known as prothrombin induced by vitamin K absence-II (PIVKA-II). Numerous studies have found that the combined testing of DCP and AFP has a sensitivity of 47.5-94.0% and a specificity of 53.3-98.5% in HCC early diagnosis, and these figures are higher than those for either marker alone (12-16). In Japan, DCP and AFP are widely and routinely used as serum biomarkers in HCC surveillance and diagnosis, which benefit the early diagnosis in more than 60% of patients (17). However, DCP is currently approved for use in Japan, South Korea, and Indonesia (18), yet has not been widely used in China. Furthermore, unlike in Japan and Western countries, the main etiological factor for HCC in China is chronic infection with HBV, which accounts for 85% of all cases. In order to assess the diagnostic value of DCP in Chinese patients with HCC, two studies published in 2002 (involving 60 patients with HCC and 30 patients with cirrhosis) (19) and 2003 (involving 120 patients with HCC and 90 patients with cirrhosis) (20) have indicated that the combined testing of DCP and AFP had a sensitivity of 78.3%, which is higher than that for DCP or AFP alone. However, the two studies were small in scale, the multiple-center studies of larger pools of serum samples from patients with HCC need to be conducted to provide further validation.

Given the rising incidence of HCC in China and the lack of substantial data on DCP's role as a serum biomarker in HCC diagnosis in Chinese patients, we conducted this large-scale, multi-center case-controlled study to further investigate the clinical utility of simultaneous measurement of AFP and DCP for HCC diagnosis in Chinese patients.

2. Materials and Methods

2.1. Study population

The subject pool consisted of 1,153 cases from the Hepato-Biliary-Pancreatic Surgery Division at the Southwest Hospital of the Third Military Medical

University, the Tianjin Medical University Cancer Hospital, and the 302 Military Hospital of China between 2001 and 2012. This study was approved by institutional review boards, and clinicopathological information on each subject was collected. Five groups of consecutive subjects were enrolled: 1) HCC group, which involved HCC patients proved by pathology after hepatic resection; 2) Malignant disease group, which involved patients with non-HCC malignant disease of the liver, bile ducts, or pancreas, including carcinoma of the gallbladder, cholangiocarcinoma, and pancreatic carcinoma; 3) Benign disease group, which involved patients with benign disease of the liver, bile ducts, or pancreas, including cholangiolithiasis, cholecystitis, hepatic cysts; 4) Chronic liver disease group, which involved patients with progressivity of hepatitis or liver cirrhosis; and 5) Normal group, which involved normal healthy subjects without risk factors for viral hepatitis. Among a total of 1,153 cases, 876 cases (75.98%) were male and 277 (24.02%) were female, with a median age of 46 years (range: 12-83 years). None of cases received vitamin K during the week prior to inclusion in this study.

2.2. Serological detection of DCP and AFP

Serum DCP levels were measured with an electro-chemiluminescence immunoassay using a highly sensitive DCP determination kit (ED036, Eisai, Tokyo, Japan) in accordance with the manufacturer's instructions. The range of detection was 10-200,000 mAU/mL. Serum AFP levels were tested using a commercial ELISA kit in accordance with instructions from the manufacturer (Biocell Biotech, Zhengzhou, China). For patients undergoing surgery, blood samples for measurement of DCP and AFP were obtained a week before surgery. Blood samples were spun, serum aliquoted, and stored at -80°C until testing. All testing was conducted at the Southwest Hospital of the Third Military Medical University by the same group of laboratory technicians, and none of technicians was informed of the subject's status prior to testing.

2.3. Data collection and analysis

Clinicopathological variables of age, gender, HBsAg, anti-HCV, levels of DCP and AFP, tumor size, and histological pathology were examined.

Continuous variables were expressed as median (range) and compared between groups using the Wilcoxon rank-sum test. Categorical data were compared using the χ^2 test. Descriptive statistics for the transformed marker were compared using box plots and then using analysis of variance. Youden's index was calculated as an index of sensitivity and specificity. To determine the optimal cut-off values for DCP and AFP to diagnose HCC, receiver operating characteristic

Table 1. Laboratory results for five groups of subjects

Items	HCC group (n = 550)	Malignant Disease group (n = 164)	Benign disease group (n = 181*)	Chronic liver disease group (n = 85)	Normal group (n = 173)	P**
Median age (range) (year)	51 (15-82)	56 (31-83)	50 (12-83)	32 (22-46)	28 (21-46)	
Gender (male / female)	480 / 70	110 / 54	84 / 97	70 / 15	132 / 41	
HBsAg						< 0.001
Positive (cases)	408	43 ^{†a}	44 ^{†b}	79	0	
Anti-HCV						
Positive (cases)	10	0	1 [‡]	6	0	
DCP level (mAU/mL)						< 0.001
Median	516.50	27.93	20.00	48.78	29.91	
Minimum	< 10.00	< 10.00	< 10.00	22.20	< 10.00	
Maximum	> 200,000.00	48,193.50	129,297.83	178.78	104.97	
AFP level (ng/mL)						< 0.001
Median	237.40	2.81	2.30	7.00	6.00	
Minimum	0.24	0.20	0.20	1.00	0.00	
Maximum	1,939,000.00	3,098.00	1,082.20	25.00	30.00	

* HBsAg results were missing for 11 patients; ^{†a} including 6 patients with HBV-related cirrhosis proven by pathology; ^{†b} including 20 patients with HBV-related cirrhosis proven by pathology; [‡] including 1 patients with HCV-related cirrhosis proven by pathology. ** patients with HCC vs. the other four groups of subjects, respectively.

(ROC) curves were created using all possible cut-offs for each assay. A bivariate normal distribution for the two markers was assumed. A 2-tailed *p* value of < 0.05 was used to determine statistical significance. All statistical analyses were performed using the statistical software package SPSS® version 22.0 for Windows® (SPSS, Chicago, Illinois, USA).

3. Results

3.1. Baseline characteristics

As shown in Table 1, there were 550 cases in HCC group, 164 in Malignant disease group, 181 in Benign disease group, 85 in Chronic liver disease group, and 173 in Normal group.

For the 550 patients with HCC, 74.18% (408 patients) were infected with HBV, which was significantly higher than that in patients with malignant disease and patients with benign disease (*P* < 0.001). Chronic liver disease group included 79 patients who were positive for HBsAg. Of 1,153 subjects in total, only 17 patients were positive for anti-HCV antibodies (10 cases in HCC group, 1 in Benign disease group, and 6 in Chronic liver disease group).

The median levels of DCP and AFP in patients with HCC were 516.50 mAU/mL (range: 10-200,000 mAU/mL) and 237.40 ng/mL (range: 0.24-1,939,000 ng/mL), which were significantly higher than those in the other four groups of subjects (*P* < 0.001) (Table 1). There was no significant correlation between serum levels of DCP and AFP ($R^2 = 0.154$) (Figure 1). When a cut-off value of 40 mAU/ml, reported to be the upper limit of normal for Japanese subjects (21), was used, 82.91% of patients in HCC group, 38.31% of patients in Malignant disease group, 27.75% of patients in Benign disease group, 61.18% of patients in Chronic liver disease

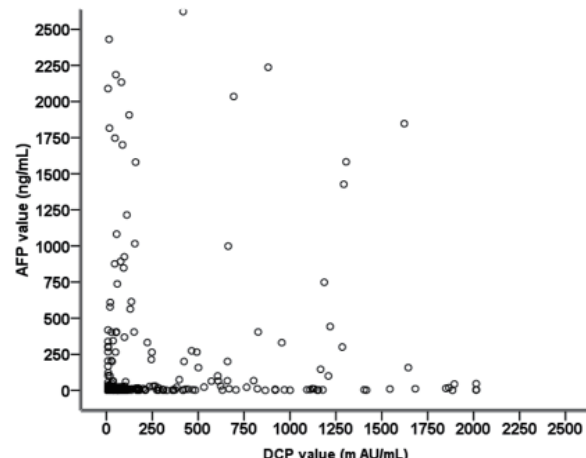


Figure 1. The correlation between serum levels of DCP and AFP ($R^2 = 0.154$).

group, and 34.68% of subjects in Normal group had elevated DCP levels. When using a cut-off value of 10 ng/mL as the upper limit of normal reported in Chinese subjects, 74.80% of patients in HCC group, 20.83% of patients in Malignant disease group, 12.50% of patients in Benign disease group, 28.24% of patients in Chronic liver disease group, and 30.06% of subjects in Normal group had elevated AFP levels (Figure 2).

3.2. Optimal cut-off values for DCP and AFP in differentiating patients with HCC from the other four groups of subjects studied

ROC curves were plotted to identify a cut-off value that would best distinguish patients with HCC from the other four groups of subjects. As shown in Figure 3, the optimal cut-off value for DCP was 86 mAU/ml, which yielded a sensitivity of 71.50% and specificity

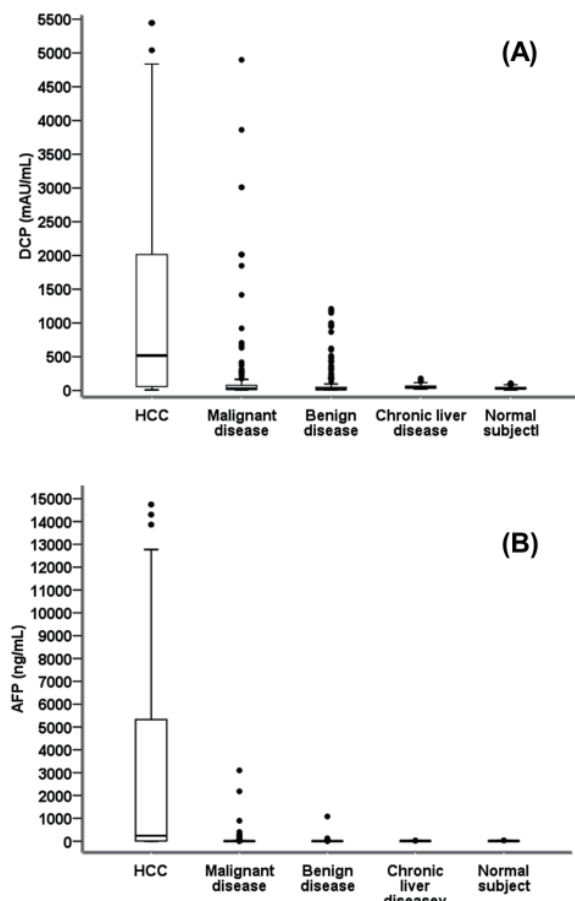


Figure 2. Scatter plot for DCP levels (A) and AFP levels (B) in 5 groups of subjects.

of 86.30%; the optimal cut-off value for AFP was 21 ng/mL, which yielded a sensitivity of 68.00% and specificity of 93.20%. The area under the ROC curve was 0.846 (95% CI, 0.794-0.863, $P < 0.001$) for DCP, 0.832 (95% CI, 0.817-0.879, $P < 0.001$) for AFP, and 0.890 (95% CI, 0.869- 0.911, $P < 0.001$) for the combination of DCP and AFP.

When using DCP with the cut-off value of 86 mAU/ml, 71.45% of patients in HCC group, 22.08% of patients in Malignant disease group, 15.61% of patients in Benign disease group, 11.76% of patients in Chronic liver disease group, and 5.20% of subjects in Normal group had elevated DCP levels.

When using AFP with the cut-off value of 21 ng/mL, 68.01% of patients in HCC group, 9.03% of patients in Malignant disease group, 7.29% of patients in Benign disease group, 3.53% of patients in Chronic liver disease group, and 5.20% of subjects in Normal group had elevated AFP levels.

3.3. Sensitivity, specificity, and predictive values of DCP and AFP in differentiating patients with HCC from the other four groups of subjects studied

As shown in Table 2, DCP with a cut-off value of 86 mAU/mL had a high specificity and positive predictive

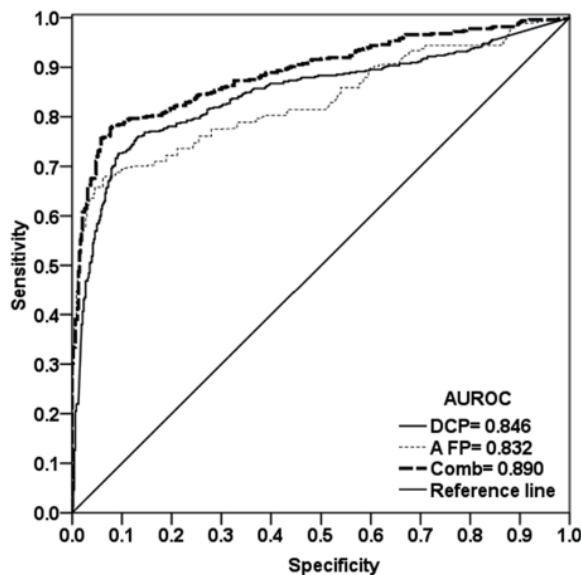


Figure 3. ROC curve comparing DCP and AFP levels in patients with HCC versus patients without HCC (including patients with malignant disease, patients with benign disease, patients with chronic liver disease, and normal subjects). The curves show an optimal cut-off value for DCP of 86 mAU/mL and for AFP of 21 ng/mL. The area under the ROC curve was 0.846 for DCP, 0.832 for AFP, and 0.890 for the combination of DCP and AFP.

value (PPV) but a lower sensitivity and negative predictive value (NPV) than a cut-off value of 40 mAU/mL. The Youden index for DCP with a cut-off value of 86 mAU/mL was 49.40% (HCC group vs. Malignant disease group), 55.90% (HCC group vs. Benign disease group), 58.70% (HCC group vs. Chronic liver disease group), and 66.30% (HCC group vs. Normal group), which were higher than that of DCP with cut-off value of 40 mAU/mL.

As the cut-off AFP value increased from 10 ng/mL to 400 ng/mL, its specificity and PPV increased but its sensitivity and NPV decreased. The Youden index for AFP with a cut-off value of 21 ng/mL was 59.00% (HCC group vs. Malignant disease group), 60.70% (HCC group vs. Benign disease group), 64.50% (HCC group vs. Chronic liver disease group), and 62.80% (HCC group vs. Normal group), which were higher than those for AFP with a cut-off value of 10 ng/mL or 400 ng/mL. The combination of DCP with a cut-off value of 86 mAU/ml and AFP with a cut-off value of 21 ng/mL had a greater sensitivity and a higher Youden index than DCP or AFP alone in differentiating patients with HCC from the other four groups of subjects, regardless of other cut-off value chosen.

3.4. DCP and AFP levels according to tumor size

In the 550 patients with HCC, the median DCP level increased from 93.91 mAU/mL to 2014.00 mAU/mL along with the enlargement of tumor size. For patients with a tumor > 10.0 cm, the median AFP level was

Table 2. The clinical utility of DCP and AFP with different cut-off values in differentiating HCC patients from other groups of subjects

DCP/AFP (cut-off value)	Sensitivity (%)	Specificity (%)	PPV (%)	NPV (%)	Youden Index (%)
DCP (86 mAU/mL)					
HCC group vs. Malignant disease group	71.50	77.90	92.04	43.32	49.40
HCC group vs. Benign disease group	71.50	84.40	93.57	48.18	55.90
HCC group vs. Chronic liver disease group	71.50	88.20	97.52	32.33	58.70
HCC group vs. Normal group	71.50	94.80	97.76	51.09	66.30
DCP (40 mAU/mL)					
HCC group vs. Malignant disease group	82.90	61.70	88.54	50.26	44.60
HCC group vs. Benign disease group	82.90	72.30	90.48	57.08	45.20
HCC group vs. Chronic liver disease group	82.90	38.80	89.76	25.98	21.70
HCC group vs. Normal group	82.90	65.30	88.37	54.59	48.20
AFP (10 ng/mL)					
HCC group vs. Malignant disease group	74.80	79.00	92.52	47.48	53.80
HCC group vs. Benign disease group	74.80	87.50	96.87	40.19	62.30
HCC group vs. Chronic liver disease group	74.80	71.80	93.92	32.80	46.60
HCC group vs. Normal group	74.80	69.90	87.71	49.19	44.70
AFP (21 ng/mL)					
HCC group vs. Malignant disease group	68.00	91.00	96.30	45.17	59.00
HCC group vs. Benign disease group	68.00	92.70	97.97	35.89	60.70
HCC group vs. Chronic liver disease group	68.00	96.50	99.12	34.02	64.50
HCC group vs. Normal group	68.00	94.80	97.40	50.77	62.80
AFP (400 ng/mL)					
HCC group vs. Malignant disease group	45.10	97.20	98.25	33.90	42.30
HCC group vs. Benign disease group	45.10	99.00	99.56	25.82	44.10
HCC group vs. Chronic liver disease group	45.10	100.00	100.00	23.74	54.90
HCC group vs. Normal group	45.10	100.00	100.00	38.79	54.90
AFP (21 ng/mL) + DCP (86 mAU/mL)					
HCC group vs. Malignant disease group	82.90	75.20	91.93	56.28	58.10
HCC group vs. Benign disease group	82.90	82.30	93.44	61.32	65.20
HCC group vs. Chronic liver disease group	82.90	84.70	97.23	43.37	67.60
HCC group vs. Normal group	82.90	90.80	96.61	62.55	73.70

PPV, positive predictive value; NPV, negative predictive value.

Table 3. DCP and AFP levels in 550 patients with HCC according to tumor size

Size of tumor	Median		Minimum		Maximum	
	DCP (mAU/mL)	AFP (ng/mL)	DCP (mAU/mL)	AFP (ng/mL)	DCP (mAU/mL)	AFP (ng/mL)
≤ 2.0 cm	93.91	216.10	< 10.00	0.24	7,369.15	59,615.00
> 2.0 cm, ≤ 3.0cm	191.82	391.93	< 10.00	1.83	46,825.61	1,647,080.00
> 3.0 cm, ≤ 4.0cm	462.78	126.90	< 10.00	1.38	> 200,000.00	366,417.00
> 4.0 cm, ≤ 5.0cm	556.88	174.00	< 10.00	0.82	111,170.15	1,193,000.00
> 5.0 cm, ≤ 10.0cm	1,278.91	200.00	< 10.00	0.24	> 200,000.00	794,800.00
> 10.0 cm	2,014.00	2,265.00	< 10.00	1.00	> 200,000.00	1,939,000.00

2,265.00 ng/mL, which was significantly higher than that in patients with a smaller tumor (Table 3).

Among the 550 patients with HCC, 41 cases were with the tumor size of ≤ 2.0 cm, with the median values for DCP as 93.01 mAU/mL (range: 10-7,369.15 mAU/mL), and for AFP as 216.10 ng/mL (range: 0.24-59,615.00 ng/mL); 99 cases were with the tumor size of ≤ 3.0 cm, the median values for DCP as 134.59 mAU/mL (range: 10-46,825.61 mAU/mL), and for AFP as 297.63 ng/mL (range: 0.24-1,647,080.00 ng/mL); 205 cases were with the tumor size of ≤ 5.0 cm, the median

values for DCP as 280.87 mAU/mL (range: 10-200,000 mAU/mL), and for AFP as 206.40 (range: 0.24-1,647,080.00 ng/mL).

3.5. The sensitivity of DCP and AFP in diagnosing patients with HCC according to tumor size

As shown in Table 4, the sensitivity of DCP with a cut-off value of 86 mAU/ml increased from 53.70% to 86.00% along the enlargement of tumor size. The combination of DCP with a cut-off value of 86 mAU/

Table 4. The sensitivity of DCP and AFP in the diagnosis of 550 patients with HCC according to tumor size

Size of tumor	DCP (86 mAU/mL) (%)	AFP (21 ng/mL) (%)	DCP (86 mAU/mL) + AFP (21 ng/mL) (%)
≤ 2.0 cm	53.66	80.49	92.68
> 2.0 cm, ≤ 3.0 cm	69.00	75.90	87.90
> 3.0 cm, ≤ 4.0 cm	76.50	58.80	88.20
> 4.0 cm, ≤ 5.0 cm	72.70	58.20	87.30
> 5.0 cm, ≤ 10.0 cm	80.50	65.80	88.40
> 10.0 cm	86.00	79.10	94.20

ml and AFP with a cut-off value of 21 ng/mL resulted in a sensitivity of approximately 90%, which was significantly higher than that for DCP or AFP alone.

For 41 cases with the tumor size of ≤ 2.0 cm, the combination of DCP with a cut-off value of 86 mAU/ml and AFP with a cut-off value of 21 ng/mL resulted in a sensitivity of 92.68%, which was higher than that of DCP (53.66%) or AFP (80.49%) alone ($P < 0.001$). For 99 cases with the tumor size of ≤ 3.0 cm, the combination of DCP and AFP with those cut-off values resulted in a sensitivity of 89.90%, which was higher than that of DCP (62.63%) or AFP (77.78%) alone ($P < 0.001$). For 205 cases with the tumor size of ≤ 5.0 cm, the combination of DCP and AFP with those cut-off values resulted in a sensitivity of 88.78%, which was also higher than that of DCP (68.78%) or AFP (67.80%) alone ($P < 0.001$).

4. Discussion

In China, HCC has currently become the second leading cause of cancer-related deaths in men and the third leading cause of such deaths in women, and its incidence has increased in the past few decades as a result of the high prevalence of its main etiological factor, chronic HBV infection (3,4). In fact, 93 million HBV carriers are Chinese, accounting for 2/3 of such patients worldwide, and about 20 million of these people have chronic HBV infection (5,22). Early diagnosis of HCC is essential when curative interventions can be implemented to improve patient prognosis and long-term survival (23,24). Thus, the early diagnosis for Chinese HCC patients predominantly caused by HBV infection has important implications not only for China, but also for the worldwide to reduce the burden of disease.

Serum biomarkers are attractive potential tools for HCC early diagnosis because they would enable non-invasive, objective, and reproducible assessments (25). In China, AFP has been recommended by HCC guidelines as a serum biomarker for diagnosis and it has been widely used in clinical practice (26), but its disadvantage of low sensitivity, low specificity, and limited accuracy in detecting small HCC diminish its clinical utility in HCC early diagnosis (7-11). Thus, other reliable serum biomarkers need to soon be identified to complement AFP in order to improve

clinical outcomes for patients with HCC in China.

DCP is an abnormal prothrombin that lacks carboxylation of specific amino-terminal glutamic acid residues. Since Liebman *et al.* found DCP to be a useful serum marker in diagnosing HCC in 1984 (27), differences in the sensitivity and specificity of DCP and AFP have been extensively discussed. In 8 large case-controlled studies, serum DCP was found to have a sensitivity of 48-62%, a specificity of 81-98%, and a diagnostic accuracy of 59-84% in differentiating patients with HCC from those with cirrhosis; in comparison, serum AFP was found to have a sensitivity of 40-54%, a specificity of 88-97%, and a diagnostic accuracy of 64-76% (15,28). Although several studies of the two tumor markers have been reported, results of those studies conflicted with regard to the relative performance of those markers. Some studies showed that DCP has greater sensitivity than AFP, while other studies found no significant difference in the sensitivity of the two serum markers, but the combination of DCP and AFP, however, appeared to have greater sensitivity than either marker alone (28-31). These differences may be due to the use of different marker cut-off values in each study (40, 60, and 100 mAU/mL for DCP and 20-200 ng/mL for AFP), differences in underlying liver disease, tumor stage, or other aspects.

The present study analyzed the clinical utility of simultaneous measurement of AFP and DCP in differentiating Chinese HCC patients (71.18% with HBV infection) from those patients with non-HCC and normal subjects. Results showed that the combined testing of DCP with a cut-off value of 86 mAU/ml and AFP with a cut-off value of 21 ng/mL resulted in a greater sensitivity and higher Youden index than DCP or AFP alone in differentiating patients with HCC from the other four groups of subjects, which suggest that the simultaneous measurement of AFP and DCP is effective in HCC diagnosis for Chinese patients predominantly caused by HBV infection.

Some studies have reported that the serum levels of DCP increase in relation to the size of HCC (30,32,33), it was also shown in our study that for patients with HCC, the median DCP level increased with a larger tumor. In the current study, the combination of DCP with a cut-off value of 86 mAU/mL and AFP with a cut-off value of 21 ng/mL resulted in a sensitivity of approximately 90%, which was significantly higher

than that for DCP or AFP alone. The same was true even for a tumor smaller than 2.0 cm. These results suggest that the simultaneous measurement of AFP and DCP may facilitate the diagnosis of patients with a broad range of HCC.

In conclusion, the simultaneous measurement of AFP and DCP could achieve a better sensitivity in diagnosing Chinese HCC patients, even for small tumors. To improve the diagnostic ability of serum biomarkers for HCC in China, the combined usage of AFP and DCP is suggested by this multi-center case-controlled study.

Acknowledgements

This work was supported by Grants-in-Aid from the Ministry of Education, Science, Sports, and Culture of Japan and the Japan-China Liver Cancer Research Project of the International Research Cooperation Association for Bio & Socio-Sciences Advancement.

References

- World Health Organization. GLOBOCAN 2012: Estimated Cancer Incidence, Mortality and Prevalence Worldwide in 2012. http://globocan.iarc.fr/Pages/fact_sheets_cancer.aspx (accessed September 8, 2014).
- Asia-Pacific Working Party on Prevention of Hepatocellular C. Prevention of hepatocellular carcinoma in the Asia-Pacific region: Consensus statements. *J Gastroenterol Hepatol.* 2010; 25:657-663.
- Tanaka M, Katayama F, Kato H, Tanaka H, Wang J, Qiao YL, Inoue M. Hepatitis B and C virus infection and hepatocellular carcinoma in China: A review of epidemiology and control measures. *J Epidemiol.* 2011; 21:401-416.
- Yuen MF, Hou JL, Chutaputti A. Hepatocellular carcinoma in the Asia pacific region. *J Gastroenterol Hepatol.* 2009; 24:346-353.
- Song PP, Feng X, Zhang K, Song T, Ma K, Kokudo N, Dong J, Tang W. Perspectives on using des- γ -carboxyprothrombin (DCP) as a serum biomarker: Facilitating early detection of hepatocellular carcinoma in China. *Hepatobiliary Surg Nutr.* 2013; 2:227-231.
- Zhang BH, Yang BH, Tang ZY. Randomized controlled trial of screening for hepatocellular carcinoma. *J Cancer Res Clin Oncol.* 2004; 130:417-422.
- Daniele B, Bencivenga A, Megna AS, Tinessa V. Alpha-fetoprotein and ultrasonography screening for hepatocellular carcinoma. *Gastroenterology.* 2004; 127 (Suppl 1):S108-S112.
- Marrero JA. Screening tests for hepatocellular carcinoma. *Clin Liver Dis.* 2005; 9:235-251, vi.
- Di Bisceglie AM, Hoofnagle JH. Elevations in serum alpha-fetoprotein levels in patients with chronic hepatitis B. *Cancer.* 1989; 64:2117-2120.
- Colli A, Fraquelli M, Casazza G, Massironi S, Colucci A, Conte D, Duca P. Accuracy of ultrasonography, spiral CT, magnetic resonance, and alpha-fetoprotein in diagnosing hepatocellular carcinoma: A systematic review. *Am J Gastroenterol.* 2006; 101:513-523.
- Tateishi R, Yoshida H, Matsuyama Y, Mine N, Kondo Y, Omata M. Diagnostic accuracy of tumor markers for hepatocellular carcinoma: A systematic review. *Hepatol Int.* 2008; 2:17-30.
- Marrero JA, Feng Z, Wang Y, et al. Alpha-fetoprotein, des-gamma carboxyprothrombin, and lectin-bound alpha-fetoprotein in early hepatocellular carcinoma. *Gastroenterology.* 2009; 137:110-118.
- Sassa T, Kumada T, Nakano S, Uematsu T. Clinical utility of simultaneous measurement of serum high-sensitivity des-gamma-carboxy prothrombin and Lens culinaris agglutinin A-reactive alpha-fetoprotein in patients with small hepatocellular carcinoma. *Eur J Gastroenterol Hepatol.* 1999; 11:1387-1392.
- Shimauchi Y, Tanaka M, Kuromatsu R, Ogata R, Tateishi Y, Itano S, Ono N, Yutani S, Nagamatsu H, Matsugaki S, Yamasaki S, Tanikawa K, Sata M. A simultaneous monitoring of Lens culinaris agglutinin A-reactive alpha-fetoprotein and des-gamma-carboxy prothrombin as an early diagnosis of hepatocellular carcinoma in the follow-up of cirrhotic patients. *Oncol Rep.* 2000; 7:249-256.
- Durazo FA, Blatt LM, Corey WG, Lin JH, Han S, Saab S, Busuttil RW, Tong MJ. Des-gamma-carboxyprothrombin, alpha-fetoprotein and AFP-L3 in patients with chronic hepatitis, cirrhosis and hepatocellular carcinoma. *J Gastroenterol Hepatol.* 2008; 23:1541-1548.
- Fujiyama S, Izuno K, Yamasaki K, Sato T, Taketa K. Determination of optimum cutoff levels of plasma des-gamma-carboxy prothrombin and serum alpha-fetoprotein for the diagnosis of hepatocellular carcinoma using receiver operating characteristic curves. *Tumour Biol.* 1992; 13:316-323.
- Izumi N. Diagnostic and treatment algorithm of the Japanese society of hepatology: A consensus-based practice guideline. *Oncology.* 2010; 78 (Suppl 1):78-86.
- Song PP, Gao JJ, Inagaki Y, Kokudo N, Hasegawa K, Sugawara Y, Tang W. Biomarkers: Evaluation of Screening for and Early Diagnosis of Hepatocellular Carcinoma in Japan and China. *Liver Cancer.* 2013; 2:31-39.
- Cui R, Wang B, Ding H, Shen H, Li Y, Chen X. Usefulness of determining a protein induced by vitamin K absence in detection of hepatocellular carcinoma. *Chin Med J (Engl).* 2002; 115:42-45.
- Cui R, He J, Zhang F, Wang B, Ding H, Shen H, Li Y, Chen X. Diagnostic value of protein induced by vitamin K absence (PIVKAI) and hepatoma-specific band of serum gamma-glutamyl transferase (GGTII) as hepatocellular carcinoma markers complementary to alpha-fetoprotein. *Br J Cancer.* 2003; 88:1878-1882.
- Nakamura S, Nouso K, Sakaguchi K, Ito YM, Ohashi Y, Kobayashi Y, Toshikuni N, Tanaka H, Miyake Y, Matsumoto E, Shiratori Y. Sensitivity and specificity of des-gamma-carboxy prothrombin for diagnosis of patients with hepatocellular carcinomas varies according to tumor size. *Am J Gastroenterol.* 2006; 101:2038-2043.
- Zhang C, Zhong Y, Guo L. Strategies to prevent hepatitis B virus infection in China: immunization, screening, and standard medical practices. *Biosci Trends.* 2013; 7:7-12.
- Amarapurkar D, Han KH, Chan HL, Ueno Y, Asia-Pacific Working Party on Prevention of Hepatocellular C. Application of surveillance programs for hepatocellular carcinoma in the Asia-Pacific Region. *J Gastroenterol Hepatol.* 2009; 24:955-961.

24. Llovet JM, Burroughs A, Bruix J. Hepatocellular carcinoma. Lancet. 2003; 362:1907-1917.
25. Forner A, Bruix J. Biomarkers for early diagnosis of hepatocellular carcinoma. Lancet Oncol. 2012; 13:750-751.
26. Song P, Tobe RG, Inagaki Y, Kokudo N, Hasegawa K, Sugawara Y, Tang W. The management of hepatocellular carcinoma around the world: A comparison of guidelines from 2001 to 2011. Liver Int. 2012; 32:1053-1063.
27. Liebman HA, Furie BC, Tong MJ, Blanchard RA, Lo KJ, Lee SD, Coleman MS, Furie B. Des-gamma-carboxy (abnormal) prothrombin as a serum marker of primary hepatocellular carcinoma. N Engl J Med. 1984; 310:1427-1431.
28. Marrero JA, Su GL, Wei W, Emick D, Conjeevaram HS, Fontana RJ, Lok AS. Des-gamma carboxyprothrombin can differentiate hepatocellular carcinoma from nonmalignant chronic liver disease in american patients. Hepatology. 2003; 37:1114-1121.
29. Ishii M, Gama H, Chida N, Ueno Y, Shinzawa H, Takagi T, Toyota T, Takahashi T, Kasukawa R. Simultaneous measurements of serum alpha-fetoprotein and protein induced by vitamin K absence for detecting hepatocellular carcinoma. South Tohoku District Study Group. Am J Gastroenterol. 2000; 95:1036-1040.
30. Fujiyama S, Izuno K, Gohshi K, Shibata J, Sato T. Clinical usefulness of des-gamma-carboxy prothrombin assay in early diagnosis of hepatocellular carcinoma. Dig Dis Sci. 1991; 36:1787-1792.
31. Grazi GL, Mazziotti A, Legnani C, Jovine E, Miniero R, Gallucci A, Palareti G, Gozzetti G. The role of tumor markers in the diagnosis of hepatocellular carcinoma, with special reference to the des-gamma-carboxy prothrombin. Liver Transpl Surg. 1995; 1:249-255.
32. Kasahara A, Hayashi N, Fusamoto H, Kawada Y, Imai Y, Yamamoto H, Hayashi E, Ogihara T, Kamada T. Clinical evaluation of plasma des-gamma-carboxy prothrombin as a marker protein of hepatocellular carcinoma in patients with tumors of various sizes. Dig Dis Sci. 1993; 38:2170-2176.
33. Weitz IC, Liebman HA. Des-gamma-carboxy (abnormal) prothrombin and hepatocellular carcinoma: A critical review. Hepatology. 1993; 18:990-997.

(Received October 22, 2014; Accepted October 28, 2014)

Relationship between renal apparent diffusion coefficient values and glomerular filtration rate in infants with congenital hydronephrosis

Feifei Lin¹, Zhiyong Li¹, Yungen Gan¹, Longwei Sun¹, Diangang Fang¹, Kui Xiang¹, Lei Liu^{2,*}

¹Department of Radiology, The Children Hospital of Shenzhen, Shenzhen, China;

²Department of Paediatrics, The Children Hospital of Shenzhen, Shenzhen, China.

Summary

The aim was to investigate the relationship between apparent diffusion coefficient (ADC) values measured by diffusion-weighted magnetic resonance imaging (DW MRI) and the split glomerular filtration rate (GFR) in infants with congenital hydronephrosis. Diffusion-weighted imaging (DWI) ($b = 0$ and 700 seconds/mm 2) was performed with a General Electric Company (GE) Signa 1.5T MR unit in 46 infants suffering single congenital hydronephrosis and in 30 healthy infants as normal control group. The ADCs were calculated with regions of interest (ROIs) positioned in the renal parenchyma. The 46 obstructed kidneys were classified into four groups according to the GFR level: renal dysfunction compensated group, renal dysfunction decompensated group, renal failure group, and uremia group. The renal ADCs in six groups (normal kidneys in control group, contralateral kidneys, and four groups of hydronephrotic kidneys) were compared statistically using analysis of variance (ANOVA), and the correlative relationship between ADCs and GFR was examined by Pearson's correlation test. There were statistically significant differences in renal ADCs among the six groups. The ADCs of hydronephrotic kidneys were lower than that of the normal kidneys. There was a moderate positive correlation between the ADCs of hydronephrotic kidneys and split GFR ($r = 0.744$). This study indicated that the ADCs of congenital hydronephrotic kidneys were lower than that of normal renal parenchyma, and there was a positive correlation between the ADCs and split renal GFR, which demonstrates that the ADCs can reflect the filtration function of hydronephrotic kidneys and may provide some reference to help clinical physician to explore a novel noninvasive approach to evaluate the single renal function.

Keywords: Congenital hydronephrosis, glomerular filtration rate, apparent diffusion coefficient, magnetic resonance imaging, diffusion-weighted imaging

1. Introduction

Obstruction at ureteropelvic junction, often referred to as congenital hydronephrosis is a common disease for infants with 0.13-0.16% incidence (1). It is essential for the clinical physician to understand the morphology and the function of hydronephrotic and contralateral kidneys in order to choose the appropriate clinical therapeutic

protocols. Currently, it is debatable in the determination of the function of hydronephrotic kidneys, and there is still no satisfactory non-invasive diagnostic method to evaluate the damage degree of unilateral involved kidney and to predict the restoration of renal function after operation.

Diffusion-weighted magnetic resonance imaging (DW MRI) is a technique used to measure and image the diffusion of water molecule, can reflect Brownian motion of water molecule in tissue and serve as a functional imaging to represent the functional condition of living tissue *in vivo*, which is a hot research area in recent years. Apparent diffusion coefficient (ADC) is a quantitative index for diffusion-weighted imaging (DWI), can provide the quantification standard for

*Address correspondence to:

Dr. Lei Liu, Department of Paediatrics, The Children Hospital of Shenzhen, Honglixi Street 7019, Futian District, Shenzhen 518026, Guangdong, China.
E-mail: 2597256665@qq.com

disease diagnosis through the different ADC values in diverse pathological changes.

With affluent blood supply and highly water-contained content, kidneys are one of the ideal organs for DWI examination in abdominal viscera (2,3). Considerable attention has been made to investigate the renal DWI across the world (4-6), and some recent studies had demonstrated that the DWI has potential clinical value in evaluating some renal diseases (7-10), such as renal artery stenosis, diffuse renal disease, renal tumor and renal infection (11-15), etc. However, as a novel functional imaging for the investigation of renal function, the DWI is mainly applied in adult patients and the studies focusing on renal diffusion of infants is scarce, and no study at present was found with regard to using renal ADC values to explore the hydronephrotic kidney in single children population. Some research found that that the renal ADC values of infants would change considerably when age increases, and there is significant difference of renal ADC values among different age groups (16). As such, the aim of our study is to investigate the relationship between renal ADC values measured by DWI and glomerular filtration function in infants with congenital hydronephrosis, and the clinical application value of using renal ADC values to evaluate the renal function in hydronephrotic kidneys, with the expectation to provide evidence to help physician to find out a novel noninvasive approach of evaluating the split renal function in clinical practice.

2. Materials and Methods

2.1. Research subjects

Patients group: 46 infants suffering single hydronephrosis caused by congenital obstruction at ureteropelvic junction, between October 2008 and October 2009 (12 women and 34 men, age range is between 5 months to 3 years, mean age = 1.9 years), were included in our study, and all patients were diagnosed with ultrasonography, intravenous urography (IVU) and magnetic resonance urography (MRU), 26 of whom were confirmed by operation. Renal dynamic scintigraphy (^{99}mTc -DTPA, HTA CO. LTD., Guangzhou, Guangdong, China) was used to measure the split renal glomerular filtration rate (GFR) for all patients within one week of MRI examination and the field of view (FOV) included both kidneys. Dynamic collection was performed immediately after "bolus" intravenous injection of ^{99}mTc -DTPA and the split GFR was calculated separately. The patients were divided into four groups according to degree of renal insufficiency: renal dysfunction compensated group (reduced GFR but is greater than 50 mL/min, serum creatinine and blood urea nitrogen are normal, 9 cases), renal dysfunction decompensated group (25 mL/min \leq GFR < 50 mL/min, 13 cases), renal failure group (10 mL/min \leq GFR

< 25 mL/min, 21 cases), and uremia group (GFR < 10 mL/min, 3 cases). No obviously abnormal features were observed in 46 kidneys in the contralateral side assessed by ultrasound, IVU and MRI.

Control group: 30 normal and healthy infants (8 women and 22 men, age range is between 4 months to 3 years, mean age = 1.7 years) were selected randomly. Inclusion criteria: (i) no clinical history of renal diseases; (ii) no present clinical manifestations of renal diseases; (iii) all the laboratory results related to renal function are normal, which mainly include serological examinations (such as blood urea nitrogen, uric acid, creatinine, potassium, sodium, chloride, etc. that are relevant to the renal function) and routine urine test; (iv) normal report of kidneys by MRI; (v) no medication that may significantly affect renal function has been taken.

This study included six groups (normal kidneys in control group, contralateral kidneys, and four groups of hydronephrotic kidneys), and it was reviewed and approved by the Hospital Ethics Committee, and all the parents of the study subjects have signed informed consent form before the examinations.

2.2. MRI examination method

MRI examination was performed with a 1.5T MR imager (Signa; General Electric Company (GE), USA) with Torso phased-array coil. Before the examination, keep the stomach empty for 6 h and all the subjects were given sedative orally (10% chloral hydrate, Zhujiang Hospital, Guangzhou, Guangdong, China; 0.5 mL/kg.). During the examination, the subjects were dormant lying on the examining table and respiration was monitored by respiratory gating technique. The upper abdominal axial routine scan was performed (T_1 weighted imaging, T_2 weighted imaging, MRU and DWI), and the range included the long diameter of bilateral kidneys. Single shot spin-echo echo-planar imaging (SE-EPI) sequence was applied in DWI examination. Scan parameters: TR 3000ms, TE 6.6-70.5ms, FOV 30 cm \times 30 cm, reconstruction matrix (RES) 128 \times 128, thickness = 4 mm, interval = 1 mm, NEX 8. Three directions of diffusion were measured simultaneously with two b values selected as 0 s/mm 2 and 700 s/mm 2 . Fat suppression was applied during the scan.

2.3. Images review and post-processing

The original data collected during the scan were transmitted to the post-processing workstation, and the DWI and ADC maps were automatically reconstructed using GE Functool software with ADC values of renal parenchyma being measured at ADC map. Given the low signal to noise ratio in EPI image, it is difficult to clearly differentiate the renal cortex and medulla. In order to reduce measurement errors, in this study,

the ADC values were measured on the whole renal parenchyma. Three planes, including the upper pole of kidneys (4-6 mm from renal upper border), renal hilum and lower renal pole (4-6 mm from renal lower border), were selected in each subject. Two regions of interest (ROIs) of each plane were delineated by two senior radiologists. The average area of the ROIs was about 25 mm², and the mean value was considered the final ADC value. The renal ADCs in six groups (normal kidneys in control group, contralateral kidneys, and four groups of hydronephrotic kidneys) were calculated.

2.4. Statistical analysis

Statistical analysis was performed with the SPSS 16.0. The significant differences of the renal ADCs values in six groups were assessed using completely randomized variance analysis (ANOVA), and the least-significant difference (LSD) method was used to compare the difference of ADC values between each two groups. The relationship between the renal ADC and split GFR was examined by Pearson's correlation coefficient

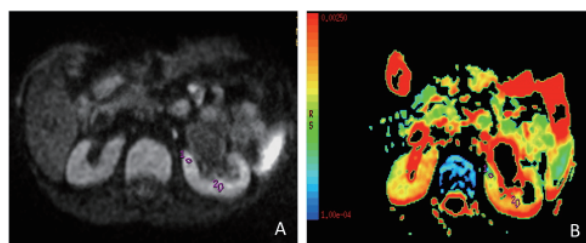


Figure 1. DWI (A) and ADC (B) map of a 36-month-old male infant with left-side congenital hydronephrosis belonging to renal dysfunction compensated group. Two ROIs in the parenchyma on the renal hilum section were delineated by two senior radiologists, and the average area of the ROIs was about 25 mm², and the mean value was considered the final ADC value.

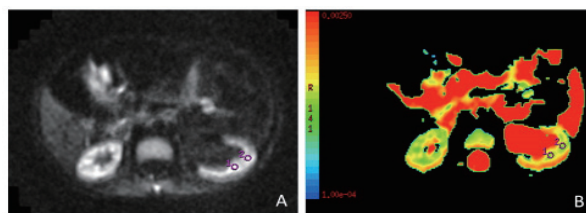


Figure 2. DWI (A) and ADC (B) map of a 36-month-old male infant with left-side congenital hydronephrosis belonging to renal dysfunction decompensated group. ROIs are manually delineated.

test. A *p*-value < 0.05 was considered statistically significant.

3. Results

The DWI images of all subjects were in accordance with the diagnosis standards without obvious distortion and artifacts (Figures 1-4).

The mean renal ADCs of six groups (normal renal parenchyma in control group, contralateral kidney group and four hydronephrotic kidney groups) were shown in Table 1. Significant difference was found between different groups ($F = 148.46, p < 0.001$). The renal ADCs in renal dysfunction compensated group were lower than that of contralateral kidney group, and the latter is lower than that of normal renal parenchyma in control group.

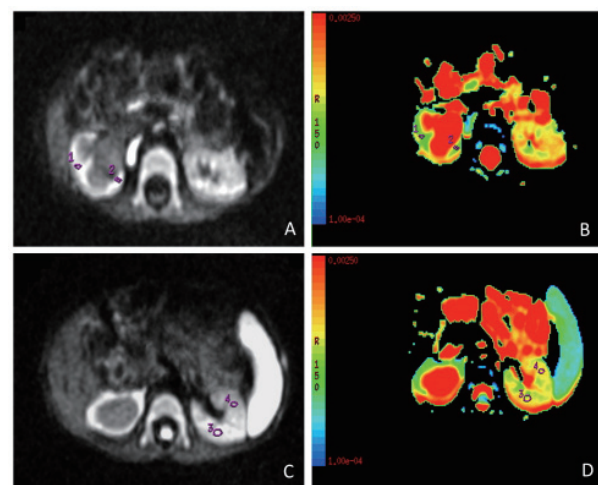


Figure 3. DWI (A, C) and ADC (B, D) map of a 24-month-old female infant with right-side congenital hydronephrosis belonging to renal failure group. The ADC value of the two renals was calculated alone.

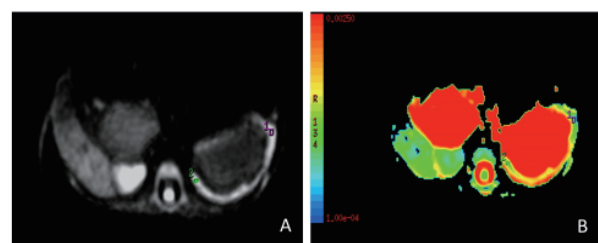


Figure 4. DWI (A) and ADC (B) map of a 5-month-old female infant with left-side congenital hydronephrosis belonging to uremia group. ROIs are manually delineated.

Table 1. The mean renal ADCs of six groups

Groups	Number of kidney	Mean of ADC values	95% confidence interval	Minimum	Maximum
Control group with normal renal parenchyma	60	1.61 ± 0.06	1.60 - 1.63	1.50	1.78
Contralateral kidney group	46	1.51 ± 0.10*	1.48 - 1.54	1.34	1.77
Renal dysfunction compensated group	9	1.46 ± 0.04*	1.43 - 1.49	1.18	1.53
Renal dysfunction decompensated group	13	1.33 ± 0.04	1.31 - 1.36	1.29	1.42
Renal failure group	21	1.22 ± 0.07	1.19 - 1.23	1.13	1.32
Uremia group	3	1.04 ± 0.03	0.97 - 1.12	1.01	1.07

*There was no statistically significance in ADC values between the contralateral kidney group and renal dysfunction compensated group. (*p* = 0.06).

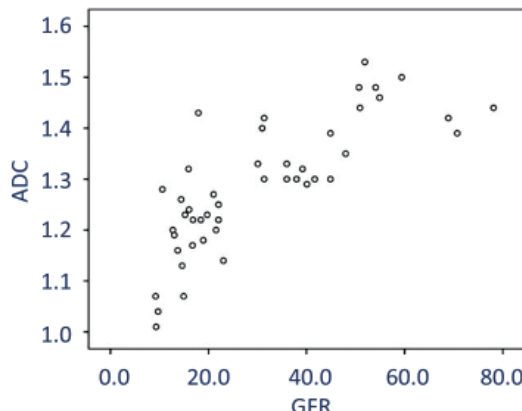


Figure 5. Relationship between ADC values of obstructed kidney with hydronephrosis and the split renal GFR. There was a moderate positive correlation ($r = 0.744, p < 0.001$).

When compared between each two groups, we observe that there was no significant difference of ADCs between renal dysfunction compensated group and contralateral kidney group ($p = 0.06$) and in the rest groups, significant difference was seen between each other ($p < 0.001$).

There was a moderate positive correlation between renal ADCs of the obstructed kidney with hydronephrosis and split renal GFR ($r = 0.744, p < 0.001$) (Figure 5).

No correlation was found between renal ADC values of the contralateral kidneys and split renal GFR ($r = 0.194, p < 0.001$) (Figure 6). The GFR range was 38.9–78 mL/min in contralateral kidney group and 2 out of 46 kidneys in this group was ≤ 50 mL/min.

4. Discussion

4.1. The change pattern of ADC values in hydronephrotic kidneys and the correlation with GFR

The accurate evaluation of renal function to hydronephrotic patients is essential for the diagnosis and treatment of this disease. The surgical operation timing relies on the location and degree of urinary obstruction, as well as the concise assessment of renal function and to what extent the renal function can be recovered after operation (17,18). Hydronephrosis will slow down the transportation of water, reduce transporting volume and restrict molecule movement. Meanwhile, the renal perfusion is reduced as well owing to the increased pressure in renal pelvis and calyces, as well as the collective effects of various cell and vasoactive factors on the renal blood supply. The pathophysiologic changes described above would certainly affect the diffusion in renal parenchyma and alter the ADCs. Our study showed that the ADCs of obstructed kidneys in infants with congenital hydronephrosis were lower than that of normal kidneys ($1.61 \pm 0.05 \times 10^{-3} \text{ mm}^2/\text{s}$), and the difference was significant, which conformed to the previous research results. Several animal experiments and clinical studies in adult (7,19) have shown that the

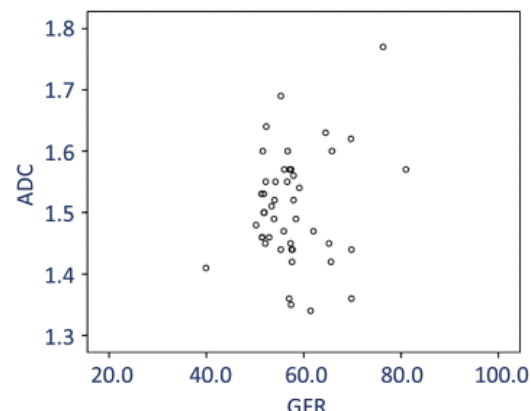


Figure 6. Relationship between ADC values of contralateral kidney with no hydronephrosis and the split renal GFR. There was no correlation ($r = 0.194, p < 0.001$).

ADCs dropped in hydronephrosis, and values of ADCs in hydronephrotic kidneys with impaired renal function were much lower than that of the contralateral kidneys with normal renal function (9,13,20). In patients with renal failure, the ADCs of cortex and medulla fell down in varying degree (7,21,22).

In acute phase of hydronephrosis, the interface between cortex and medulla is still visible. However, this differentiation would be no longer clear in chronic urinary tract obstruction (23). Fukuda *et al.* (8) had stated that there is a low signal-to-noise ratio in the kidney images with EPI sequences. As such, it would be difficult to exactly differentiate renal cortex and medulla in that situation and the measurement error will certainly increase when the ROIs are placed onto the cortex and medulla respectively. In addition, Xu *et al.* (11) reported no significant signal difference was found between the renal cortex and medulla in DWI. Therefore, the approach of placing the ROI on specific plane was adopted in this study to measure the ADCs of local renal parenchyma.

Our study indicated that there were significant differences in ADC values between each of four groups, including renal dysfunction compensated group ($1.46 \pm 0.04 \times 10^{-3} \text{ mm}^2/\text{s}$), renal dysfunction decompensated group ($1.33 \pm 0.04 \times 10^{-3} \text{ mm}^2/\text{s}$), renal failure group ($1.22 \pm 0.07 \times 10^{-3} \text{ mm}^2/\text{s}$) and uremia group ($1.04 \pm 0.03 \times 10^{-3} \text{ mm}^2/\text{s}$). The ADC values in renal dysfunction compensated group were lower than that of contralateral kidney group, and significant difference of ADCs was observed between renal failure group and uremia group. Xu *et al.* (12), however, had reported that there was no significant difference of renal ADCs between moderate and severe renal function injury groups when they investigated the healthy people and patients with chronic kidney disease. The authors believed that the reason may be attributed to the small sample in severe renal function injury group. In addition, the criteria they adopted for moderate renal function injury group is different from the renal failure group in our study

($10 \text{ mL/min} \leq \text{GFR} < 20 \text{ mL/min}$ versus $10 \text{ mL/min} \leq \text{GFR} < 25 \text{ mL/min}$), which may lead to the differential conclusion.

The research by Thoeny *et al.* (8) in healthy volunteers demonstrated that DW MRI had a fairly good repeatability in evaluating the changes of renal function, and thus can be performed as a non-invasive follow-up approach to monitor the degree and changes of abnormal renal function. But more research with larger sample size may be required to confirm this observation.

4.2. The change pattern of ADC values in contralateral kidneys and the correlation with GFR

Harriet *et al.* (13) found there was various degree of difference of ADCs between the involved kidney and contralateral kidney in patients with urinary tract obstruction. Our research results showed that the renal ADC values of hydronephrotic kidneys in renal dysfunction compensated group were lower than that of contralateral kidneys but with no significant difference, while the renal ADCs in both groups were lower than that of normal control group. Base on the grouping criteria of renal insufficiency, the GFR of renal dysfunction compensated group is reduced but above 50 mL/min, so the ADCs were lower than that of normal kidneys. Given the fact that no structural lesion is observed in contralateral kidneys, and the partial contralateral kidneys after obstruction would present some level of functional compensation, the renal ADC values of involved kidney in renal dysfunction compensated group were lower than that of contralateral kidneys. In our study, the insignificant difference of ADCs between involved kidney and contralateral kidney may result from the insignificant difference of GFR between them. In addition, in two out of 46 contralateral kidneys, the GFR level is from 25-50 mL/min. Therefore, a larger sample might be required in future research to confirm the appropriateness of using contralateral kidney as the normal control group in the past researches. Toyoshima *et al.* (9) also believed that there were overlapping of the renal ADCs between hydronephrotic kidneys without renal injury ($1.63 \pm 0.12 \times 10^{-3} \text{ mm}^2/\text{s}$) and the contralateral kidneys with no hydronephrosis ($1.68 \pm 0.15 \times 10^{-3} \text{ mm}^2/\text{s}$). Müller *et al.* (2) found that the contralateral renal ADCs increased only slightly after urinary tract obstruction on one side.

Our study found that the renal ADC values in contralateral kidney group with no hydronephrosis were lower than that of normal kidney control group ($1.61 \pm 0.05 \times 10^{-3} \text{ mm}^2/\text{s}$), and no correlation with split renal GFR was found. In the research of adult hydronephrosis, whereas Toyoshima *et al.* (9) found that the renal ADCs of contralateral kidney without hydronephrosis were similar to that of normal kidney with no correlation with the split renal GFR. In our

study, the range of contralateral renal GFR was 38.9-79 mL/min, Two out of 46 cases had mild renal function damage ($\text{GFR} \leq 50 \text{ mL/min}$) without renal compensated hyperfunction. Some researchers have indicated that renal compensated hyperfunction in contralateral kidney can occur at early stage of hydronephrosis, but part of renal function was reduced at variable degree after 6-8 months from the occurrence of obstruction. However, the reason of no correlation between the renal ADC values of obstruction contralateral kidney without hydronephrosis and the single renal GFR is still to be further investigated.

4.3. Limitations of the study

Our study has several limits. (i) The number of hydronephrosis cases in uremic group was relatively small; (ii) There is still no accurate interpretation regarding no correlation between the ADCs of contralateral kidneys and split renal GFR; (iii) In order to investigate the relationship thoroughly between the renal ADC values of hydronephrotic kidneys and the split renal GFR, patient grouping with a broader range of age may be required; (iv) Only the ADC values of whole renal parenchyma was measured in this investigation, while we expect to be able to measure the renal cortex and medulla respectively in future research; (v) As GFR is an important index to evaluate the renal filtration function, we expect to investigate the relationship further between the renal ADC values and renal tubular function of split kidney; And as a functional measurement approach, there is a need to further investigate whether the DW MRI could reflect the functional changes in early stage lesions.

In sum, this study revealed that the renal ADC values of involved kidney in infants with congenital hydronephrosis were lower than that of the normal renal parenchyma, and there was a positive correlation between the ADC values of hydronephrotic kidneys and split renal GFR, which may indicate that ADC values are of certain value to evaluate the filtration function of hydronephrotic kidney, and may provide new direction to help clinical physician to find noninvasive novel approach to evaluate the single renal function.

Although the clinical application of renal DWI is to be investigated in depth, the MRI approach shows many advantages in evaluating renal function. For instance, it is non-invasive with no radiation. The combination of conventional MR imaging and DWI can provide the information of kidney morphology and function simultaneously. As DWI does not need using contrast medium, it won't bring any adverse reactions associated with radiation or contrast medium damage to the children during their development and growth period and thus is especially beneficial to the infant patients with allergy to contrast medium and/or impaired renal function. There is a reason to believe

that functional MRI will certainly demonstrate great prospects of clinical application in evaluating renal function in the future, and will play a more important role in the diagnosis of infants hydronephrosis.

Acknowledgements

The study was supported by a grant from the Science and Technology Foundation of Shenzhen (No. JCYJ20130401114111460) and the Children Hospital of Shenzhen. We thank Drs. Guohua Liang and Xianlei Meng for their technical assistance.

References

- Nguyen HT, Kogan BA. Upper urinary tract obstruction: Experimental and clinical aspects. *Br J Urol*. 1998; 81:13-21.
- Müller MF, Prasad PV, Bimmmer D, Kaiser A, Edelman RR. Functional imaging of the kidney by means of measurement of the apparent diffusion coefficient. *Radiology*. 1994; 193:711-715.
- Laissy JP, Menegazzo D, Dumont E, Piekarski JD, Karila-Cohen P, Chillon S, Schouman-Claeys E. Hemodynamic effect of iodinated high-viscosity contrast medium in the rat kidney: A diffusion-weighted MRI feasibility study. *Invest Radiol*. 2000; 35:647-652.
- Hackstein N, Heckrodt J, Rau WS. Measurement of single-kidney glomerular filtration rate using a contrast-enhanced dynamic gradient-echo sequence and the Rutland-Patlak plot technique. *J Magn Reson Imaging*. 2003; 18:714-725.
- Annet L, Hermoye L, Peeters F, Jamar F, Dehoux JP, Van Beers BE. Glomerular filtration rate: Assessment with dynamic contrast-enhanced MRI and a cortical-compartment model in the rabbit kidney. *J Magn Reson Imaging*. 2004; 20:843-849.
- Yildirim E, Kirbas I, Teksam M, Karadeli E, Gullu H, Ozer I. Diffusion-weighted MR imaging of kidneys in renal artery stenosis. *Eur J Radiol*. 2008; 65:148-153.
- Namimoto T, Yamashita Y, Mitsuzaki K, Nakayama Y, Tang Y, Takahashi M. Measurement of the apparent diffusion coefficient in diffuse renal disease by diffusion-weighted echo-planar imaging. *J Magn Reson Imaging*. 1999; 9:832-837.
- Fukuda Y, Ohashi I, Hanafusa K, Nakagawa T, Ohtani S, An-naka Y, Hayashi T, Shibuya H. Anisotropic diffusion in kidney: Apparent diffusion coefficient measurements for clinical use. *J Magn Reson Imaging*. 2000; 11:156-160.
- Toyoshima S, Noguchi K, Seto H, Shimizu M, Watanabe N. Functional evaluation of hydronephrosis by diffusion-weighted MR imaging: Relationship between apparent diffusion coefficient and split glomerular filtration rate. *Acta Radiol*. 2000; 41:642-646.
- Kim S, Naik M, Sigmund E, Taouli B. Diffusion-weighted MR imaging of the kidneys and the urinary tract. *Magn Reson Imaging Clin N Am*. 2008; 16:585-596.
- Xu X, Fang W, Ling H, Chai W, Chen K. Diffusion-weighted MR imaging of kidneys in patients with chronic kidney disease: initial study. *Eur Radiol*. 2010; 20:978-983.
- Xu YF, Wang XY, Jiang XX. Relationship between the renal apparent diffusion coefficient and glomerular filtration rate: Preliminary experience. *Magn Reson Imaging*. 2007; 26:678-681.
- Thoeny HC, De Keyzer F, Oyen RH, Peeters RR. Diffusion-weighted MR imaging of kidneys in healthy volunteers and patients with parenchymal Diseases: Initial experience. *Radiology*. 2005; 235:911-917.
- Cova M, Squillaci E, Stacul F, Manenti G, Gava S, Simonetti G, Pozzi-Mucelli R. Diffusion-weighted MRI in the evaluation of renal lesions: Preliminary results. *British Journal of Radiology*. 2004; 77:851-857.
- Sandrasegaran K, Sundaram CP, Ramaswamy R, Akisik FM, Rydberg MP, Lin C, Aisen AM. Usefulness of diffusion-weighted imaging in the evaluation of renal masses. *AJR Am J Roentgenol*. 2010; 194:438-445.
- Jones RA, Grattan-Smith JD. Age dependence of the renal apparent diffusion coefficient in children. *Pediatr Radiol*. 2003; 33:850-854.
- Wen JG, Frøkjaer J, Jørgensen TM, Djurhuus JC. Obstructive nephropathy: An update of the experimental research. *Urol Res*. 1999; 27:29-39.
- Koff SA. Postnatal management of antenatal hydronephrosis using an observational approach. *Pediatric Urology*. 2000; 55:609-611.
- Laghi A, Catalano C, Assael FG, Panebianco V, Iannaccone R, Paolantonio P, Martino G, Passariello R. Diffusion-weighted echo-planar sequences for the evaluation of the upper abdomen: Technique optimization. *Radiol Med*. 2001; 101:213-218.
- Bammer R. Basic principles of diffusion-weighted imaging. *Eur J Radiol*. 2003; 45:169-184.
- Yamashita Y, Tang Y, Takahashi M. Ultrafast MR imaging of the abdomen: Echo planar imaging and diffusion-weighted imaging. *J Magn Reson Imaging*. 1998; 8:367-374.
- Taouli B, Vilgrain V, Dumont E, Daire JL, Fan B, Menu Y. Evaluation of liver diffusion isotropy and characterization of focal hepatic lesions with two single-shot echo-planar MR imaging sequences: Prospective study in 66 patients. *Radiology*. 2003; 226:71-78.
- Ichikawa T, Haradome H, Hachiya J, Nitatori T, Araki T. Diffusion-weighted MR imaging with a single-shot echo-planar sequence: Detection and characterization of focal hepatic lesions. *AJR*. 1998; 170:397-402.

(Received July 9, 2014; Revised October 22, 2014;
Accepted October 26, 2014)

Use of a mini-instrument in endoscopic thyroidectomy *via* a breast approach to improve cosmetic outcomes

Wei Zhang*, Chenpo Dang*, Chengxiang Shan, Sheng Liu, Zhiguo Jiang, Bin Wang, Ming Qiu**

Department of General Surgery, Changzheng Hospital affiliated with the Second Military Medical University, Shanghai, China.

Summary

The objective of this research was to evaluate the clinical benefits of using a mini-instrument during endoscopic thyroidectomy *via* a breast approach (ETBA). Surgery-related indices and cosmetic results were compared for 20 patients underwent ETBA with a mini-instrument (ETBA-m) and 20 patients who underwent standard ETBA (sETBA). Patients were closely matched in terms of age, gender, tumor size, and pathology. Patients who underwent sETBA had a significantly larger area of dissection and total length of incisions compared to patients who underwent ETBA-m ($136.25 \pm 19.22 \text{ cm}^2$ vs. $105.25 \pm 9.54 \text{ cm}^2$, $p < 0.001$ and $2.66 \pm 0.09 \text{ cm}$ vs. $2.08 \pm 0.24 \text{ cm}$, $p < 0.001$). All patients who underwent ETBA-m commented that they preferred their current cosmetic appearance after they were shown a picture of the scars of a patient who underwent sETBA. Results of this study revealed that use of a mini-instrument in ETBA is technically safe and feasible and it offers improved cosmetic outcomes compared to sETBA.

Keywords: Endoscopic, thyroidectomy, mini-instrument

1. Introduction

Thyroid disease has a particularly high incidence in women. Although conventional thyroidectomy is safe, effective, and well-tolerated, it results in an obvious cervical scar that compromises a patient's cosmetic appearance. Endoscopic thyroid surgery was developed to provide an aesthetically pleasing scar after open thyroidectomy (1,2).

Endoscopic thyroid surgery can be classified into video-assisted endoscopic and pure endoscopic surgery (3). The former requires only a small skin incision in the neck and limited tissue dissection, while the latter is performed remotely and involves extracervical incisions. Pure endoscopic surgery is popular in Asia since it yields superior cosmetic results. More than 20 "scarless" approaches for endoscopic thyroidectomy have been developed (4).

To further improve the cosmetic results of "scarless" endoscopic thyroidectomy (SET), some surgeons have attempted to reduce the number of incisions. Single-incision endoscopic thyroidectomy *via* an axillary approach was reported by Lee *et al.* (5) and similar surgery *via* a trans-areolar approach was reported by Fan *et al.* (6). Both groups of researchers found that single-incision endoscopic thyroidectomy was safe and technically feasible and offered an advantage in terms of the excellent cosmetic appearance of the thoracic wall. However, such procedures are technically difficult, they offer a singular view and more confined working space, and they carry the risk of instrument interference (5,6). Single-incision endoscopic thyroidectomy also takes a great deal of time and it involves a very steep learning curve.

Another way to improve cosmetic appearance is to reduce the size of an incision, as in mini-laparoscopic surgery. Mini-laparoscopic instruments are widely used in general surgery and gynecology (7-9) and can provide excellent cosmetic results without significantly altering the laparoscopic approach. However, such instruments have seldom been used in SET.

Reported here is experience using a mini-instrument in endoscopic thyroidectomy *via* a breast approach (ETBA), the most popular technique for SET in China.

*These authors contributed equally to this work.

**Address correspondence to:

Dr. Ming Qiu, Department of General Surgery, Changzheng Hospital affiliated with the Second Military Medical University, No.415 Fengyang Road, Shanghai 200003, China.
E-mail: qiuming2006@aliyun.com

The potential advantages of using mini-instruments are that first, the longest parasternal incision for the camera port can be moved to the areola, thus reducing the likelihood of hypertrophic scar formation at the parasternal incision. Second, a mini-incision will heal without leaving a mark, so the trocar for the mini-instrument can be inserted in the chest wall while maintaining the convenient triangular positioning of instruments. This rearrangement of trocar sites should not increase the procedure's technical difficulty and may improve cosmetic appearance afterwards.

2. Methods

2.1. Patient demographics

This study was approved by the Institutional Review Board of Changzheng Hospital. From September to December 2012, 20 consecutive patients (18 women, mean age: 34.7 ± 9.17 years) underwent ETBA with a mini-instrument (ETBA-m). Eligibility criteria were the same as for conventional ETBA: benign thyroid nodules (diameter < 5 cm) and papillary microcarcinoma diagnosed by preoperative ultrasound and fine needle aspiration cytology. Exclusion criteria were: a history of neck surgery or radiotherapy; thyroiditis diagnosed by preoperative biochemistry or ultrasound; liver dysfunction; and autoimmune disease (10,11). Twenty consecutive patients who underwent standard ETBA (sETBA) from June to September 2012 (17 women; mean age: 38.85 ± 9.95 years) served as the control group. All patients provided written informed consent prior to study participation.

2.2. Thyroidectomy

sETBA has been described previously (10,11). Briefly, three incisions were made: a 12-15-mm curved longitudinal parasternal incision for the camera port and two 5-mm working port incisions in the circumareolar region. Several tunnels were created with a plastic rod, and then a thyroidectomy was performed with a harmonic scalpel (HS, Ethicon Endo Surgery, Cincinnati, OH, USA). When exposure was difficult, a puncture was made in the skin of the neck and a suture retractor was inserted to pull the strap muscles laterally (12). Either a unilateral or a bilateral near-total or total lobectomy was performed depending on the size of benign tumors, and a hemi- or total thyroidectomy with central compartment node dissection (CCND) was performed for papillary microcarcinoma.

The location of trocars in ETBA-m differed from that in sETBA: a 10-mm optical trocar was inserted on the right areolar border and a 5-mm manipulation trocar for the HS was inserted along the left areolar border. A subcutaneous tunnel in the direction of the

neck was first created *via* a 10-mm incision, and a 5-mm trocar was inserted on the left to connect to the tunnel. A working space was created with the HS under endoscopic guidance. A 2-mm mini-instrument was inserted *via* the chest wall, maintaining a wide angle for extensive manipulation and facilitating exposure with the surgeon's left hand (Figures 1A and 1B). The rest of the procedure was the same as that for sETBA (Figures 1C and 1D). Even though the view is lateral, resection of either lobe is no more difficult than in sETBA. If, however, central compartment dissection is necessary, then the sternal portion of the clavicle and the lower right strap muscle may hinder visualization. Thus, the strap muscles were usually transected in part for better exposure.

2.3. Collection of surgery-related data

The diameter of thyroid lesions as determined by ultrasound, pathologic diagnosis, operating time, extent of the subcutaneous area marked with endoscopic illumination, blood loss, and total incision length were recorded and compared.

2.4. Subjective assessment of postoperative pain

Postoperative pain was assessed 12, 24, and 48 h after surgery using a visual analog scale (VAS) from 0-10 ("0" = "no pain," "10" = "worst pain imaginable") (10,13).

2.5. Monitoring of complications

Blood samples were collected to measure calcium levels on day 1 postoperatively. Hypocalcemia was diagnosed depending on symptoms and laboratory findings. Patients who presented with postoperative hoarseness underwent laryngoscopy. Transient hypocalcemia and transient recurrent laryngeal nerve (RLN) injury were defined based on recovery from symptoms and normalization of laboratory data within 6 months (10,14).

2.6. Evaluation of cosmetic results

Three months postoperatively, patients evaluated their cosmetic outcomes using a numerical scoring system (NSS) similar to VAS ("0" = "extreme dissatisfaction", "10" = "extreme satisfaction") (10). Patients who underwent ETBA-m were also shown a picture of scars following sETBA and their comments were recorded.

2.7. Statistical analysis

The student's *t*-test and the Pearson χ^2 test were used to compare means and categorical variables, respectively. A *p* value of less than 0.05 was considered to be statistically significant.

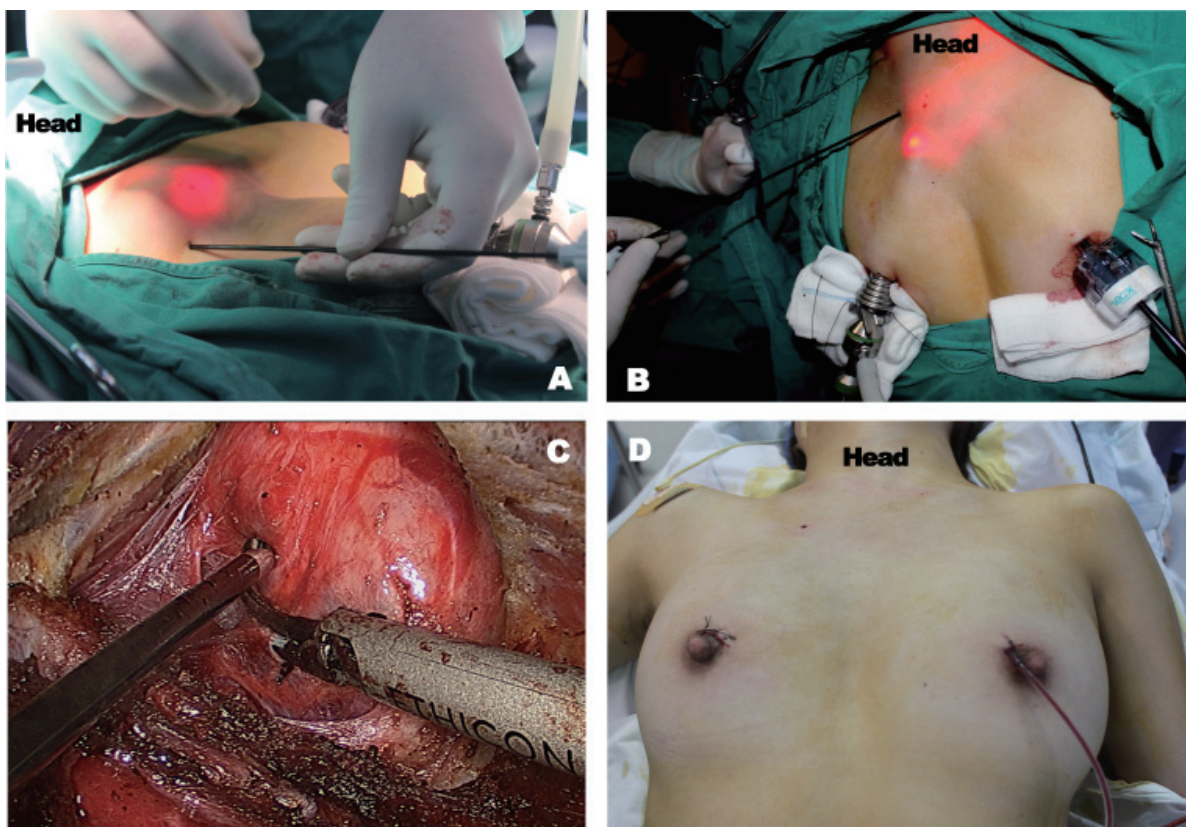


Figure 1. Surgical procedure for ETBA-m. **A:** A 2-mm mini-instrument was inserted in the chest wall; **B:** A wide angle was maintained for extensive manipulation; **C:** A thyroidectomy was performed with the mini-instrument facilitating exposure, and **D:** Surgical sites once the surgery was completed.

Table 1. Baseline data of patients underwent BAET

Items	sBAET group	mBAET group	p value
Gender (male/female)	3/17	2/18	1.000
Age(y)	38.85 ± 9.95	34.70 ± 9.00	0.175
Tumor size (mm)			
benign	29.50 ± 10.27	31.39 ± 8.65	0.623
Cancer	6.88 ± 2.17	7.29 ± 1.50	0.681
Lateral (uni/bilateral)	13/7	11/9	0.519
Pathology (adenoma/goiter/cancer)	11/3/6	13/2/5	0.795

3. Results

3.1. Baseline data

The two groups were closely matched in terms of age, gender, tumor size, and pathology, as shown in Table 1

3.2. Surgical outcomes

The surgical procedures for patients who underwent ETBA-m were a lobectomy for 7 patients, hemithyroidectomy with CCND for 4, sub-total thyroidectomy for 5, total thyroidectomy (TT) for 3, and TT with CCND for 1.

There were no deaths or conversion to another procedure for either group. There were no significant

differences in blood loss and operating time for the two groups. The location of trocars was altered since the shape of the area of subcutaneous dissection was changed from a rhomboid shape to an upside-down Y shape. Thus, the area of dissection decreased significantly from $136.25 \pm 19.22 \text{ cm}^2$ in patients who underwent sETBA to $105.25 \pm 9.54 \text{ cm}^2$ in patients who underwent ETBA-m ($p < 0.001$). Use of the mini-instrument also significantly shortened the total length of incisions ($2.66 \pm 0.09 \text{ cm}$ vs. $2.08 \pm 0.24 \text{ cm}$, $p < 0.001$, Table 2).

There was one case of RLN palsy in each group, and both resolved within 3 months. Transient hypocalcemia occurred in 3 patients who underwent ETBA-m and in 2 patients who underwent sETBA. Hypercapnia, subcutaneous emphysema, and seroma were not observed in either group.

Table 2. Surgery-related data of patients underwent BAET

Items	sBAET group	mBAET group	<i>p</i> value
Dissection area (cm ²)	136.25 ± 19.22	105.25 ± 9.54	<0.001
Incision length (cm)	2.66 ± 0.09	2.08 ± 0.24	<0.001
Blood loss (mL)	6.85 ± 2.08	6.65 ± 3.63	0.832
Surgery duration (min)	105.75 ± 20.02	113.75 ± 41.51	0.442
VAS-12h	3.45 ± 1.57	2.55 ± 1.19	0.048
VAS-24h	1.75 ± 1.41	0.95 ± 0.76	0.031
VAS-48h	0.75 ± 1.41	0.30 ± 0.47	0.184
Drainage volume (mL)	120.75 ± 38.12	113.75 ± 41.51	0.442
NSS	8.75 ± 1.21	9.30 ± 1.21	0.090

**Figure 2. Cosmetic outcomes of ETBA. A:** Surgical scars following ETBA-m and **B:** Surgical scars following sETBA.

3.3. Postoperative pain

The severity of pain according to the VAS differed significantly 12 and 24 h postoperatively but did not differ significantly 48 hours postoperatively for either group.

3.4. Cosmetic outcomes

The areolar incisions blended well with the areola, and the mini-incision on the chest wall left no obvious trace (Figure 2A). Although the patients who underwent ETBA-m had a higher NSS score than patients who underwent sETBA, the difference was not statistically significant. However, all patients who underwent ETBA-m commented that they preferred their incisions after they were shown a picture of scars of a patient who underwent sETBA (Figure 2 B).

4. Discussion

Use of a mini-instrument in endoscopic thyroidectomy has the advantages as mini-laparoscopic surgery, yielding the same surgical results after minor technical adjustments (15). Some technical pitfalls have been encountered when mini-instruments were used for complex procedures, such as antireflux surgery (15). This is not a problem in ETBA-m since the surgeon only used the mini-instrument in his left hand to

facilitate exposure. A new learning curve is not required, as the triangular positioning of instruments is maintained. This was evident in the absence of a significant difference in the operating time for either group. This is despite the fact that ETBA-m was performed for the first time during this study and sETBA has been performed more than 700 times by the current authors. That said, ETBA-m involved unilateral lobectomy for adenoma as well as TT with CCND for bilateral papillary microcarcinoma. There was also no difference in the incidence of RLN palsy and hypocalcaemia in the groups, and this incidence was within the range reported in literature (2,16-18). Thus, clinical use of mini-instruments is feasible and yields consistent results (7,8).

Breast and axillary approaches to endoscopic thyroidectomy (ETAA) were both developed by Asian surgeons (19,20). ETBA has an advantage over ETAA in terms of a wide triangular positioning of instruments so they do not interfere with one another (21), and ETBA offers excellent visualization when approaching bilateral lesions. Thus, ETBA is the most popular approach for endoscopic thyroidectomy in China (22). However, ETBA is inferior in terms of cosmetics as it may leave a hypertrophic parasternal scar (21,23). To resolve this issue, the breast and axillary approaches were combined, including the bilateral axillo-breast approach (BABA) (24), axillo-bilateral breast approach (ABBA) (25) and bilateral breast areola and ipsilateral

axillary approach (BBIA) (3). These techniques do not provide an optimal solution since the axillary scar can be rather prominent and it compromises a patient's cosmetic appearance, especially for young women who wear sleeveless clothing (23).

Hur *et al.* (23) developed a bilateral areolar approach (BAA) to endoscopic thyroidectomy, offering an advantage of an excellent cosmetic appearance compared to other approaches, including BABA. ETBA with the mini-instrument results in a scar with an almost identical appearance since the 2-mm minilaparoscopic incision was no longer evident during the follow-up 3 months postoperatively. The NSS score did not differ significantly for patients who underwent the ETBA-m and those who underwent the sETBA, but all of the patients who underwent ETBA-m felt that endoscopic thyroidectomy with a mini-instrument yielded a better cosmetic appearance after viewing a picture of the scars of a patient who underwent sETBA. The current approach has several advantages over BAA. First, only 3 incisions are required. Second, total incision length can be reduced (22 mm vs. 26 mm). Third, instruments were positioned in a triangular shape with larger angles, so instruments did not interfere with one another.

Proponents of BAA argue that the approach is minimally invasive (23). Although patients who underwent ETBA-m had significantly less postoperative pain than those who underwent sETBA 12 and 24 h postoperatively, one cannot rationally conclude that ETBA-m is superior, as personal bias may be involved (26). However, ETBA-m has the potential to reduce invasiveness in terms of total incision length (2.66 ± 0.09 cm vs. 2.08 ± 0.24 cm, $p < 0.001$) and the lack of a parasternal incision (the triangle-shaped area between the nipples does not need to be dissected, reducing the area of subcutaneous dissection; 136.25 ± 19.22 cm 2 vs. 105.25 ± 9.54 cm 2 , $p < 0.001$). Additional research is necessary to provide a more comprehensive evaluation.

In conclusion, use of a mini-instrument in ETBA is technically safe and feasible and it offers improved cosmetic outcomes compared to sETBA while also reducing invasiveness in terms of incision length and subcutaneous dissection.

References

- Hüscher CS, Chiodini S, Napolitano C, Recher A. Endoscopic right thyroid lobectomy. *Surg Endosc*. 1997; 11:877.
- Tan CT, Cheah WK, Delbridge L. "Scarless" (in the neck) endoscopic thyroidectomy (SET): An evidence-based review of published techniques. *World J Surg*. 2008; 32:1349-1357.
- Jeryong K, Jinsun L, Hyegyong K, Eilsung C, Jiyoung S, Insang S, Moonsang A, Jiyeon K, Jaeeun H. Total endoscopic thyroidectomy with bilateral breast areola and ipsilateral axillary (BBIA) approach. *World J Surg*. 2008; 32:2488-2493.
- Schardey HM, Schopf S, Kammal M, Barone M, Rudert W, Hernandez-Richter T, Pörtl S. Invisible scar endoscopic thyroidectomy by the dorsal approach: Experimental development of a new technique with human cadavers and preliminary clinical results. *Surg Endosc*. 2008; 22:813-820.
- Lee D, Nam Y, Sung K. Single-incision endoscopic thyroidectomy by the axillary approach. *Laparoendosc Adv Surg Tech A*. 2010; 20:839-842.
- Fan YB, Wu B, Zhong CL, Kang J, Guo BM, Yang F, Deng XZ, Zheng Q. Trans-areola single-site endoscopic thyroidectomy: Pilot study of 35 cases. *Surg Endosc*. 2012; 26:939-947.
- Bona S, Molteni M, Montorsi M. Minilaparoscopic colorectal resections: Technical note. *Minim Invasive Surg*. 2012; 2012:482079.
- Di Lorenzo N, Manzelli A, Coscarella G, Pietrantuono M, Jarzemowski TM, Fisichella PM, Gaspari AL. Minilaparoscopic appendectomy for acute appendicitis. *JSLS*. 2006; 10:52-55.
- Wattiez A, Goldchmit R, Durruty G, Mage G, Canis M, Cucinella G, Pouly JL, Bruhat MA. Minilaparoscopic hysterectomy. *J Am Assoc Gynecol Laparosc*. 1999; 6:97-100.
- Jiang ZG, Zhang W, Jiang DZ, Zheng XM, Shen HL, Shan CX, Liu S, Qiu M. Clinical benefits of scarless endoscopic thyroidectomy: An expert's experience. *World J Surg*. 2011; 35:553-557.
- Liu S, Qiu M, Jiang DZ, Zheng XM, Zhang W, Shen HL, Shan CX. The learning curve for endoscopic thyroidectomy: A single surgeon's experience. *Surg Endosc*. 2009; 23:1802180-1802186.
- Liu S, Zheng XM, Jiang DZ, Zhang W, Shan CX, Qiu M. New technique for retraction of the strap muscles in endoscopic thyroidectomy. *Surg Innov*. 2011; 18:141-144.
- Perigli G, Cortesini C, Qirici E, Boni D, Cianchi F. Clinical benefits of minimally invasive techniques in thyroid surgery. *World J Surg*. 2008; 32:45-50.
- Jeong JJ, Kang SW, Yun JS, Sung TY, Lee SC, Lee YS, Nam KH, Chang HS, Chung WY, Park CS. Comparative study of endoscopic thyroidectomy versus conventional open thyroidectomy in papillary thyroid microcarcinoma (PTMC) patients. *J Surg Oncol*. 2009; 100:477-480.
- Dimbarre D, de Loureiro PM, Claus C, Carvalho G, Trauczynski P, Elias F. Minilaparoscopic fundoplication: Technical adaptations and initial experience. *Arq Gastroenterol*. 2012; 49:223-226.
- Cao F, Jin K, Cui B, Xie B. Learning curve for endoscopic thyroidectomy: A single teaching hospital study. *Onco Targets Ther*. 2013; 6:47-52.
- Zhou J, Wu Z, Wang Y, Peng B. Endoscopic thyroidectomy for bilateral thyroid diseases: Safety and effectiveness. *J Craniofac Surg*. 2012; 23:565-570.
- Chen B, Wang Y, Xuan S, Zhang G, Hu S, Wachtel MS, Frezza EE. Endoscopic thyroidectomy: The development in a Chinese center. *J Laparoendosc Adv Surg Tech A*. 2012; 22:76-80.
- Ikeda Y, Takami H, Sasaki Y, Kan S, Niimi M. Endoscopic neck surgery by the axillary approach. *J Am Coll Surg*. 2000; 191:336-340.
- Ohgami M, Ishii S, Arisawa Y, Ohmori T, Noga K, Furukawa T, Kitajima M. Scarless endoscopic thyroidectomy: Breast approach for better cosmesis. *Surg Laparosc Endosc Percutan Tech*. 2000; 10:1-4.

21. Choe JH, Kim SW, Chung KW, Park KS, Han W, Noh DY, Oh SK, Youn YK. Endoscopic thyroidectomy using a new bilateral axillo-breast approach. *World J Surg.* 2007; 31:601-606.
22. Zhang W, Jiang DZ, Liu S, Li LJ, Zheng XM, Shen HL, Shan CX, Qiu M. Current status of endoscopic thyroid surgery in China. *Surg Laparosc Endosc Percutan Tech.* 2011; 21:67-71.
23. Hur SM, Kim SH, Lee SK, Kim WW, Choe JH, Lee JE, Kim JH, Nam SJ, Yang JH, Kim JS. New endoscopic thyroidectomy with the bilateral areolar approach: A comparison with the bilateral axillo-breast approach. *Surg Laparosc Endosc Percutan Tech.* 2011; 21:e219-224.
24. Choi JY, Lee KE, Chung KW, Kim SW, Choe JH, Koo do H, Kim SJ, Lee J, Chung YS, Oh SK, Youn YK. Endoscopic thyroidectomy via bilateral axillo-breast approach (BABA): Review of 512 cases in a single institute. *Surg Endosc.* 2012; 26:948-955.
25. Bärlehner E, Benhidjeb T. Cervical scarless endoscopic thyroidectomy: Axillo-bilateral-breast approach (ABBA). *Surg Endosc.* 2008; 22:154-157.
26. Sasaki A, Nakajima J, Ikeda K, Otsuka K, Koeda K, Wakabayashi G. Endoscopic thyroidectomy by the breast approach: A single institution's 9-year experience. *World J Surg.* 2008; 32:381-385.

(Received April 14, 2014; Revised October 10, 2014; October 11, 2014)

Revisiting Einstein's brain in Brain Awareness Week

Hao Chen, Su Chen, Lidan Zeng, Lin Zhou, Shengtao Hou*

Department of Biology, South University of Science and Technology of China, Shenzhen, China.

Summary

Albert Einstein's brain has long been an object of fascination to both neuroscience specialists and the general public. However, without records of advanced neuro-imaging of his brain, conclusions regarding Einstein's extraordinary cognitive capabilities can only be drawn based on the unique external features of his brain and through comparison of the external features with those of other human brain samples. The recent discovery of 14 previously unpublished photographs of Einstein's brain taken at unconventional angles by Dr. Thomas Stoltz Harvey, the pathologist, ignited a renewed frenzy about clues to explain Einstein's genius. Dr. Dean Falk and her colleagues, in their landmark paper published in *Brain* (2013; 136:1304-1327), described in such details about the unusual features of Einstein's brain, which shed new light on Einstein's intelligence. In this article, we ask what are the unique structures of his brain? What can we learn from this new information? Can we really explain his extraordinary cognitive capabilities based on these unique brain structures? We conclude that studying the brain of a remarkable person like Albert Einstein indeed provides us a better example to comprehensively appreciate the relationship between brain structures and advanced cognitive functions. However, caution must be exercised so as not to over-interpret his intelligence solely based on the understanding of the surface structures of his brain.

Keywords: Albert Einstein's brain, cerebral cortex, cognitive function, Thomas Stoltz Harvey, brain photography

1. Introduction

This March, as we celebrate the achievements made in neuroscience and raise awareness of brain health in our communities around the world, it is fitting to revisit one of the most fascinating brains on earth, that of Albert Einstein - the brain of a true genius. As a group of science students, we are fascinated by what is under his brain, a finite boundless spherical universe. In particular, we are drawn to a recent study of the cerebral cortex of Albert Einstein based on newly discovered, previously unpublished photographs of Einstein's brain (1). What is unique about the structures of his brain? What can we learn from this new information? Can we explain his extraordinary cognitive capabilities based

on his unique brain structures? These are just a few of the questions we will focus on in this short review article.

To gain a better understanding of the cognitive functions related to the structures of Einstein's brain, we collected and critically reviewed all published papers describing Einstein's brain, including a recent report by Falk and her colleagues (1). A battery of unusual external features of Einstein's cerebral cortex is discussed in the paper. A comparison of these features with known human brain structures reported in the literature revealed several interesting features of Einstein's brain previously unknown to us.

After Einstein's death in 1955, his brain was carefully dissected, photographed and preserved by Princeton Hospital pathologist Dr. Thomas Stoltz Harvey. Dr. Harvey cut the brain into 240 pieces; some were sent to researchers for examination. Efforts were made to identify unusual anatomical features in particular on the cerebral cortex to account for Einstein's genius (2-5). It is only until recently a detailed description of the surface anatomy of the entire

*Address correspondence to:

Dr. Shengtao Hou, Department of Biology, South University of Science and Technology of China, 1088 Xueyuan Blvd, Xili University Town, Nanshan District, Shenzhen 518055, China.

E-mail: hou.st@sustc.edu.cn

cerebral cortex of Einstein's brain was reported by Dr. Falk and colleagues (1). New findings were revealed in this study based on 14 previously unpublished photographs taken by Dr. Harvey. Importantly, these photos were apparently taken at unconventional angles, which showed unusual morphological features when compared with the external features of other 85 human brain samples described in previous studies by Connolly (1950) (6) and Ono *et al.* (1990) (7). All external surfaces of the cerebral cortex, the medial surface of each hemisphere and the insula of the right hemisphere were imaged on these photographs. New surface sulci of Einstein's cerebral cortex were identified and a road map to the 240 blocks of brain sections was provided for future investigators. Although limited by the information available on the photographs, the unusual features of Einstein's brain are good indications of extraordinary cognitive capabilities based on our current understanding of cognitive process of humans.

2. What is unique about the structures of his brain?

Based on the descriptions by Falk *et al.*, (2013) (1), a summary of the unusual anatomical features of Einstein's cerebral cortex is listed below.

2.1. The frontal lobes

- i). A large 'knob'-shaped fold in the right hemisphere representing enlarged motor cortex area for the left hand;
- ii). The pre-central superior sulcus is continuous with the pre-central inferior sulcus in both hemispheres, forming a long, continues sulcus. The pre-central inferior sulcus terminates extraordinarily high above the Sylvian fissure in the left, but not the right, hemisphere. Diagonal sulcus exists in both hemispheres;
- iii). The presence of unusually long and continuous mid-frontal sulcus on the right hemisphere which divides the middle frontal region into two distinct gyri, giving rise to four frontal gyri rather than the typical three gyri;
- iv). A long, branched inferior frontal sulcus and an additional triangular sulcus in the left hemisphere, which are located in the pars triangularis;
- v). The caudal segment of the inferior frontal sulcus is connected with both the diagonal sulcus and the pre-central inferior sulcus in the left hemisphere.

2.2. The parietal lobes

- i). Morphological features suggest expanded primary sensory and motor representations of face and tongue in the left hemisphere;
- ii). The left Sylvian fissure is separated from the postcentral inferior sulcus by a submerged gyrus;

- iii). A significantly larger volume of grey matter in the angular gyrus in the left hemisphere than that in the right hemisphere;
- iv). The left superior parietal lobule is separated from the inferior parietal lobule by a continue sulcus in the left hemisphere, while the two lobules are separated by two parallel sulcus in the right hemisphere;
- v). The united segments of the intraparietal sulcus on the right side course upward into the superior parietal lobule, rather than along its inferior border.

2.3. The temporal lobes

- i). Expanded superior surface of the posterior part on the left side than on the right;
- ii). Collateral sulcus is divided into two separate segments in the left hemisphere.

2.4. The occipital lobes

- i). The anterior occipital sulcus in both hemisphere are relatively caudal, which might be caused by expansion of inferior parietal lobules;
- ii). A separate medial segment of the transverse occipital sulcus on the left hemisphere that crosses its superior margin;
- iii). A relatively large additional transverse occipital sulcus in the right hemisphere (This variation is not included in articles by Ono (1990) (7) and Connolly (1950) (6)).
- iv). Presence of four transverse occipital sulci;
- v). Relatively large additional transverse occipital sulcus in the right hemisphere, indicating relatively wide occipital lobes near their dorsal rostral borders.

2.5. The medial and internal surfaces of the brain

- i). The marginal sulcus ends at the superior medial border instead of extending on the dorsolateral surface of the brain on the medial surface of the left hemisphere;
- ii). There are four inferiorly directed branches of cingulate sulcus on the left hemisphere and unnamed sulci in the middle of cingulate gyri in both hemispheres, indicating that the cingulate gyri may have been relatively convoluted;
- iii). No limb of the H-shaped subparietal sulcus crosses the superior margin of the right hemisphere;
- iv). The cuneus of the left hemisphere are relatively ramified, containing inferior and superior sagittal sulci;
- v). The superior sagittal sulcus and the parieto-occipital sulcus are connected in the left hemisphere;
- vi). In both hemispheres, parieto-occipital incisures are distinct from each other and just caudal to the

limiting sulcus of the precuneus. The cunei are found unusually convoluted.

2.6. Patalia pattern

The left occipital lobe is lower, wider towards the posterior end than the right occipital lobe. The right frontal lobe is wider in the anterior end than the left frontal lobe. These features contribute greatly to the asymmetry of Einstein's brain.

3. What can we learn from this new information?

The highly advanced cognitive abilities in humans have been attributed to an evolutionary increase in both the overall brain size (8) and neurological reorganization (9) manifested by an asymmetry of the cerebral hemispheres and some of their subareas (10,11). Although there is no evidence to suggest Albert Einstein's brain is exceptional in size (2), the external neuroanatomic features of his cerebral cortex involved in specific higher cognitive functions appear to be especially marked.

The following lists important features. For example, the convoluted Broca's speech area of his brain can be interpreted as having higher speech abilities. The enlarged 'knob' in the right primary motor cortex corresponds to the left hand, which may attribute to Einstein's early extensive violin training (12). The expanded lower parts of the primary sensory and motor cortices in the left hemisphere indicate enhanced sensory of the face and tongue (5,13). The relatively expanded left inferior parietal lobule suggests relatively great skills on language, body image and mathematics. In particular, the expanded left angular gyrus facilitates the recognition of visual symbols and sensory language (1). Einstein's right superior parietal lobule may be larger comparing with the left, which are thought to be involved in certain aspects of visuospatial imagery (14). The convoluted medial surfaces of the occipital lobes including primary visual area BA 17 as well as associated visual areas BA 18 and BA 19 may be significant during processing visual information (15,16). The inferior temporal gyrus is relatively expanded on the basal surface of each hemisphere, which can be interpreted as having better developed high-level processing capabilities associated with remembering, recognizing and naming of visual objects and forms (1). The medial surfaces manifest larger frontopolar region, especially for anterior cingulate cortex, which gives implications about neurological substrate for the enhanced ability in handling conflicting impulses needed in self-regulating behavior (17).

Despite of the details provided based on the photographs, it is possible that some of the descriptions are not accurate due to the fact that analysis was based only on old monochrome photographs rather than the real brain. Possibility exists that the cortical convolution was actually not as exaggerated as described. Indeed, this

kind of mistake occurred before. For example, earlier studies regarded Einstein's posterior ascending limb of the Sylvian fissure as confluent with the postcentral inferior sulcus based on the photographs (2). However, new photographs taken from another angle revealed that the two sulci (fissure) were, in fact, separate (1). Therefore, caution must be taken when conclusions are drawn from these photographs.

Many unusual features of Einstein's brain were identified based on the comparison of Einstein's brain with descriptions provided in two previous studies of 60 (6) and 25 (7) human brains. Because these two studies did not provide accurate records of the brain samples in terms of race, age and sex, etc., the reliability of the identified "unusual features" of Einstein's brain is limited and depends on the accuracy of the two reports. For example, in the study of Connolly *et al.* (1950) (6), half of the brains were from white Germans; the other half were from black Americans. Sample sex, but not age, was reported. In the study of Ono *et al.* (1990) (7), most of the specimens were assumed to be Europeans with age and sex unknown. It is obviously necessary and ideal to match factors such as race, sex and age when comparing brain structures, which may lead to the identification of more unusual features and elimination of possible artifacts.

One of the pictures revealed that Einstein's left Sylvian fissure was non-confluent with the postcentral inferior sulcus and it was suggested that the right hemisphere was also the same, assuming from the similar external sulcal patterns of the surrounding region. This assumption may be unreliable as the layout pattern of the cerebral cortex is asymmetric which makes it rather difficult to predict features of the opposite hemisphere.

4. Can we explain his extraordinary cognitive capabilities based on his unique brain structures?

Einstein has extraordinary cognitive abilities including maintaining attention, performing visuospatial tasks and mathematical thinking, which facilitate his thought experiments (1). The anatomical basis might lie in the pattern of Einstein's prefrontal cortex including the anterior portion of the frontal lobes (BA10). The prefrontal cortex is critical for a group of high-level cognitive processes including working memory, reasoning, task flexibility, and problem solving as well as planning and execution (18,19). In Einstein's case, his cortex appears to be highly convoluted in both hemispheres, which may explain his remarkable cognitive strength.

However, more convoluted brain areas may not necessarily correlate with enhanced cognitive functions. For example, the unusually convoluted Broca's area, relatively expanded left inferior parietal lobule and expanded interior parts of Einstein's left primary somatosensory area, and the left primary motor cortices

representing face and tongue are considered to be involved in language skills, especially speech abilities (1). But we did not find sufficient evidence suggesting that Einstein exhibited extraordinary abilities in such things. In fact, Einstein is an introvert and probably not a good speaker (20).

How to tease out brain structural changes due to "nature", but not "nurture", is another difficult issue when trying to interpret Einstein's genius based on his final brain structures. For example, a large 'knob'-shaped fold representing the left hand in the motor cortex of Einstein's right hemisphere can probably be attributed to long time violin training during Einstein's early age. This unusual feature has been seen in some long-time right-handed violinists. A study by Hyde *et al.*(2009) (21) has shown that brain structure changes in the frontal, temporal and parieto-occipital lobes in children around the age of six after 15 months of keyboard training (21). Another study by Christian Gaser demonstrated that gray matter volume increased in the brains of musicians (22). This type of alteration of brain structures due to "nature" has also been reported in animals. For instance, the primary somatosensory area of raccoon's forepaw used for exploring the environment is greatly enlarged and the areas controlling the palm pad and digit area in the forepaw are also separated by sulci (23). It is not possible at this stage to determine if some of Einstein's unusual brain structures were in fact "nature", or "nurture".

It is also worth noting that in addition to external brain morphology, other factors, such as cortical thickness, neuronal density, the neuron to glia ratio, and brain chemicals, those also play important parts in a person's mental activities. These information is obviously not available to us, which make it very difficult to fully understand Einstein's brain. Furthermore, we must not over interpret Einstein's brain. Because interpretation bias occurs when people are constantly aware that they are looking at the famous Einstein's brain rather than a brain of unknown identity. In psychology, this is termed as observer-expectancy effect, in which the observer is unconsciously affected by the expectation of certain results (24). Such a bias can be controlled with a blinded experimental design approach. It is necessary to choose observers who are not aware of the identity of the brain samples and to derive at their conclusions independently.

References

1. Falk D, Lepore FE, Noe A. The cerebral cortex of Albert Einstein: A description and preliminary analysis of unpublished photographs. *Brain*. 2013; 136:1304-1327.
2. Witelson SF, Kigar DL, Harvey T. The exceptional brain of Albert Einstein. *Lancet*. 1999; 353:2149-2153.
3. Yuan TF. Einstein's brain: Gliogenesis in autism? *Med Hypotheses*. 2009; 72:753-761.

4. Marian C, Diamond AB, Scheibel GM, Murphy JR, Harvey T. On the Brain of a Scientist: Albert Einstein. *Exp Neurol*. 1985; 88:198-204.
5. Falk D. New Information about Albert Einstein's Brain. *Front Evol Neurosci*. 2009; 1:3.
6. Connolly JC. External morphology of the primate brain (Thomas CC, ed.). Springfield, IL, USA, 1950; pp. 1-378.
7. Ono M, Kubik S, Abernathy CD. *Atlas of the Cerebral Sulci*. Thieme Medical Publishers, Inc., New York, USA, 1990.
8. Finlay BL., and Darlington RB. Linked regularities in the development and evolution of mammalian brains. *Science*. 1995; 268:1578-1584.
9. Teffer K, Semendeferi K. Human prefrontal cortex: Evolution, development, and pathology. *Prog Brain Res*. 2012; 195:191-218.
10. Galaburda AM, Geschwind N. Anatomical asymmetries in the adult and developing brain and their implications for function. *Adv Pediatr*. 1981; 28:271-292.
11. Galaburda AM, LeMay M, Kemper TL. Right-left asymmetries in the brain. *Science* 1978; 199:852-856.
12. Bangert M, Schlaug G. Specialization of the specialized in features of external human brain morphology. *Eur J Neurosci*. 2006; 24:1832-1834.
13. Penfield M, Rasmussen T. *The Cerebral Cortex of Man: A Clinical Study of Localization of Function*. Hafner Publishing Company, New York, USA. 1968.
14. Sack AT, Sperling JM, Prvulovic D, Formisano E, Goebel R, Di Salle F, Dierks T, Linden DE. Tracking the mind's image in the brain II: Transcranial magnetic stimulation reveals parietal asymmetry in visuospatial imagery. *Neuron*. 2002; 35:195-204.
15. Kosslyn SM, Ganis G, Thompson WL. Neural foundations of imagery. *Nat Rev Neurosci*. 2001; 2:635-642.
16. Kosslyn SM, Thompson WL, Kim IJ, Alpert NM. Topographical representations of mental images in primary visual cortex. *Nature*. 1995; 378:496-498.
17. Posner MI, Rothbart MK, Sheese BE, Tang Y. The anterior cingulate gyrus and the mechanism of self-regulation. *Cogn Affect Behav Neurosci*. 2007; 7:391-395.
18. Monsell S. Task switching. *Trends Cogn Sci*. 2003; 7:134-140.
19. Wilson CR, Gaffan D, Browning PG, Baxter MG. Functional localization within the prefrontal cortex: Missing the forest for the trees? *Trends Neurosci*. 2010; 33:533-540.
20. Isaacson W. *Einstein: His Life and Universe*. Simon & Schuster Audio, New York, USA, 2011.
21. Hyde KL, Lerch J, Norton A, Forgeard M, Winner E, Evans AC, Schlaug G. Musical training shapes structural brain development. *J Neurosci*. 2009; 29:3019-3025.
22. Gaser C, Schlaug G. Brain structures differ between musicians and non-musicians. *J Neurosci*. 2003; 23:9240-9245.
23. Welker WI, Campos GB. Physiological significance of sulci in somatic sensory cerebral cortex in mammals of the family procyonidae. *J Comp Neurol*. 1963; 120:19-12036.
24. Rosenthal R. *Experimenter effects in behavioral research*. Appleton-Century-Crofts, East Norwalk, CT, USA, 1966; pp. 1-464.

(Received March 31, 2014; Revised June 10, 2014; Re-revised October 17, 2014; Accepted October 17, 2014)

Guide for Authors

1. Scope of Articles

BioScience Trends is an international peer-reviewed journal. BioScience Trends devotes to publishing the latest and most exciting advances in scientific research. Articles cover fields of life science such as biochemistry, molecular biology, clinical research, public health, medical care system, and social science in order to encourage cooperation and exchange among scientists and clinical researchers.

2. Submission Types

Original Articles should be well-documented, novel, and significant to the field as a whole. An Original Article should be arranged into the following sections: Title page, Abstract, Introduction, Materials and Methods, Results, Discussion, Acknowledgments, and References. Original articles should not exceed 5,000 words in length (excluding references) and should be limited to a maximum of 50 references. Articles may contain a maximum of 10 figures and/or tables.

Brief Reports definitively documenting either experimental results or informative clinical observations will be considered for publication in this category. Brief Reports are not intended for publication of incomplete or preliminary findings. Brief Reports should not exceed 3,000 words in length (excluding references) and should be limited to a maximum of 4 figures and/or tables and 30 references. A Brief Report contains the same sections as an Original Article, but the Results and Discussion sections should be combined.

Reviews should present a full and up-to-date account of recent developments within an area of research. Normally, reviews should not exceed 8,000 words in length (excluding references) and should be limited to a maximum of 100 references. Mini reviews are also accepted.

Policy Forum articles discuss research and policy issues in areas related to life science such as public health, the medical care system, and social science and may address governmental issues at district, national, and international levels of discourse. Policy Forum articles should not exceed 2,000 words in length (excluding references).

Case Reports should be detailed reports of the symptoms, signs, diagnosis, treatment, and follow-up of an individual patient. Case reports may contain a demographic profile of the patient but usually describe an unusual or novel occurrence. Unreported or unusual

side effects or adverse interactions involving medications will also be considered. Case Reports should not exceed 3,000 words in length (excluding references).

News articles should report the latest events in health sciences and medical research from around the world. News should not exceed 500 words in length.

Letters should present considered opinions in response to articles published in BioScience Trends in the last 6 months or issues of general interest. Letters should not exceed 800 words in length and may contain a maximum of 10 references.

3. Editorial Policies

Ethics: BioScience Trends requires that authors of reports of investigations in humans or animals indicate that those studies were formally approved by a relevant ethics committee or review board.

Conflict of Interest: All authors are required to disclose any actual or potential conflict of interest including financial interests or relationships with other people or organizations that might raise questions of bias in the work reported. If no conflict of interest exists for each author, please state "There is no conflict of interest to disclose".

Submission Declaration: When a manuscript is considered for submission to BioScience Trends, the authors should confirm that 1) no part of this manuscript is currently under consideration for publication elsewhere; 2) this manuscript does not contain the same information in whole or in part as manuscripts that have been published, accepted, or are under review elsewhere, except in the form of an abstract, a letter to the editor, or part of a published lecture or academic thesis; 3) authorization for publication has been obtained from the authors' employer or institution; and 4) all contributing authors have agreed to submit this manuscript.

Cover Letter: The manuscript must be accompanied by a cover letter signed by the corresponding author on behalf of all authors. The letter should indicate the basic findings of the work and their significance. The letter should also include a statement affirming that all authors concur with the submission and that the material submitted for publication has not been published previously or is not under consideration for publication elsewhere. The cover letter should be submitted in PDF format. For example of Cover Letter, please visit <http://www.biostencetrends.com/downncentre.php> ([Download Centre](#)).

Copyright: A signed JOURNAL PUBLISHING AGREEMENT (JPA) form must be provided by post, fax, or as a scanned file before acceptance of the article. Only forms with a hand-written signature are accepted. This copyright will ensure the widest possible dissemination of information. A form facilitating transfer of copyright can be downloaded by clicking the

appropriate link and can be returned to the e-mail address or fax number noted on the form (Please visit [Download Centre](#)). Please note that your manuscript will not proceed to the next step in publication until the JPA Form is received. In addition, if excerpts from other copyrighted works are included, the author(s) must obtain written permission from the copyright owners and credit the source(s) in the article.

Suggested Reviewers: A list of up to 3 reviewers who are qualified to assess the scientific merit of the study is welcomed. Reviewer information including names, affiliations, addresses, and e-mail should be provided at the same time the manuscript is submitted online. Please do not suggest reviewers with known conflicts of interest, including participants or anyone with a stake in the proposed research; anyone from the same institution; former students, advisors, or research collaborators (within the last three years); or close personal contacts. Please note that the Editor-in-Chief may accept one or more of the proposed reviewers or may request a review by other qualified persons.

Language Editing: Manuscripts prepared by authors whose native language is not English should have their work proofread by a native English speaker before submission. If not, this might delay the publication of your manuscript in BioScience Trends.

The Editing Support Organization can provide English proofreading, Japanese-English translation, and Chinese-English translation services to authors who want to publish in BioScience Trends and need assistance before submitting a manuscript. Authors can visit this organization directly at <http://www.iacmhr.com/iac-eso/support.php?lang=en>. IAC-ESO was established to facilitate manuscript preparation by researchers whose native language is not English and to help edit works intended for international academic journals.

4. Manuscript Preparation

Manuscripts should be written in clear, grammatically correct English and submitted as a Microsoft Word file in a single-column format. Manuscripts must be paginated and typed in 12-point Times New Roman font with 24-point line spacing. Please do not embed figures in the text. Abbreviations should be used as little as possible and should be explained at first mention unless the term is a well-known abbreviation (e.g. DNA). Single words should not be abbreviated.

Title Page: The title page must include 1) the title of the paper (Please note the title should be short, informative, and contain the major key words); 2) full name(s) and affiliation(s) of the author(s), 3) abbreviated names of the author(s), 4) full name, mailing address, telephone/fax numbers, and e-mail address of the corresponding author; and 5) conflicts of interest (if you have an actual or potential conflict of interest to disclose, it must be included as a footnote on the title page of the manuscript; if no conflict of

interest exists for each author, please state "There is no conflict of interest to disclose". Please visit [Download Centre](#) and refer to the title page of the manuscript sample.

Abstract: The abstract should briefly state the purpose of the study, methods, main findings, and conclusions. For article types including Original Article, Brief Report, Review, Policy Forum, and Case Report, a one-paragraph abstract consisting of no more than 250 words must be included in the manuscript. For News and Letters, a brief summary of main content in 150 words or fewer should be included in the manuscript. Abbreviations must be kept to a minimum and non-standard abbreviations explained in brackets at first mention. References should be avoided in the abstract. Key words or phrases that do not occur in the title should be included in the Abstract page.

Introduction: The introduction should be a concise statement of the basis for the study and its scientific context.

Materials and Methods: The description should be brief but with sufficient detail to enable others to reproduce the experiments. Procedures that have been published previously should not be described in detail but appropriate references should simply be cited. Only new and significant modifications of previously published procedures require complete description. Names of products and manufacturers with their locations (city and state/country) should be given and sources of animals and cell lines should always be indicated. All clinical investigations must have been conducted in accordance with Declaration of Helsinki principles. All human and animal studies must have been approved by the appropriate institutional review board(s) and a specific declaration of approval must be made within this section.

Results: The description of the experimental results should be succinct but in sufficient detail to allow the experiments to be analyzed and interpreted by an independent reader. If necessary, subheadings may be used for an orderly presentation. All figures and tables must be referred to in the text.

Discussion: The data should be interpreted concisely without repeating material already presented in the Results section. Speculation is permissible, but it must be well-founded, and discussion of the wider implications of the findings is encouraged. Conclusions derived from the study should be included in this section.

Acknowledgments: All funding sources should be credited in the Acknowledgments section. In addition, people who contributed to the work but who do not meet the criteria for authors should be listed along with their contributions.

References: References should be numbered in the order in which they appear in the text. Citing of unpublished results, personal communications, conference abstracts, and theses in the reference list is not recommended but these sources may be mentioned in the text. In the reference list,

cite the names of all authors when there are fifteen or fewer authors; if there are sixteen or more authors, list the first three followed by *et al.* Names of journals should be abbreviated in the style used in PubMed. Authors are responsible for the accuracy of the references. Examples are given below:

Example 1 (Sample journal reference):

Inagaki Y, Tang W, Zhang L, Du GH, Xu WF, Kokudo N. Novel aminopeptidase N (APN/CD13) inhibitor 24F can suppress invasion of hepatocellular carcinoma cells as well as angiogenesis. *Biosci Trends*. 2010; 4:56-60.

Example 2 (Sample journal reference with more than 15 authors):

Darby S, Hill D, Auvinen A, *et al.* Radon in homes and risk of lung cancer: Collaborative analysis of individual data from 13 European case-control studies. *BMJ*. 2005; 330:223.

Example 3 (Sample book reference):

Shalev AY. Post-traumatic stress disorder: diagnosis, history and life course. In: Post-traumatic Stress Disorder, Diagnosis, Management and Treatment (Nutt DJ, Davidson JR, Zohar J, eds.). Martin Dunitz, London, UK, 2000; pp. 1-15.

Example 4 (Sample web page reference):

Ministry of Health, Labour and Welfare of Japan. Dietary reference intakes for Japanese. <http://www.mhlw.go.jp/houdou/2004/11/h1122-2a.html> (accessed June 14, 2010).

Tables: All tables should be prepared in Microsoft Word or Excel and should be arranged at the end of the manuscript after the References section. Please note that tables should not be in image format. All tables should have a concise title and should be numbered consecutively with Arabic numerals. If necessary, additional information should be given below the table.

Figure Legend: The figure legend should be typed on a separate page of the main manuscript and should include a short title and explanation. The legend should be concise but comprehensive and should be understood without referring to the text. Symbols used in figures must be explained.

Figure Preparation: All figures should be clear and cited in numerical order in the text. Figures must fit a one- or two-column format on the journal page: 8.3 cm (3.3 in.) wide for a single column, 17.3 cm (6.8 in.) wide for a double column; maximum height: 24.0 cm (9.5 in.). Please make sure that the symbols and numbers appeared in the figures should be clear. Please make sure that artwork files are in an acceptable format (TIFF or JPEG) at minimum resolution (600 dpi for illustrations, graphs, and annotated artwork, and 300 dpi for micrographs and photographs). Please provide all figures as separate files. Please note that low-resolution images are one of the leading causes of article resubmission and schedule delays. All color figures will be reproduced in full color in the online edition of the journal at no cost to authors.

Units and Symbols: Units and symbols

conforming to the International System of Units (SI) should be used for physicochemical quantities. Solidus notation (*e.g.* mg/kg, mg/mL, mol/mm²/min) should be used. Please refer to the SI Guide www.bipm.org/en/si/ for standard units.

Supplemental data: Supplemental data might be useful for supporting and enhancing your scientific research and BioScience Trends accepts the submission of these materials which will be only published online alongside the electronic version of your article. Supplemental files (figures, tables, and other text materials) should be prepared according to the above guidelines, numbered in Arabic numerals (*e.g.*, Figure S1, Figure S2, and Table S1, Table S2) and referred to in the text. All figures and tables should have titles and legends. All figure legends, tables and supplemental text materials should be placed at the end of the paper. Please note all of these supplemental data should be provided at the time of initial submission and note that the editors reserve the right to limit the size and length of Supplemental Data.

5. Submission Checklist

The Submission Checklist will be useful during the final checking of a manuscript prior to sending it to BioScience Trends for review. Please visit [Download Centre](#) and download the Submission Checklist file.

6. Online Submission

Manuscripts should be submitted to BioScience Trends online at <http://www.biostencetrends.com>. The manuscript file should be smaller than 5 MB in size. If for any reason you are unable to submit a file online, please contact the Editorial Office by e-mail at office@biostencetrends.com.

7. Accepted Manuscripts

Proofs: Galley proofs in PDF format will be sent to the corresponding author via e-mail. Corrections must be returned to the editor (proof-editing@biostencetrends.com) within 3 working days.

Offprints: Authors will be provided with electronic offprints of their article. Paper offprints can be ordered at prices quoted on the order form that accompanies the proofs.

Page Charge: Page charges will be levied on all manuscripts accepted for publication in BioScience Trends (\$140 per page for black white pages; \$340 per page for color pages). Under exceptional circumstances, the author(s) may apply to the editorial office for a waiver of the publication charges at the time of submission.

(Revised February 2013)

Editorial and Head Office:

Pearl City Koishikawa 603
2-4-5 Kasuga, Bunkyo-ku
Tokyo 112-0003 Japan
Tel: +81-3-5840-8764
Fax: +81-3-5840-8765
E-mail: office@biostencetrends.com

JOURNAL PUBLISHING AGREEMENT (JPA)

Manuscript No.:

Title:

Corresponding Author:

The International Advancement Center for Medicine & Health Research Co., Ltd. (IACMHR Co., Ltd.) is pleased to accept the above article for publication in BioScience Trends. The International Research and Cooperation Association for Bio & Socio-Sciences Advancement (IRCA-BSSA) reserves all rights to the published article. Your written acceptance of this JOURNAL PUBLISHING AGREEMENT is required before the article can be published. Please read this form carefully and sign it if you agree to its terms. The signed JOURNAL PUBLISHING AGREEMENT should be sent to the BioScience Trends office (Pearl City Koishikawa 603, 2-4-5 Kasuga, Bunkyo-ku, Tokyo 112-0003, Japan; E-mail: office@biosciencetrends.com; Tel: +81-3-5840-8764; Fax: +81-3-5840-8765).

1. Authorship Criteria

As the corresponding author, I certify on behalf of all of the authors that:

- 1) The article is an original work and does not involve fraud, fabrication, or plagiarism.
- 2) The article has not been published previously and is not currently under consideration for publication elsewhere. If accepted by BioScience Trends, the article will not be submitted for publication to any other journal.
- 3) The article contains no libelous or other unlawful statements and does not contain any materials that infringes upon individual privacy or proprietary rights or any statutory copyright.
- 4) I have obtained written permission from copyright owners for any excerpts from copyrighted works that are included and have credited the sources in my article.
- 5) All authors have made significant contributions to the study including the conception and design of this work, the analysis of the data, and the writing of the manuscript.
- 6) All authors have reviewed this manuscript and take responsibility for its content and approve its publication.
- 7) I have informed all of the authors of the terms of this publishing agreement and I am signing on their behalf as their agent.

2. Copyright Transfer Agreement

I hereby assign and transfer to IACMHR Co., Ltd. all exclusive rights of copyright ownership to the above work in the journal BioScience Trends, including but not limited to the right 1) to publish, republish, derivate, distribute, transmit, sell, and otherwise use the work and other related material worldwide, in whole or in part, in all languages, in electronic, printed, or any other forms of media now known or hereafter developed and the right 2) to authorize or license third parties to do any of the above.

I understand that these exclusive rights will become the property of IACMHR Co., Ltd., from the date the article is accepted for publication in the journal BioScience Trends. I also understand that IACMHR Co., Ltd. as a copyright owner has sole authority to license and permit reproductions of the article.

I understand that except for copyright, other proprietary rights related to the Work (e.g. patent or other rights to any process or procedure) shall be retained by the authors. To reproduce any text, figures, tables, or illustrations from this Work in future works of their own, the authors must obtain written permission from IACMHR Co., Ltd.; such permission cannot be unreasonably withheld by IACMHR Co., Ltd.

3. Conflict of Interest Disclosure

I confirm that all funding sources supporting the work and all institutions or people who contributed to the work but who do not meet the criteria for authors are acknowledged. I also confirm that all commercial affiliations, stock ownership, equity interests, or patent-licensing arrangements that could be considered to pose a financial conflict of interest in connection with the article have been disclosed.

Corresponding Author's Name (Signature):

Date:

